Investigation of Reverse Pumping in Rotary Seals

by

Karen Ann Davis

B.S. Mechanical Engineering
Florida State University, 2001

SUBMITTED TO THE DEPARTMENT OF MECHANICAL ENGINEERING IN PARTIAL FULFILLMENT OF THE REQUIREMENTS FOR THE DEGREE OF

MASTER OF SCIENCE
AT THE
MASSACHUSETTS INSTITUTE OF TECHNOLOGY

SEPTEMBER 2003

© 2003 Massachusetts Institute of Technology
All rights reserved

Signature of Author _____
Department of Mechanical Engineering
August 25, 2003

Certified by _____
Douglas P. Hart
Associate Professor of Mechanical Engineering
Thesis Supervisor

Accepted by _____
Ain A. Sonin
Chairmen, Department Committee on Graduate Students

BARKER

Investigation of Reverse Pumping in Rotary Seals

by

Karen Ann Davis

Submitted to the Department of Mechanical Engineering
On August 25, 2003 in Partial Fulfillment of the Requirements for the Degree of
Master of Science in
Mechanical Engineering

ABSTRACT

Seals play an integral role in all aspects of mechanisms that are a necessity to daily life. For dynamic seals, the existence of a thin lubricating film makes or breaks a seal. This oil film layer is critical to reduced friction and wear, dissipation of heat generated at the interface, and transport of particles. Coincidentally, the oil film that is a necessity can also be the source of catastrophic failure. Therefore, there also exists an opposing mechanism to prevent leakage referred to as reverse pumping. Although seals have been studied for many years, there are still unknowns concerning this phenomenon of reverse pumping.

The investigations consider the role that grooves play in reverse pumping. A technique previously developed by Douglas P. Hart and Carlos Hidrovo, called Emission Reabsorption Laser Induced Fluorescence (ERLIF), is applied to collect the presented data.

Observations of film thickness measurements at various speeds allude to understanding reverse pumping.

Thesis Supervisor: Douglas P. Hart

Title: Associate Professor of Mechanical Engineering

Biographical Note

Karen Ann Davis was born in Seoul, South Korea on October 1, 1979, moved to the states at the age of two and was adopted by an American family at the age of seven in Pittsfield, MA. She then moved to Clearwater, FL. After high school, she attended St. Petersburg Junior College for a year, received her B.S. in Mechanical Engineering from Florida State University in April of 2001, and then commenced her graduate work at the Massachusetts Institute of Technology in September of 2001. As a S. M. student, Karen was a member of the Hatsopoulos Microfluids Laboratory (HML) where she studied lubrication of seals.

Acknowledgements

Where to begin, first and foremost, I want to thank Douglas for his leap of faith and encouragement in accepting me as one of his students. I would also like to thank Caterpillar for fostering such exciting research and their enthusiasm. I thank Carlos for his belief in me and his patience in not giving up.

Lastly, but certainly not least, I want to thank my family and friends for relentless support and encouragement and especially belief in my abilities, even when I was not such a strong believer. Most of all, to my father who always encouraged me to step up to the next challenge with a vengeance, never back down and constantly strive for success. He took so much pride in any and all accomplishments I made, and I wish so much for him to be here to share in the culmination of everything that this experience has provided me . . .Dad, this one is for you. To my mother who has risen above her own struggles to help me through my darker moments . . .I can never repay you . . .you always knew what to say. I dedicate this to you, because without you, without your love, I would not be here today. To my friends and lab mates and Lily the super-pup who dealt with all my stress and unpleasantness at times, I thank you.

Contents

1.1 Introduction 12
1.2 Sealing Fundamentals 13
1.2.1 Oil Film 14
1.2.2 Load Support 14
1.2.3 Reverse Pumping Background 15
2.1 Theoretical Analysis of Reverse Pumping 21
2.2.1 Analysis-Pressure Difference P (h) 25
2.2.2 Analysis-Viscosity μ (h) 26
2.2.3 Analysis-Effects of Grooves 28
3.1 Experimental Setup-Ratiometric Technique 33
3.2 Experimental Setup-Film Thickness Information 36
3.3 Experimental Setup-Temperature Measurement 38
3.4.1 Experimental Setup-Calibration 42
3.4.2 Experimental Setup-Non-Linearity 47
3.4.3 Experimental Setup-Dyes 50
3.4.4 Experimental Setup-Data Collection 53
4.1 Results and Discussion 55
4.2.1 Results and Discussion-Production Seal-Dye 1 56
4.2.2 Results and Discussion-Plain Seal-Dye 1 63
4.2.3 Results and Discussion-0 Degree Seal-Dye 1 67
4.2.4 Results and Discussion-Production Seal-Dye 4 73
4.2.5 Results and Discussion-15 Degree Seal-Dye 4 83
4.2.6 Results and Discussion-Production Seal with holes-Dye 4 91
5.1 Summary 97
5.2 Conclusions 99
5.3 Future Work 100
Appendix A 101
Appendix B 103
Works Cited 107

List of Figures

1.1 Sealing fundamentals 13

1.2 Schematic of microasperities and the pressure distribution at an asperity 15

1.3 Schematic of test procedure used to observe reverse pumping 16

1.4 Microscopic view of micro-texture 17

1.5 Micro-viscoseal concept 18

1.6 Micro-undulations on a Seal Surface 20

2.1 Velocity distributions for simplified analysis 21

2.2 Schematic of how velocity effects film thickness 24

2.3 Pressure model 25

2.4 Energy balance 26

2.5 Constantinescu model 28

2.6 Seal grooves 29

2.7 Theoretical film thickness vs. shaft speed 31

3.1 Fluorescence vs. film thickness 37

3.2 Transition from separate dye images to the ratio image 41

3.3 Calibration fixture 42

3.4 Calibration fixture 1 and 2 profiles 43

3.5 Transition from calibration image to thickness 44

3.6 Example of fluorescence to thickness image 45

3.7 Layout of regions for data collection 46

3.8 Progression of non-linearity with exponent 47

3.9 Variations with exponent 48

3.10 Theoretical ratio vs. film thickness-original concentration 50

3.11 Theoretical ratio vs. film thickness-varying concentration 51

3.12 Schematic for image collection 53

4.1 Depiction of grooved seal 55

4.2 Calibration–production seal dye 1 56

4.3 Thickness image-production seal dye 1 57

4.4 Thickness images over the speed range-production seal dye 1 58

4.5 Average film thickness vs. shaft speed-production seal dye 1 59

4.6 Images of meniscus movement-production seal dye 1 60

4.7 Meniscus movement-production seal dye 1 61

4.8 Percentage of values based on calibration-production seal dye 1 62

4.9 Calibration–plain seal dye 1 63

4.10 Thickness images over the speed range-plain seal dye 1 64

4.11 Average film thickness vs. shaft speed-plain seal dye 1 65

4.12 Percentage of values based on calibration-plain seal dye 1 66

4.13 Calibration–0 degree seal dye 1 67

4.14 Thickness images over the speed range-0 degree seal dye 1 68

4.15 Average film thickness vs. shaft speed-0 degree seal dye 1 70

4.16 Percentage of values based on calibration-0 degree seal dye 1 71

4.17 Calibration–production seal dye 4 73

4.18 Thickness images over the speed range-production seal dye 4 74

4.19 Images of meniscus movement-production seal dye 4 76

4.20 Meniscus movement-production seal dye 4 77

4.21 Average film thickness vs. shaft speed-production seal dye 4 78

4.22 Percentage of values based on calibration-production seal dye 4 80

4.23 Calibration–15 degree seal dye 4 83

4.24 Thickness images over the speed range-15 degree seal dye 4 84

4.25 Images of meniscus movement-15 degree seal dye 4 86

4.26 Meniscus movement-15 degree seal dye 4 87

4.27 Average film thickness vs. shaft speed-15 degree seal dye 4 89

4.28 Percentage of values based on calibration-15 degree seal dye 4 90

4.29 Schematic of hole placement 91

4.30 Calibration–production seal with holes dye 4 91

4.31 Thickness images over the speed range-prod. seal with holes dye 4 92

4.32 Images of meniscus movement-prod. seal with holes dye 4 94

4.33 Average film thickness vs. shaft speed-prod. seal with holes dye 4 95

4.34 Percentage of values based on calibration-prod. seal with holes dye 4 96

5.1 Average film thickness for tested seals 97

5.2 Meniscus movement for tested seals 98

List of Tables

2.1 Iterated viscosity values 28

3.1 Dye concentrations 52

4.1 Tested seals 55

4.2 Meniscus location-production seal dye 1 60

4.3 Meniscus location-production seal dye 4 77

4.4 Meniscus location-15 degree seal dye 4 87

List of Symbols

h = film thickness

P = pressure

R = shaft radius

T = temperature

t = time

u, v, w = velocity component in the x, y, and z direction respectively

Q = volumetric flow rate

Q' = volumetric flow rate per unit length

$\upsilon = \mu/\rho$ = kinematic viscosity

ρ = density

ω = shaft speed (rad/s)

Film Thickness and Temperature Measurement

C, C_1, C_2 = dye molar concentration (effective 2-dye molar concentration), dye 1 molar concentration, dye 2 molar concentration respectively

I_0 = exciting light intensity at x=0

I_f = total fluorescence intensity

$I_{f,1}'$ = total fluorescence intensity of dye 1 with reabsorption

$I_{f,2}$ = total fluorescence intensity of dye 2 without reabsorption

x = coordinate perpendicular to plane of interest

y = coordinate parallel to plane of interest

t = film thickness

T = temperature

$\varepsilon(\lambda), \varepsilon_1(\lambda), \varepsilon_2(\lambda) =$ molar absorption coefficient at a given wavelength (effective 2 dye molar absorption), dye 1 molar absorption, dye 2 molar absorption respectively

$\eta_1(\lambda), \eta_2(\lambda) =$ dye 1 relative emission at a specific wavelength, dye 2 relative emission at a specific wavelength

$\lambda =$ wavelength

$\xi =$ monitoring efficiency

$\tau =$ time

$\Phi_1, \Phi_2 =$ dye 1 quantum efficiency, dye 2 quantum efficiency

1.1 Introduction

Seals are present in all mechanisms, from the simple to the extremely complex machines, all of which have a crucial role in industry.

The purpose of a seal is to "seal off" one medium from another. This being said, there are two main categories of seals, static and dynamic. Static seals are utilized to prevent leakage in a stationary condition. However, dynamic seals are more complex. In particular, rotary shaft seals require a lubricating oil film layer, counterintuitive to the sealing concept. The complexity is thus in providing a dynamic mechanism for leakage prevention.

Though seals themselves may be inexpensive (less than a dollar in some instances), the failure of just one seal can cost magnitudes more. For example, one unsuccessful seal can lead to a temporary shut-down of a machine; the costs associated with replacing the seal (disassembly of the equipment); and consequently, the operators of these machines are also out of commission. Another consequence is the delay in meeting a deadline, and hence other project deadlines that are compromised in turn. In all, a seal that may have only cost a few dollars may end up costing two or three orders of magnitude more. Thus, the motivation for complete comprehension of sealing fundamentals.

1.2 Sealing Fundamentals

Research related to seal technology has been a topic of interest for about fifty years. It is well known that there are three main components for a seal to function properly: 1) a lubricating layer, 2) load support, 3) and reverse pumping (figure 1.1). Caterpillar provided the funding to investigate variations on seal design for a better understanding of failure prevention.

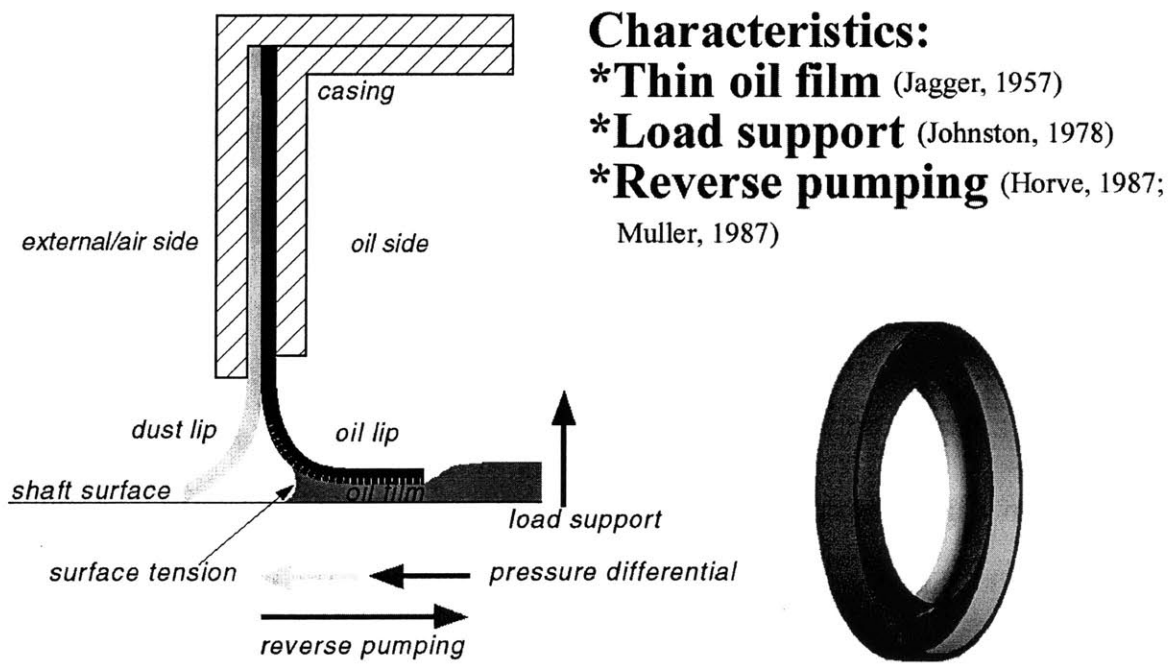

Figure 1.1: Sealing fundamentals. The figure depicts the three basic principles required for a successful seal.

1.2.1 Oil Film

The first fundamental is the existence of a lubrication layer between the shaft-seal interface found to be on the order of 1 micron [10]. This lubricating film is essential for the success of a seal. Ideally, the thicker the oil film is between the shaft and seal, the friction approaches a minimum, simultaneously, increasing the amount of heat that is dissipated from the surface due to any heat generation. The lubricating film in the sliding contact also creates a physical barrier against transfer of contaminants. The dynamic optimization of a lip seal is linked with the ability of the designer to predict and control the thickness and the dynamic characteristics of the fluid film that develops between the seal and shaft [3].

1.2.2 Load Support

As early as 1965, it was hypothesized that microasperities on the shaft surface played a key role in providing load support [10]. In 1966, Jagger also investigated the contribution that microasperities on the surface of the seal contact region provided the oil. Hydrodynamic lubrication allows for the proper load carrying capacity for the existence of the lubricating film.

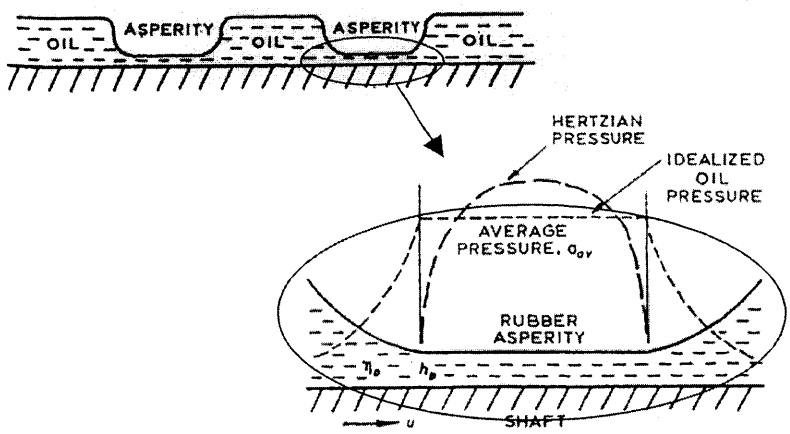

Figure 1.2: Schematic of microasperities and the pressure distribution at an asperity. Notice the maximum pressure occurs at the asperity peak, and as a reaction, the fluid film then lifts the seal off of the surface.

Figure 1.2 shows the pressure that is induced by the presence of an asperity. The oil at the peak of each asperity feels a maximum pressure. The oil has an equal and opposite force which lifts the asperity from the shaft surface, providing the lift necessary for the lubricating film the exist [1]. Actual numerical computation of the pressure fields under the lip was first performed in 1989 by Gabelli [4].

1.2.3 Reverse Pumping Background

Finally, and most importantly, the mechanism that is responsible for the prevention of oil leakage, a phenomenon referred to as reverse pumping. In 1978, Kammüller carried out a test where he injected a known amount of fluid into the airside of a seal and observed the hydrodynamic pumping effect of the oil being transferred from the airside to the oil sump (lower pressure to higher pressure), shown in figure 1.3.

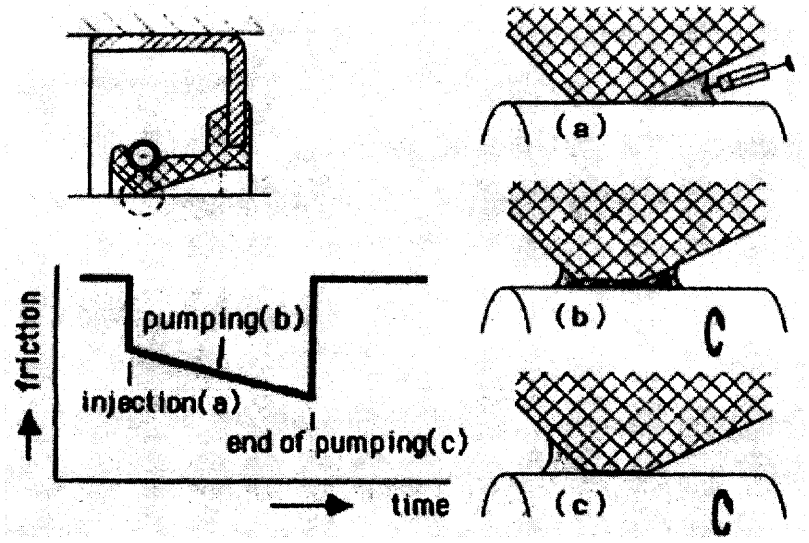

Figure 1.3: Schematic of the test procedure that Kammüller setup to observe the dynamic sealing mechanism.

The importance of completely understanding how to prevent a seal from leaking is essential for the success of a seal. This is thus the main motivation for the research that follows.

As mentioned earlier, reverse pumping is the phenomenon by which a seal runs without leakage. It was observed that a conversely installed seal would leak profusely [12]. Surface topography such as microasperities and microundulations (shown in figure 1.4) coupled with the asymmetric geometry of the seal, are believed to foster this dynamic sealing mechanism.

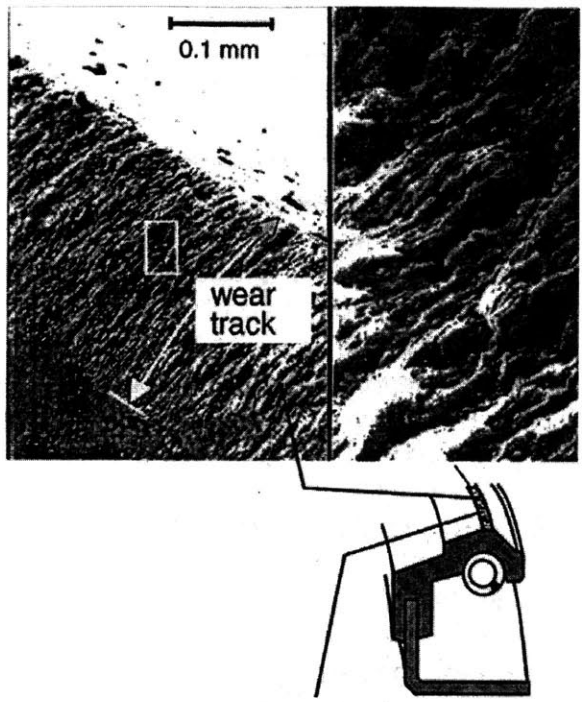

Figure 1.4: An example of a microscopic view of micro-texture on the surface of the contact region of a garter spring seal [13].

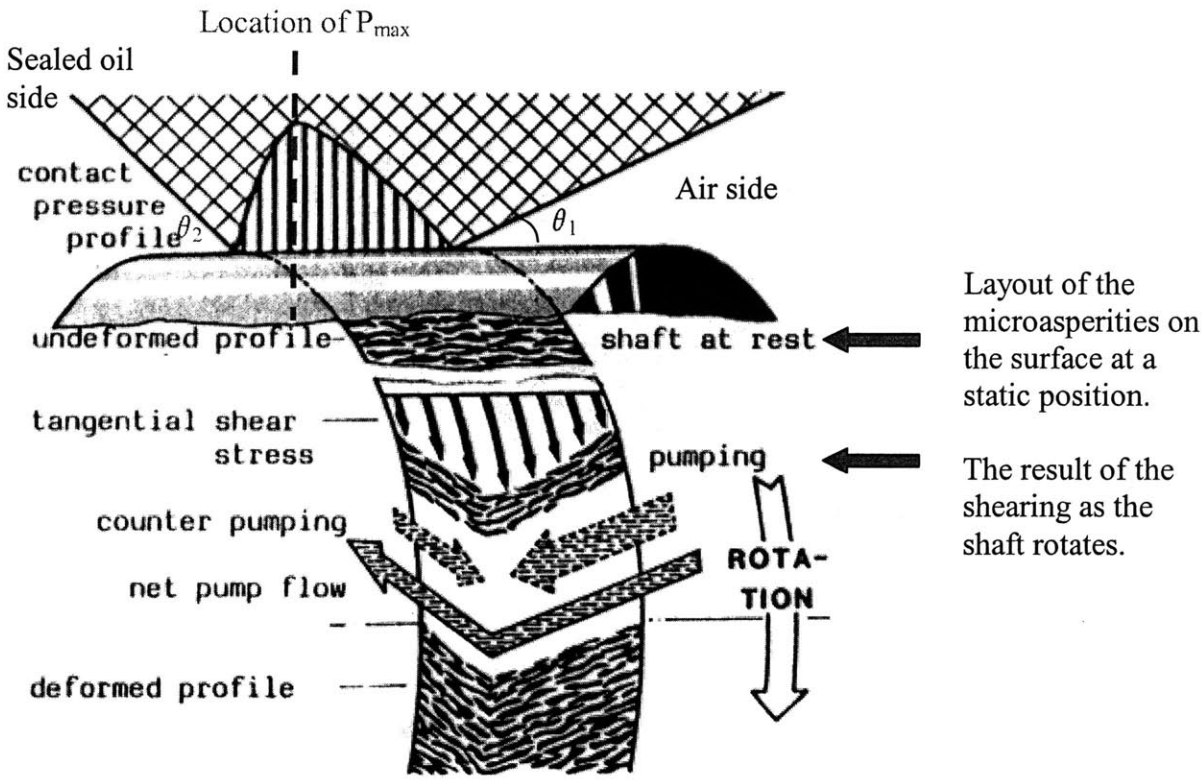

Figure 1.5: Micro-viscoseal concept by Kammüller [11].

Figure 1.5 shows schematically the concept of how the micro-texture induces the reverse pumping action. In the static position, the microasperities (believed to be formed during the initial breaking in of a new seal) appear to form axially along the surface [9]. As a new seal is being broken in (initial wear in process, which is approximately 2-3 hours), different pressures or imperfections on the shaft surface, chip away pieces of the seal, leaving behind topographical texturing and deformation on the seal. Once rotation commences (after the wear in process), the shearing motion in the circumferential direction shears the microasperities in such a way that micro-vanes or channels are formed. The asymmetry of the seal itself ($\theta_1 < \theta_2$), allows for the channels to have a net flow back toward the oil sump. Ideally, there should be oil that seeps out

due to the pressure difference from the oil sump to atmospheric air, and surface tension, but enough opposing reverse pumping would result in a zero net flow case.

The lip surface can be influenced by the shear stress in the lubricating film. In a static case, the axial distribution of contact pressure at the shaft-seal interface is asymmetric (due to $\theta_1 < \theta_2$). The asymmetry causes a higher contact pressure closer to the higher pressure side (oil sump). At this maximum pressure (P_{max} in figure 1.5), film thickness becomes a minimum. The film thickness therefore varies in the axial direction, which allows for variation in the circumferential direction shear stresses. Since shear stress is inversely proportional to film thickness, it is a maximum, at P_{max}. Profiles of the film thickness were confirmed by tests performed by Kawahara and Hirabayashi in 1978; Müller, 1987. These tests also allowed for observation that when P_{max} was located closer to the center, there was more symmetry, and thus less reverse pumping [15].

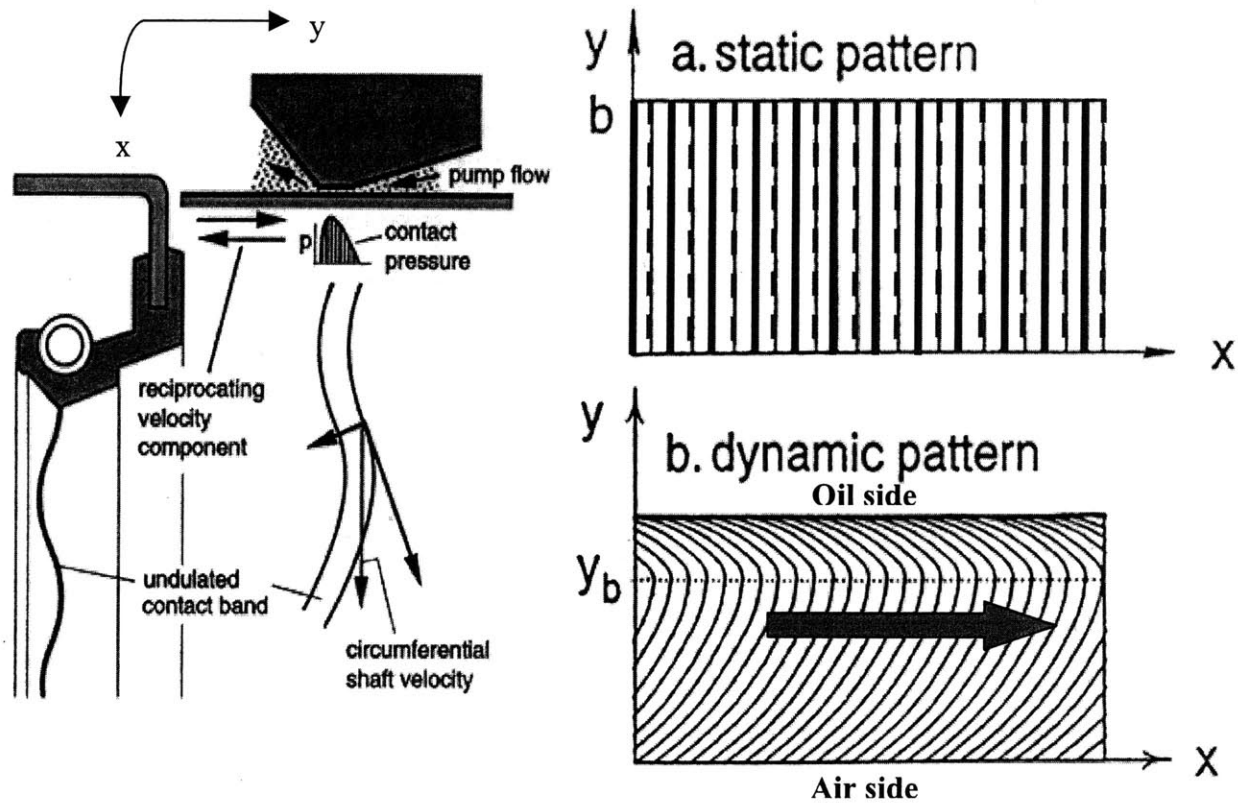

Figure 1.6: Micro-undulations on the surface of a seal and the deformation of them in a dynamic case. The picture on the top right shows the peaks as the solid black lines and the valleys as the purple-segmented lines in the static situation. The red arrow in the dynamic case shows the direction of shearing induced by rotation.

Figure 1.6 represents the scenario of adding a macroscopic texturing to the seal surface in an attempt to induce the reverse pumping with more predictability [13]. The macroscopic variations to a seal allow for a more definite formation or control of vanes for reverse pumping. Grooves on a seal should have a similar effect that the undulations in figure 1.6 have.

Thus the objective of this research is to explore and understand the effects that grooves on the surface of a seal have on the phenomenon of reverse pumping.

2.1 Theoretical Analysis of Reverse Pumping

Before beginning to understand reverse pumping on the more complex seal geometries such as the ones that were tested for this specific research, a more simplified analysis excluding the geometries (i.e., grooves) is necessary.

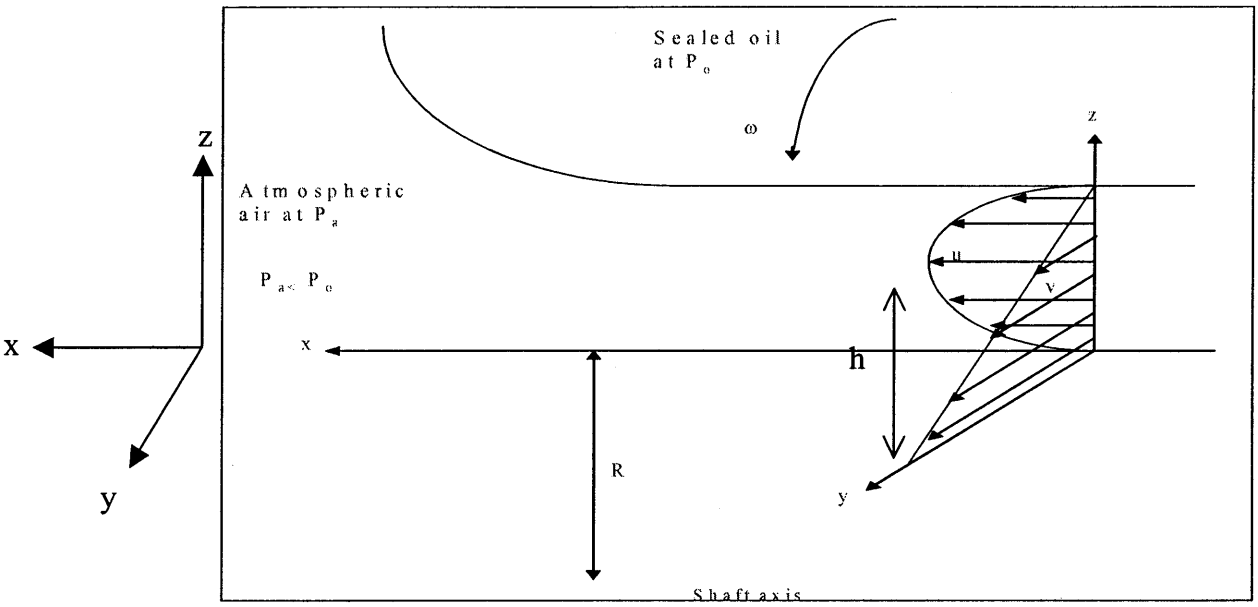

Figure 2.1: Schematic the velocity distributions for simplified analysis to follow. The velocity profile induced by a pressure difference (u) is parabolic in nature while the shear induced flow (v) once rotation commences has a linear profile.

<u>Assumptions that were made [16]</u>:

1) Steady state condition $\Rightarrow \frac{\partial}{\partial t} \approx 0$

2) w $\approx$ 0 (negligible fluid flow in the z direction)

3) u = f(z only); v = f(z only)

4) Fluid is incompressible, $\rho \approx$ constant

5) Film thickness << R (i.e. 1micron << 33400 microns)

6) $\frac{\partial P}{\partial y} \approx 0$ (Though there may be variations circumferentially, there must be continuity since the beginning and end are the same)

$$\frac{\partial u}{\partial t}+u\frac{\partial u}{\partial x}+v\frac{\partial u}{\partial y}+w\frac{\partial u}{\partial z}=-\frac{1}{\rho}\frac{\partial P}{\partial x}+\upsilon(\frac{\partial^2 u}{\partial x^2}+\frac{\partial^2 u}{\partial y^2}+\frac{\partial^2 u}{\partial y^2}) \tag{2.1a}$$

$$\frac{\partial v}{\partial t}+u\frac{\partial v}{\partial x}+v\frac{\partial v}{\partial y}+w\frac{\partial v}{\partial z}=-\frac{1}{\rho}\frac{\partial P}{\partial y}+\upsilon(\frac{\partial^2 v}{\partial x^2}+\frac{\partial^2 v}{\partial y^2}+\frac{\partial^2 v}{\partial y^2}) \tag{2.1b}$$

$$\frac{\partial w}{\partial t}+u\frac{\partial w}{\partial x}+v\frac{\partial w}{\partial y}+w\frac{\partial w}{\partial z}=-\frac{1}{\rho}\frac{\partial P}{\partial z}+\upsilon(\frac{\partial^2 w}{\partial x^2}+\frac{\partial^2 w}{\partial y^2}+\frac{\partial^2 w}{\partial y^2}) \tag{2.1c}$$

First, Navier Stokes' equations (2.1a-c) are simplified based on the assumptions 1-6, which simplify to the equations (2.2a-c).

$$\frac{\partial P}{\partial x}=\mu\frac{\partial^2 u}{\partial z^2} \tag{2.2a}$$

$$\frac{\partial P}{\partial y}=\mu\frac{\partial^2 v}{\partial z^2} \tag{2.2b}$$

$$\frac{\partial P}{\partial z}=0 \tag{2.2c}$$

From Mass Conservation:

$$\frac{\partial u}{\partial x}=-\frac{\partial v}{\partial y}=0 \tag{2.3}$$

Boundary conditions:

$$u(z=0) = u(z=h) = 0 \tag{2.4}$$

$$v(z=0) = R\omega;\ v(z=h) = 0$$

Applying the boundary conditions to solve for u and v:

$$u=\frac{z^2}{2\mu}\frac{\partial P}{\partial x}-z\frac{h}{2\mu}\frac{\partial P}{\partial x}$$

$$v = \frac{1}{2\mu} z^2 \frac{\partial P}{\partial y} - z\left(\frac{R\omega}{h} + \frac{h}{2\mu}\frac{\partial P}{\partial y}\right) + R\omega \tag{2.5}$$

The volumetric flow rate is defined as:

$$\begin{aligned} Q_x &= \int u dA_x \qquad dA_x = 2\pi R dz \\ Q_y &= \int v dA_y \qquad dA_y = dz dx \end{aligned} \tag{2.6}$$

Combining equations (2.5) and (2.6):

Q_x' and Q_y' represent the volumetric flow rate per unit length in the axial and circumferential direction respectively.

$$\begin{aligned} Q_x' &= \frac{Q_x}{2\pi R} = -\frac{h^3}{12\mu}\frac{\partial P}{\partial x} \\ Q_y' &= \frac{Q_y}{x} = \frac{R\omega h}{2} \end{aligned} \tag{2.7}$$

From equation (2.7), it is apparent that there are two main components of the volumetric flow rate:

1. Q_p' ⇒ Poiseuille flow (pressure driven) ⇒ Q_x'
2. Q_c' ⇒ Couette flow (boundary driven) ⇒ Q_y'

Q_x' is directly proportional to film thickness cubed and the pressure differential in the axial direction while inversely proportional to the oil viscosity. Q_y' depends upon the radius, angular velocity, and film thickness. At a glance, Q_y' appears to be the only term that would be directly effected by velocity changes. However, it is also known that friction (heat generation) also increases, temperature within the lubricating film increases, thus decreasing the oil viscosity, and hence the film thickness, h.

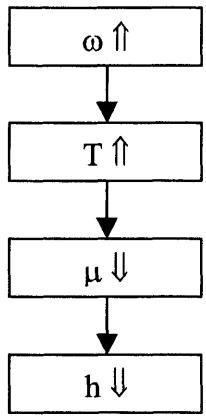

Figure 2.2: Schematic of how a change in velocity affects h.

Therefore, each of the elements, along with their contributions, that make up the axial and circumferential flow rates, need to be assessed. In other words, Q_x' and Q_y' need to be functions of one variable (h in this case) only, to compare the effects of the pressure driven to the boundary driven flow.

2.2.1 Analysis-Pressure Difference P (h)

Since the seal is made out of an elastic material, we assume that the lip tip can be modeled as a spring in order to get a relative idea about the pressure at a specific location, x_0.

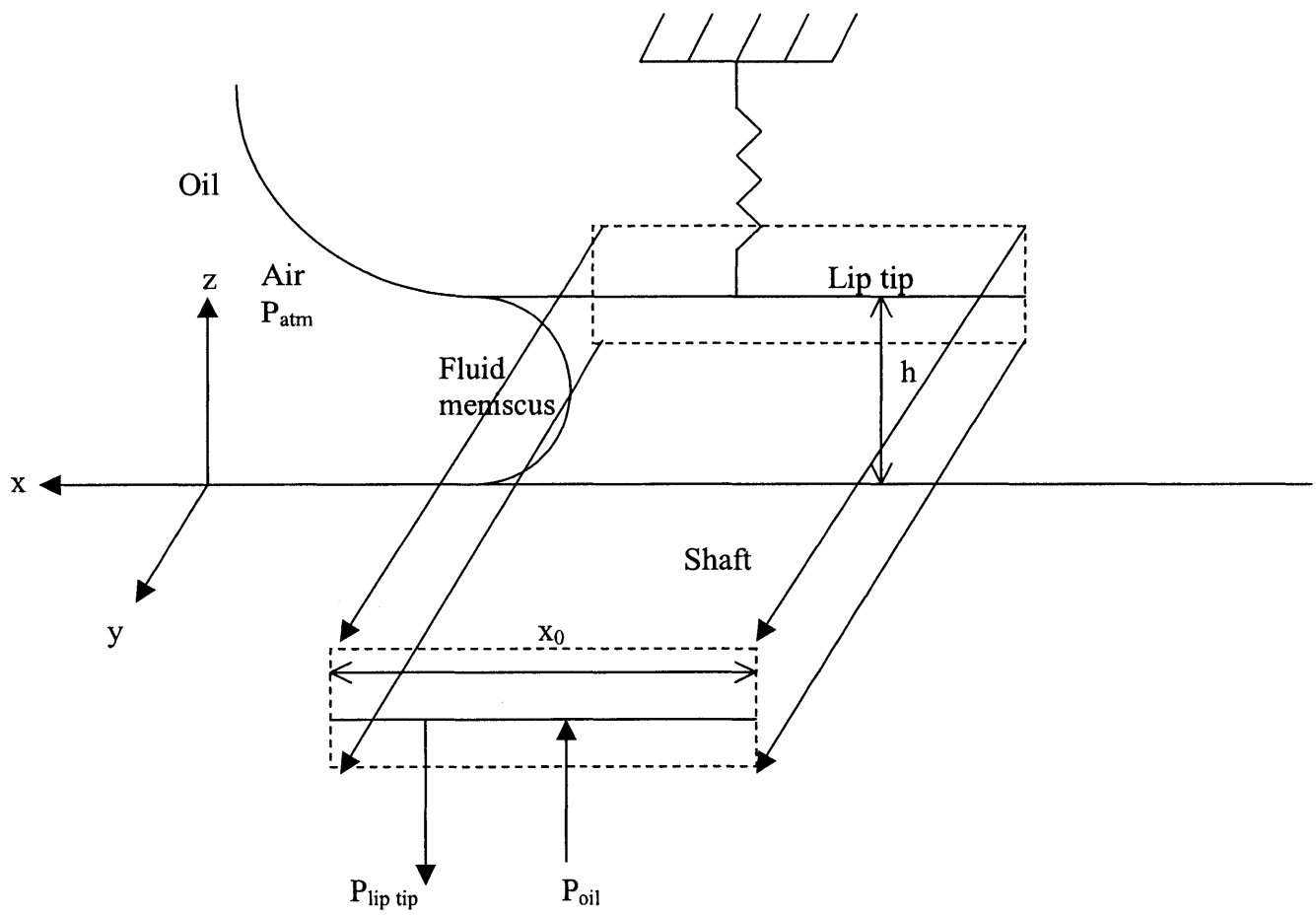

Figure 2.3: Diagram of pressure at the lip tip interface modeling x_0 as a spring.

$$P_{lip\ tip} = P_{oil} = \frac{k_{teflon} z}{A} = \frac{k_{teflon} h}{2\pi R x_0} \quad \text{(more detailed derivation in Appendix A)} \qquad (2.8)$$

Equation (2.8) gives the pressure in terms of known values k_{teflon} (thermal conductivity of Teflon), shaft and seal geometry and h.

2.2.2 Analysis-Viscosity μ(h)

As angular velocity increases, the amount of heat that is generated increases, and hence the temperature within the oil film increases. It would therefore be beneficial to understand the effect that T has on μ. The relationship between the two proves to be inversely proportional, i.e. as the temperature increases within a fluid, the viscosity decreases and visa versa. In 1926, MacCoull proposed the following correlation [16]:

$$\begin{aligned} &\log_{10}[\log_{10}(\nu+0.8)] = \eta \log_{10} T + c \\ &\eta = -3.1562 \\ &c = 8.9679 \end{aligned} \tag{2.9}$$

From (2.9), the unknowns are the viscosity and temperature; the next step is to obtain another relationship between the temperature and viscosity in terms of film thickness (h). This was achieved by looking at an energy balance for a fluid particle in the lubrication layer.

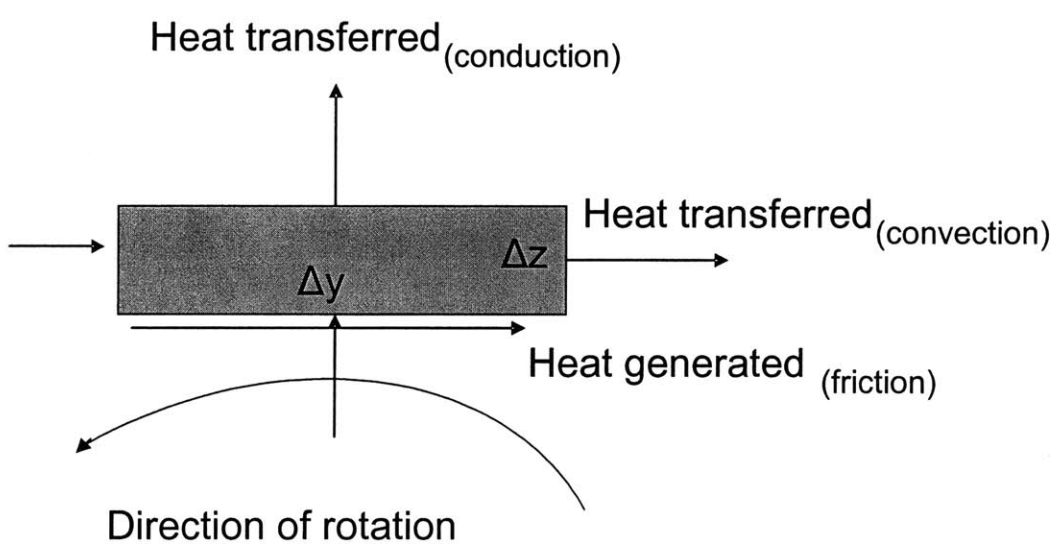

Figure 2.4: Diagram of heat transfer through a fluid particle and the heat generated at the shearing interface once rotation is commenced.

Heat transferred$_{(conduction)}$+ Heat transferred$_{(convection)}$ = Heat generated$_{(friction)}$

<u>Assumptions</u>:

1) Steady state

2) Heat transfer through convection at each z location (circumferentially) can be neglected (the same reason that $\frac{\partial P}{\partial y} \approx 0$)

Heat transferred$_{(conduction)}$ = Heat generated$_{(friction)}$

$$k_{oil}\frac{\partial T}{\partial z}(2\pi R)\Delta x\,/_{z+\Delta z} - k_{oil}\frac{\partial T}{\partial z}(2\pi R)\Delta x\,/_{z} = \mu v\frac{\partial v}{\partial z}(2\pi R)\Delta x \qquad (2.10)$$

$$T = \frac{\mu}{k_{oil}}v^2 + T(\omega = 0) = \frac{\mu}{k_{oil}}(R\omega)^2 + 25^{o}C$$

Combining equations (2.9) and (2.10):

$$v = 10^{10^{[-3.1562\log_{10}\left\{\frac{v\rho_{oil}}{k_{oil}}(R\omega)^2 + T(\omega=0)\right\}+8.9679]}} - 0.8 \qquad (2.11)$$

$$\rho_{oil} = 54.45818\frac{lb}{ft^3}$$

$$k_{oil} = 0.000020704\frac{Btu}{s-ft-^{o}F}$$

$$[\frac{v\rho_{oil}}{k_{oil}}(R\omega)^2 + T(\omega = 0)] = {}^{o}R$$

Equation (2.11) is in terms of known values and unknown values-temperature and kinematic viscosity. With iteration, estimates for the viscosity change with change in speed is calculated and shown in table 2.1.

Table 2.1: Viscosity values at each speed

omega (rpm)	omega (rad/s)	mu (kg/m-s)
0	0	0.15340336
300	31.4159	0.14349249
600	62.8318	0.1226399
900	94.2477	0.10195617
1200	125.6636	0.08497768
1500	157.0795	0.07169078
1800	188.4954	0.06136546
2100	219.9113	0.05317122

2.2.3 Analysis-Effects of Grooves

For generalization purposes, the axial and circumferential components that were derived in the simplified case now have to be broken down into components due to the grooves. Constantinescu carried out a detailed derivation for considering geometric effects in the volumetric flow rate [1 and 2].

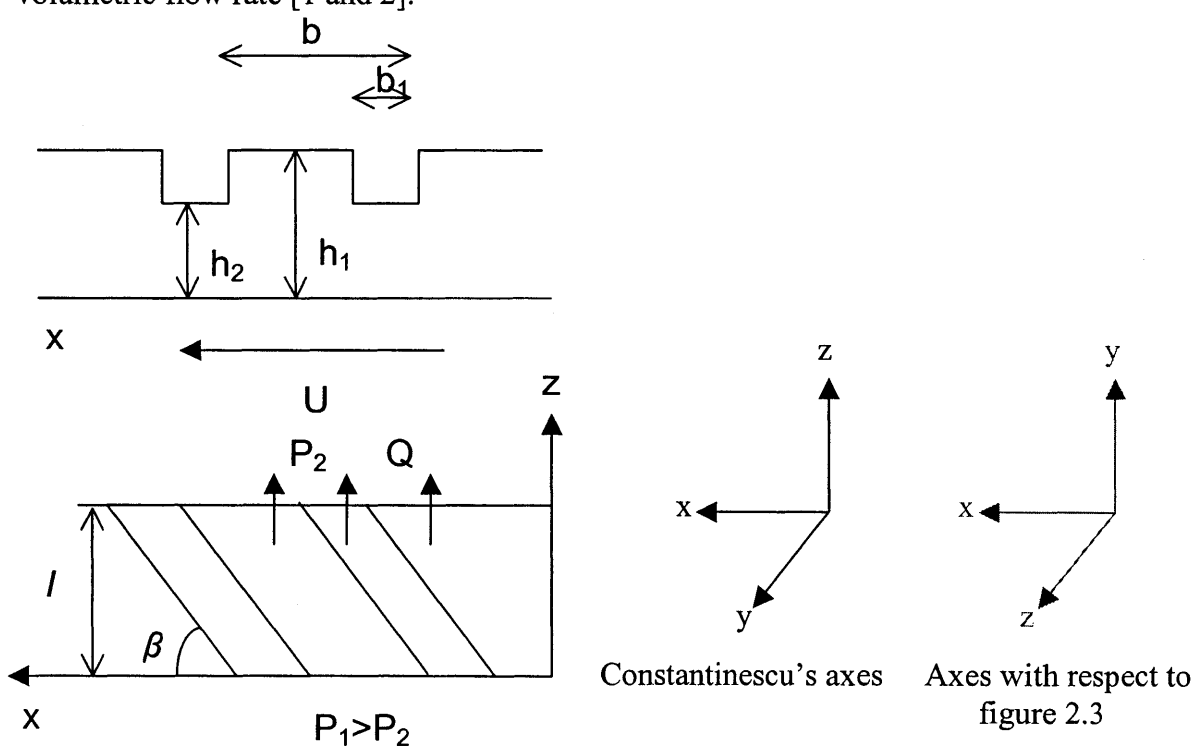

Figure 2.5: Schematic Constantinescu used to model volumetric flow rate of a seal with grooves.

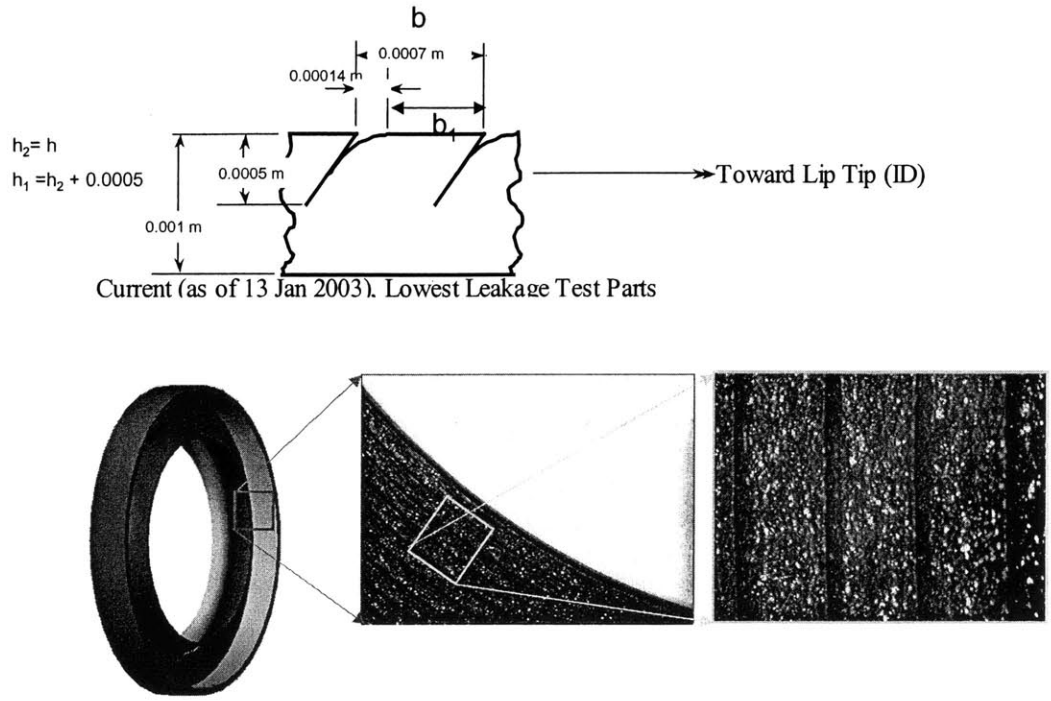

Figure 2.6: Schematic of the actual seal of interest that was tested, depicting the correlating values to those in figure 2.5. Also, a close up image of the seal grooves.

$$\frac{\Delta Q}{\Delta x} = -\frac{1}{12\mu}\left[\begin{array}{c} \dfrac{h^3{}_1 h_2{}^3 + \dfrac{b_1}{b}\left(1-\dfrac{b_1}{b}\right)\sin^2\beta(h^3{}_1 - h_2{}^3)^2}{\left(1-\dfrac{b_1}{b}\right)h^3{}_1 + \dfrac{b_1}{b}h_2{}^3}\dfrac{\partial P}{\partial x} \\ -\dfrac{6\mu U(h_1-h_2)\dfrac{b_1}{b}\left(1-\dfrac{b_1}{b}\right)\sin\beta\cos\beta(h^3{}_1 - h_2{}^3)}{\left(1-\dfrac{b_1}{b}\right)h^3{}_1 + \dfrac{b_1}{b}h_2{}^3} \end{array}\right] \tag{2.12}$$

Though equation (2.12) looks complicated, the coefficients of both terms on the right are essentially due to the geometry of the grooves. Now compare to equation (2.7), equation (2.12) also has a term due to a pressure difference as well as a change in velocity, the two equations are hence very similar.

Combining Constinescu's model with equations (2.7), the following can be investigated:

Net Q' in the axial direction =

(Q' due to Poiseuille flow)$_{\text{axial components}}$ + (Q' due to Couette flow)$_{\text{axial components}}$

$$Q_{net}' = Q_{P,x}' + Q_{C,x}'$$

Or for the case when there is not net flow:

$$Q_{P,x}' = -Q_{C,x}' \tag{2.13}$$

Equation (2.13) combined with (2.7), (2.8), and (2.11), insight is shed on the change in the film thickness, h, with shaft speed (detailed derivation with the appropriate geometries appears in Appendix B).

$$-\frac{h^3}{12\mu}\frac{\frac{k_{teflon}h}{2\pi R x_0} - P_{atm}}{x_0} + \frac{R\omega h}{2} = 0$$

$$\text{R} = 0.0334\text{m} \tag{2.14}$$

$$x_0 = 0.00675m$$

$$P_{atm} = 1.01 * 10^5 \frac{N}{m^2}$$

$$k_{teflon} = 3083332.355\frac{N}{m}$$

μ = values from table 2.1

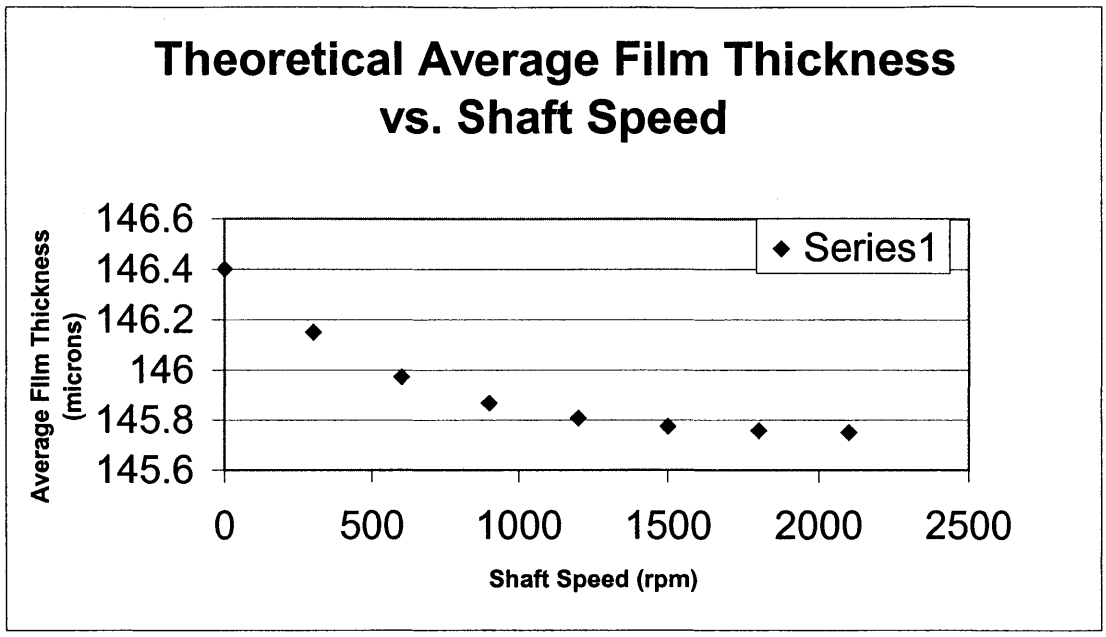

Figure 2.7: Trend of how the film thickness changes with respect to the shaft speed. Notice how the trend decreases with increasing shaft speed.

Film thickness decreases with shaft speed with a second order polynomial trend. This will provide us with an idea of what to expect from the experimental data in order to have the hydrodynamic lubrication balance with the reverse pumping rate.

3.1 Experimental Setup-Ratiometric Technique

The means by which film thickness measurements were observed was via a method based upon Laser Induced Fluorescence (LIF). Fluorescent particles within the fluid of interest, in this case oil, fluoresce at various intensity levels depending on the chosen dyes and the time and type of exposure to a light source. This method is utilized in various tracking applications for fluid mechanics research.

Emission Reabsorption Laser Induced Fluorescence (ERLIF) system was developed by Carlos Hidrovo and Douglas Hart [5 and 6]. Though both dyes absorb the light from the laser excitation, one of the dyes also absorbs the emission of light from the other dye. Therefore, one dye absorbs much more than the other, and the other dye emits less since it is getting reabsorbed by the first dye. Taking the ratio of the fluorescent and illuminating intensities, eliminates the dependence on the excitation intensity, leaving only the information of interest, film thickness and temperature (i.e. R (t, T)). Since this research was not about the development of the ERLIF system, only a brief overview will be included.

Illumination intensity as a function of position and time:

$$I_o = I_o(y, \tau) \tag{3.1}$$

Therefore the total fluorescence intensity:

$$I_f = I_f(t, y, \tau)$$

or

$$I_f = I_f(t, T, y, \tau) \tag{3.2}$$

The ratio of the two intensities:

$$R = \frac{I_f}{I_o} \tag{3.3}$$

The methodology behind the two dye system allows for the separation so R(T) or R(t). For film thickness analysis, the following relationship exists.

$$R(t) = \frac{I_{f,1}'}{I_{f,2}} \tag{3.4}$$

$I_{f,1}'$ = total fluorescence intensity of dye 1 with reabsorption

$I_{f,2}$ = total fluorescence intensity of dye 2

The temperature relationship:

$$R(T) = \frac{I_{f,1}}{I_{f,2}} \tag{3.5}$$

$I_{f,1}$ = total fluorescence intensity of dye one (no reabsorption)

The issue here is since in order to obtain the film thickness measurement, a system where there is a reabsorbed dye is necessary while the temperature information requires no reabsorption.

3.2 Experimental Setup-Film Thickness Information

Film thickness information lies within the reabsorbed dye. Therefore, the system must be optically thick so the information is not lost when the ratio is taken.

$$I_{f1}'(t,\lambda_{filter1},y,\tau) = \frac{\xi I_o(y,\tau)\epsilon_1(\lambda_{laser})C_1\Phi_1\eta_1(\lambda_{filter1})\left(1-\exp\left\{-\left[\epsilon(\lambda_{laser})C+\epsilon_2(\lambda_{filter1})C_2\right]t\right\}\right)}{\epsilon(\lambda_{laser})C+\epsilon_2(\lambda_{filter1})C_2} \tag{3.6}$$

$$I_{f2}(t,\lambda_{filter2},y,\tau) = \frac{\xi I_o(y,\tau)\epsilon_2(\lambda_{laser})C_2\Phi_2\eta_2(\lambda_{filter2})\left(1-\exp\left\{-\left[\epsilon(\lambda_{laser})C\right]t\right\}\right)}{\epsilon(\lambda_{laser})C} \tag{3.7}$$

Then:

$$R(t)=\frac{I_{f,1}'}{I_{f,2}}=\frac{\varepsilon_1(\lambda_{laser})C_1\Phi_1\eta_1(\lambda_{filter1})\varepsilon(\lambda_{laser})C(1-\exp\{-[\varepsilon(\lambda_{laser})C+\varepsilon_2(\lambda_{laser})C_2]t\})}{\varepsilon_2(\lambda_{laser})C_2\Phi_2\eta_2(\lambda_{filter2})(\varepsilon(\lambda_{laser})C+\varepsilon_2(\lambda_{filter1})C_2)(1-\exp\{-[\varepsilon(\lambda_{laser})C]t\})} \tag{3.8}$$

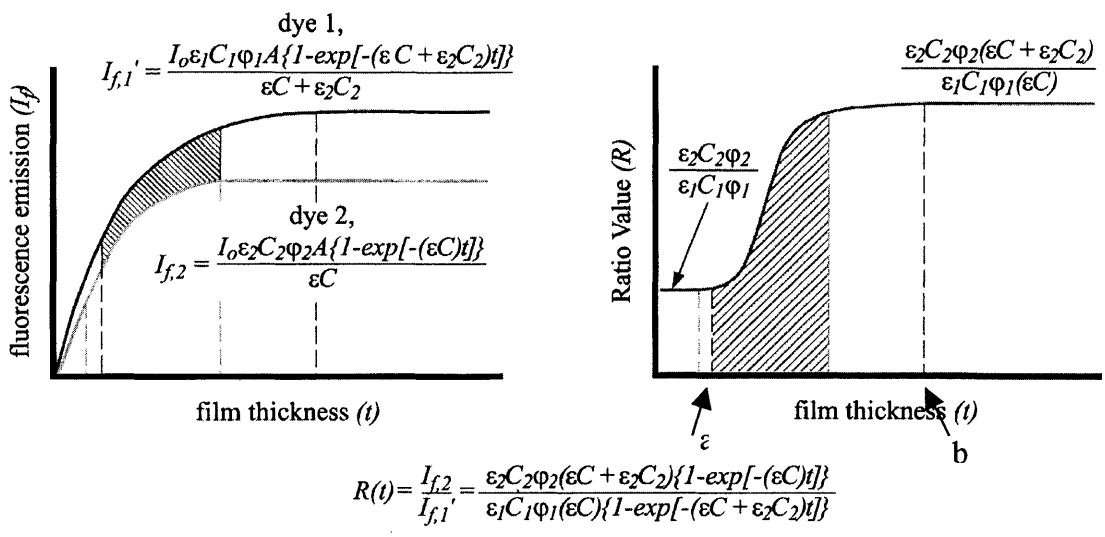

$$R(t)=\frac{I_{f,2}}{I_{f,1}'}=\frac{\varepsilon_2C_2\varphi_2(\varepsilon C+\varepsilon_2C_2)\{1-exp[-(\varepsilon C)t]\}}{\varepsilon_1C_1\varphi_1(\varepsilon C)\{1-exp[-(\varepsilon C+\varepsilon_2C_2)t]\}}$$

Figure 3.1: Fluorescence as a function of film thickness for both dyes, and their ratio.

Figure 3.1 depicts the profile of intensities that are emitted by each dye as well as the profile of the ratio between the two. The region of interest lies between a and b.

3.3 Experimental Setup-Temperature Measurement

Opposing the requirements for the film thickness measurements, an optically thin system is required to acquire temperature information. Film thickness with an optically thin system proves to have a linear relationship, therefore would cancel out with the ratio.

$$I_{f,1}'(t,\lambda_{filter1},y,\tau) = \frac{\xi I_o(y,\tau)\epsilon_1(\lambda_{laser})C_1\Phi_1\eta_1(\lambda_{filter1})\left(1-\exp\left\{-\left[\epsilon(\lambda_{laser})C+\epsilon_2(\lambda_{filter1})C_2\right]t\right\}\right)}{\epsilon(\lambda_{laser})C+\epsilon_2(\lambda_{filter1})C_2} \tag{3.9}$$

if the system is optically thin, equation above can be approximated as

$$I_{f,1}'(t,\lambda_{filter1},y,\tau) \approx \frac{\xi I_o(y,\tau)\epsilon_1(\lambda_{laser})C_1\Phi_1\eta_1(\lambda_{filter1})\left[\epsilon(\lambda_{laser})C+\epsilon_2(\lambda_{filter1})C_2\right]t}{\epsilon(\lambda_{laser})C+\epsilon_2(\lambda_{filter1})C_2} \tag{3.10}$$

and simplifying terms

$$I_{f,1}'(t,\lambda_{filter1},y,\tau) \approx \xi I_o(y,\tau)\epsilon_1(\lambda_{laser})C_1\Phi_1\eta_1(\lambda_{filter1})t \tag{3.11}$$

such that

$$R = \frac{I_{f,1}'}{I_{f,2}} \tag{3.12}$$

$$R(\lambda_{filter1}, \lambda_{filter2}) \approx \frac{\epsilon_1(\lambda_{laser})\, C_1\ \Phi_1 \eta_1(\lambda_{filter1})}{\epsilon_2(\lambda_{laser})\, C_2\ \Phi_2 \eta_2(\lambda_{filter2})} \tag{3.13}$$

is not dependent on film thickness.

Also:

$$I_{f,1}(t, T, \lambda_{filter1}, y, \tau) \ = \ \xi\, I_o(y, \tau) C_1 \Phi_1 \eta_1(\lambda_{filter1}) \left\{ \epsilon_{1,o}(\lambda_{laser}) t - k \int_0^t T(x)\, dx \right\} \tag{3.14}$$

$$I_{f,2}(t, \lambda_{filter2}, y, \tau) \ = \ \xi\, I_o(y, \tau) \epsilon_2(\lambda_{laser}) C_2 \Phi_2 \eta_2(\lambda_{filter2}) t \tag{3.15}$$

and taking their ratio

$$R \ = \ \frac{I_{f,1}}{I_{f,2}} \tag{3.16}$$

$$R(T, \lambda_{filter1}, \lambda_{filter2}) = \frac{\epsilon_{1,o}(\lambda_{laser}) C_1 \Phi_1 \eta_1(\lambda_{filter1})}{\epsilon_2(\lambda_{laser}) C_2 \Phi_2 \eta_2(\lambda_{filter2})} - \frac{k C_1 \Phi_1 \eta_1(\lambda_{filter1})}{\epsilon_2(\lambda_{laser}) C_2 \Phi_2 \eta_2(\lambda_{filter2})} \frac{\int_0^t T(x)\, dx}{t} \tag{3.17}$$

where

$$\frac{\int_0^t T(x)\ \ dx}{t} = T_{x-avg} \tag{3.18}$$

and therefore

$$R(T_{x-avg}, \lambda_{filter1}, \lambda_{filter2}) = \frac{\epsilon_{1,o}(\lambda_{laser})C_1\Phi_1\eta_1(\lambda_{filter1})}{\epsilon_2(\lambda_{laser})C_2\Phi_2\eta_2(\lambda_{filter2})} - \frac{kC_1\Phi_1\eta_1(\lambda_{filter1})}{\epsilon_2(\lambda_{laser})C_2\Phi_2\eta_2(\lambda_{filter2})}T_{x-avg} \tag{3.19}$$

which is independent of excitation intensity and film thickness, while providing a measure of the average temperature in the direction of observation. Equation (3.19) can be rewritten in a simpler form by letting

$$\frac{\epsilon_{1,o}(\lambda_{laser})C_1\Phi_1\eta_1(\lambda_{filter1})}{\epsilon_2(\lambda_{laser})C_2\Phi_2\eta_2(\lambda_{filter2})} = const. = a \tag{3.20}$$

and

$$\frac{kC_1\Phi_1\eta_1(\lambda_{filter1})}{\epsilon_2(\lambda_{laser})C_2\Phi_2\eta_2(\lambda_{filter2})} = const. = b \tag{3.21}$$

in which case

$$R(T_{x-avg}, \lambda_{filter1}, \lambda_{filter2}) = a - b\,T_{x-avg} \tag{3.22}$$

Another benefit from taking a ratiometric approach is the elimination of the laser fluctuations or noise.

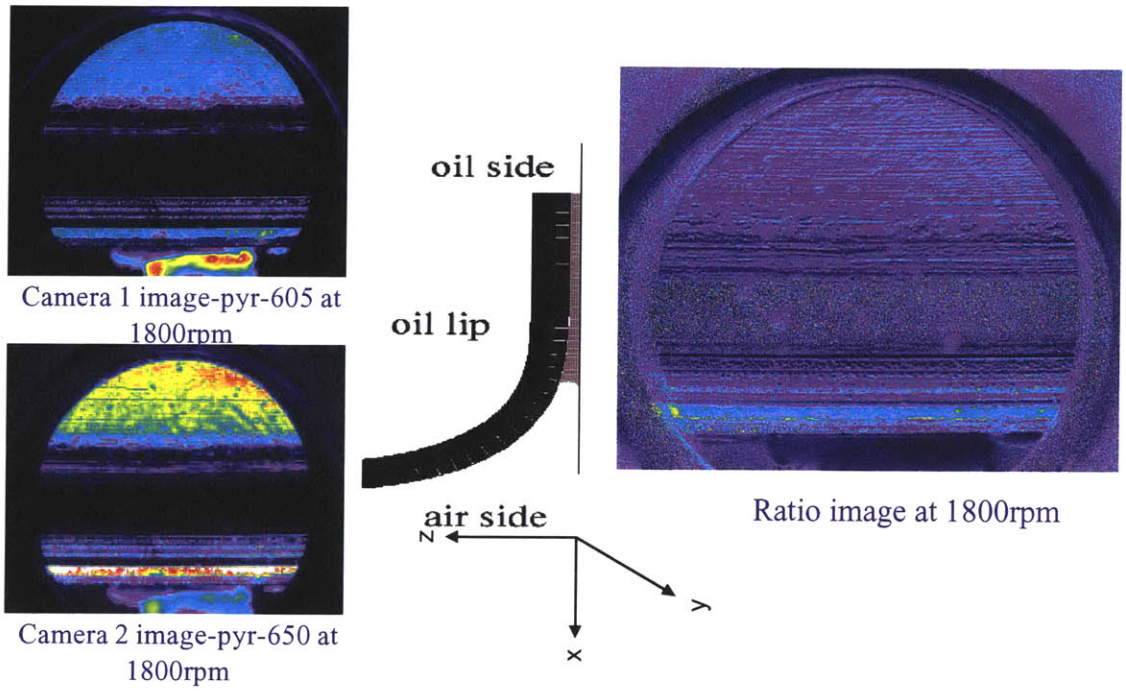

Figure 3.2: Example of each fluorescent image and the resulting ratio image to the right.

3.4.1 Experimental Setup-Calibration

The data that was collected from each test produced intensity images over a 2-D pixel image. A correlation needed to be provided to then translate these intensity values into thickness values. This was achieved by means of two calibration fixtures with measurements provided by Caterpillar. These fixtures consisted of a top and bottom plate made out of quartz that were mated together using four corner bolts shown in figure 3.3.

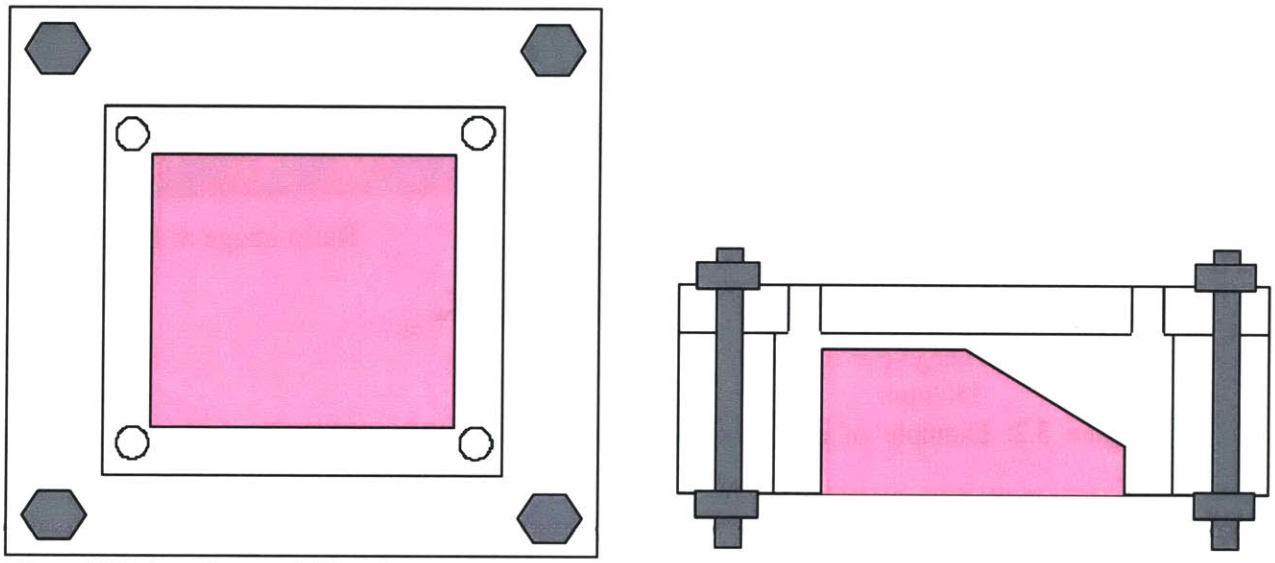

Figure 3.3 Top view and side view of calibration fixture.

Figure 3.4 a) and b) are the profiles of the two different fixtures. Fixture 1 has a steeper slope and a quicker drop off than fixture 2.

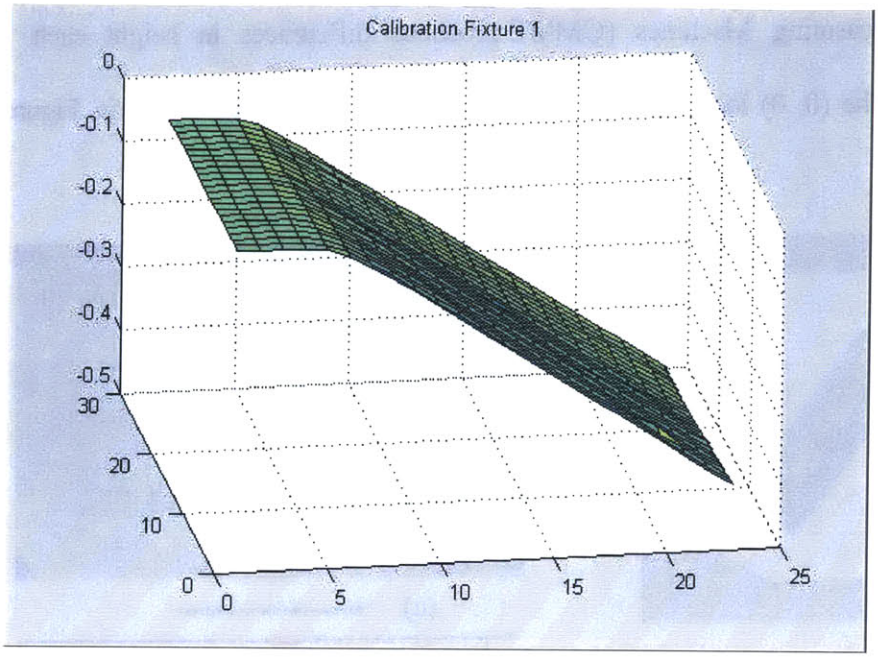

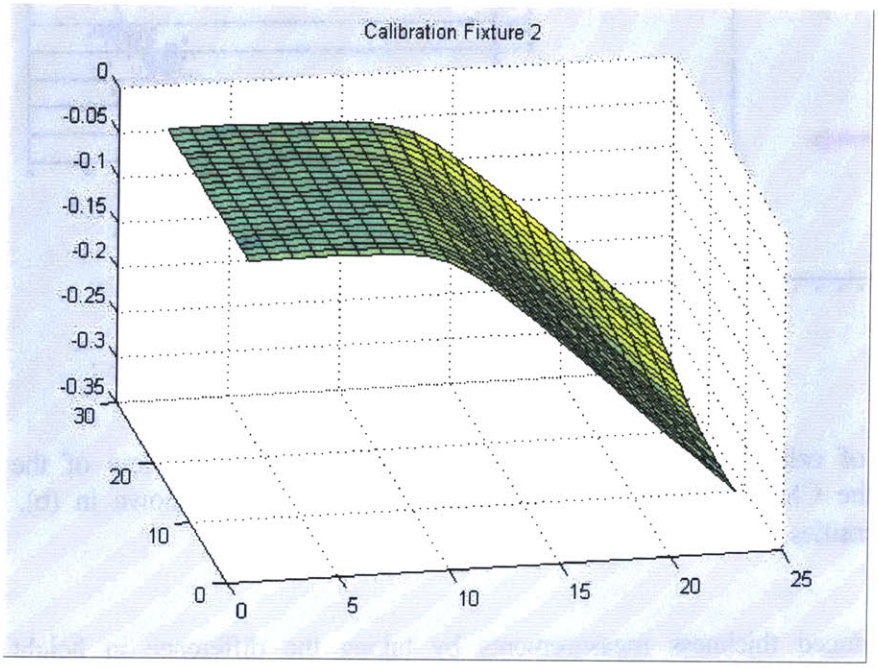

Figure 3.4 Profile of the bottom plate for a) Calibration fixture 1 and b) Calibration fixture 2.

Coordinate Measuring Machines (CMM) produced differences in height each 1 mm apart, starting at the (0, 0) location with a thickness set to 0 microns, shown in Figure 3.5.

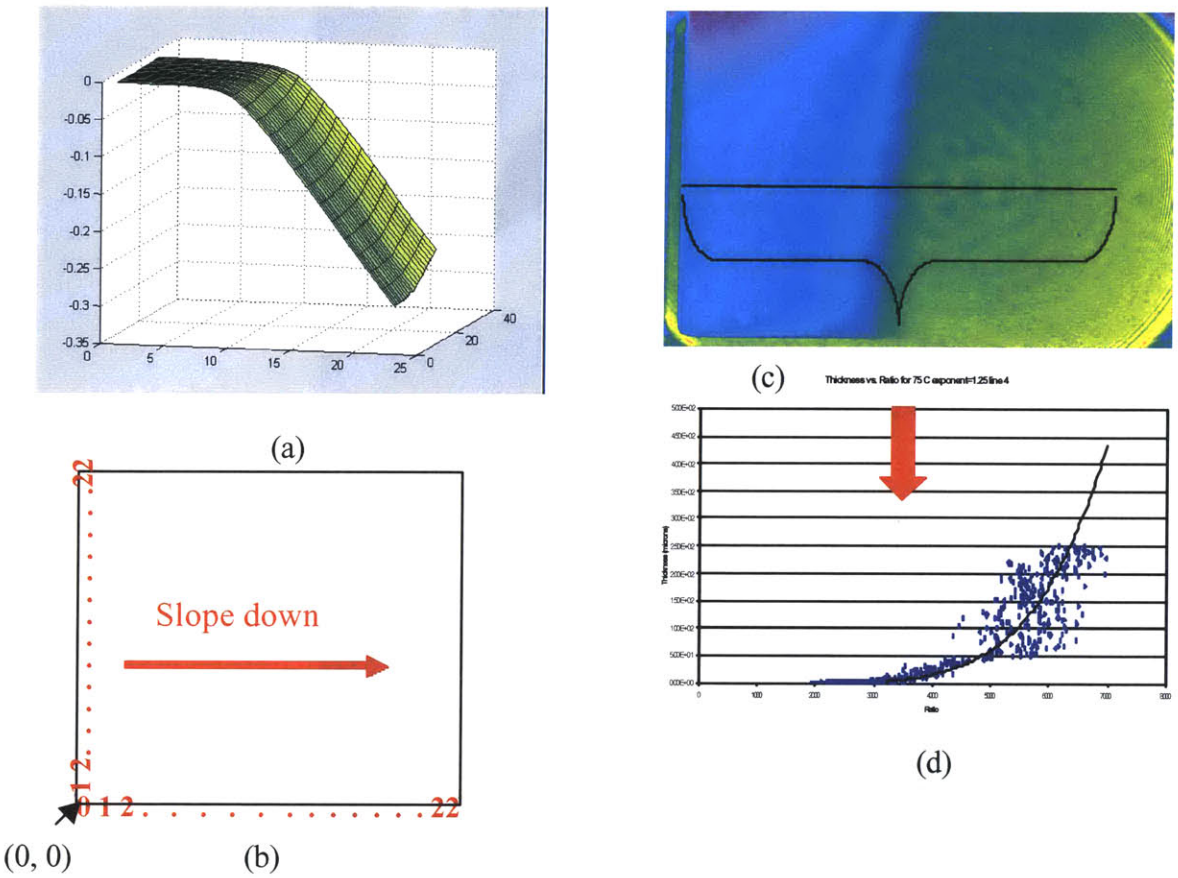

Figure 3.5 (a) Profile of calibration fixture 2 from figure 3.4, (b) the top view of the calibration fixture and the CMM scheme, (c) intensity image of the fixture shown in (b), (d) correlation of the intensities to the CMM values.

The CMM produced thickness measurements by taking the difference in height down the slope from the (0, 0) reference. This introduced some error with respect to the shallow region. Each time the fixture was put together, the surfaces pressing against each other may induce deformation of the surfaces (this was observed by noticing the

interference rings in the regions of closest contact with the top plate). The most accurate results would have been if the plates mated without stress.

Once the correlation between the film thickness and intensity levels were analyzed (figure 3.5d) with a best-fit equation to interpolate. A series of MATLAB programs were then applied to the test seal images with the appropriate non-linearizing exponent (discussed in the following section) and each pixel value was translated into a thickness measurement based on the calibration.

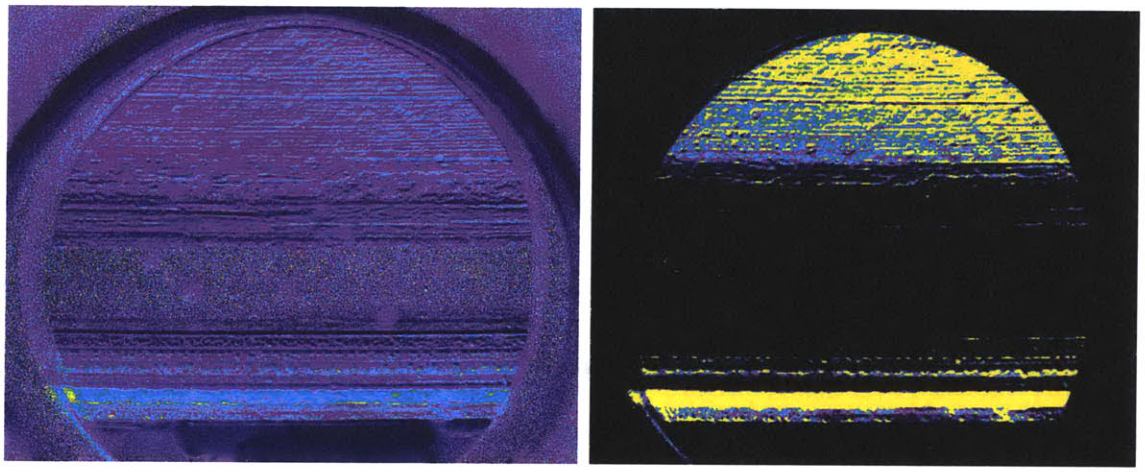

Figure 3.6: Left image is a ratio image of a seal at 1800 rpm, the right image is the same seal with the appropriate calibration applied, translating the ratio image into a film thickness image.

The images were then broken up into four different regions (a-d) shown in figure 3.7.

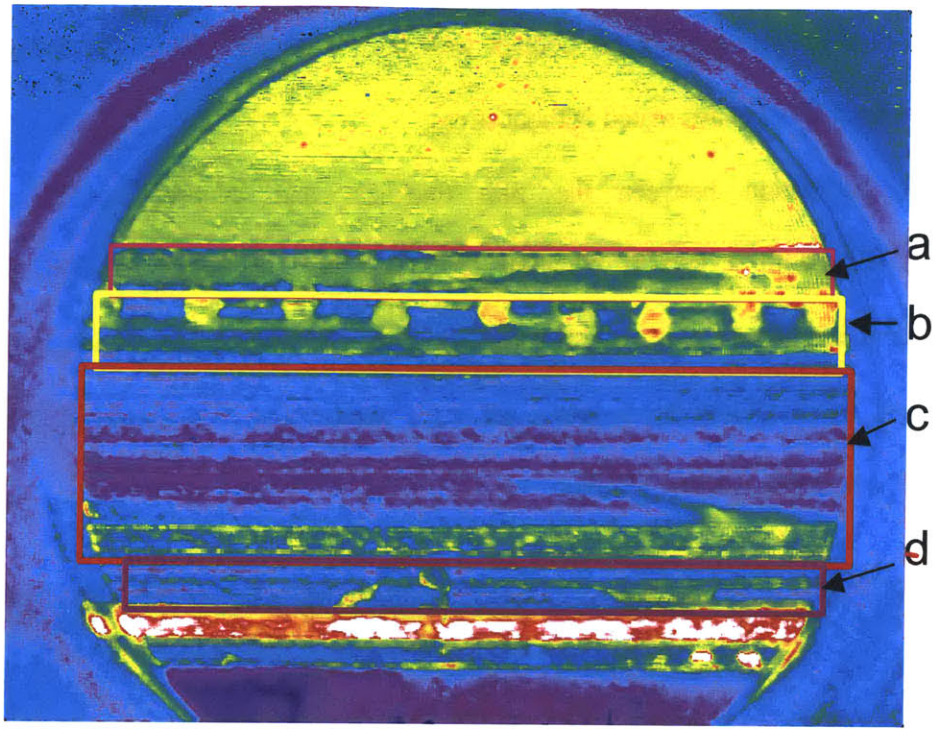

Figure 3.7: Layout of the regions a-d that will be referred to in the results and discussion section.

Region a encapsulates the area closest to the lip tip, where the film thickness is higher than region b. Both a and b were also chosen such that the meniscus movement was not included at any of the speeds. Region b also is the area where the holes were drilled for the last experiment. Region c is the transitional region where the contact or rollup region is located, and where the meniscus moves. Region d is closest to the dust lip.

3.4.2 Experimental Setup-Non-Linearity

The previous described calculations were all based on the assumption that the fluorescent and excitation intensities were linearly dependent. In reality, the thicker the film thickness, the less linearly the behavior. This translates into the lack of complete elimination of laser fluctuations even after taking the ratio. In order to compensate, a power law assumption is applied. By raising the numerator of the ratio to a power of Γ (where $\Gamma \leq 1$), the excitation intensity information from the ratio can be suppressed. When the proper non-linearity component is chosen, the spatial laser fluctuations are minimized. Figure 3.8 shows the progression of non-linearity with Γ.

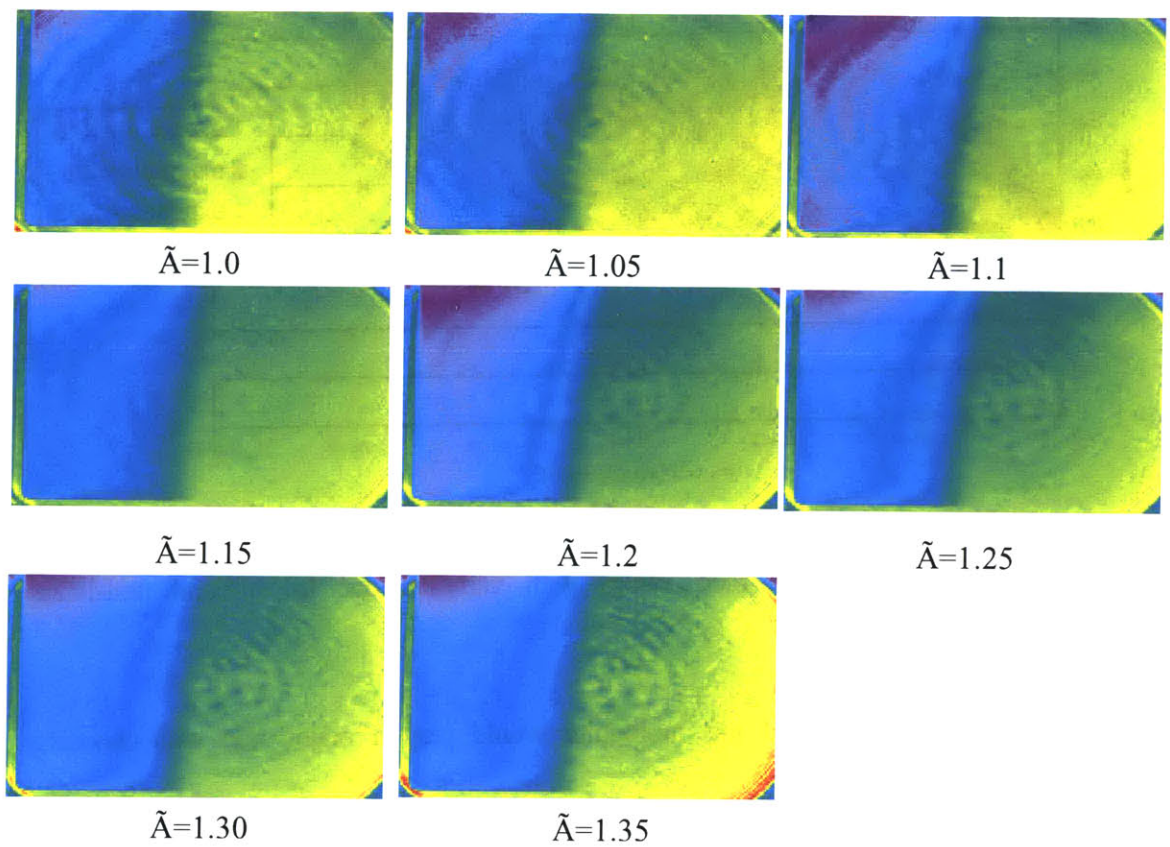

Figure 3.8 Spatial fluctuations with non-linearity component. Notice the fluctuations are a minimum between Ã=1.1-1.15 in the deeper regions (green or portion to the right of each image) and Ã=1.25-1.3 for the shallow regions (blue or left portion of each image).

As the figure shows, there was a distinction to a range within which the fluctuations decrease, but it proved to be extremely difficult to pin point a specific power. Also, the power that minimized the fluctuations in the thinner film region (blue area) appeared to be different than the power that minimized the thicker film region (green area). 1.25-1.3 appeared to minimize the shallow region while 1.1-1.15 seemed to minimize the deeper region.

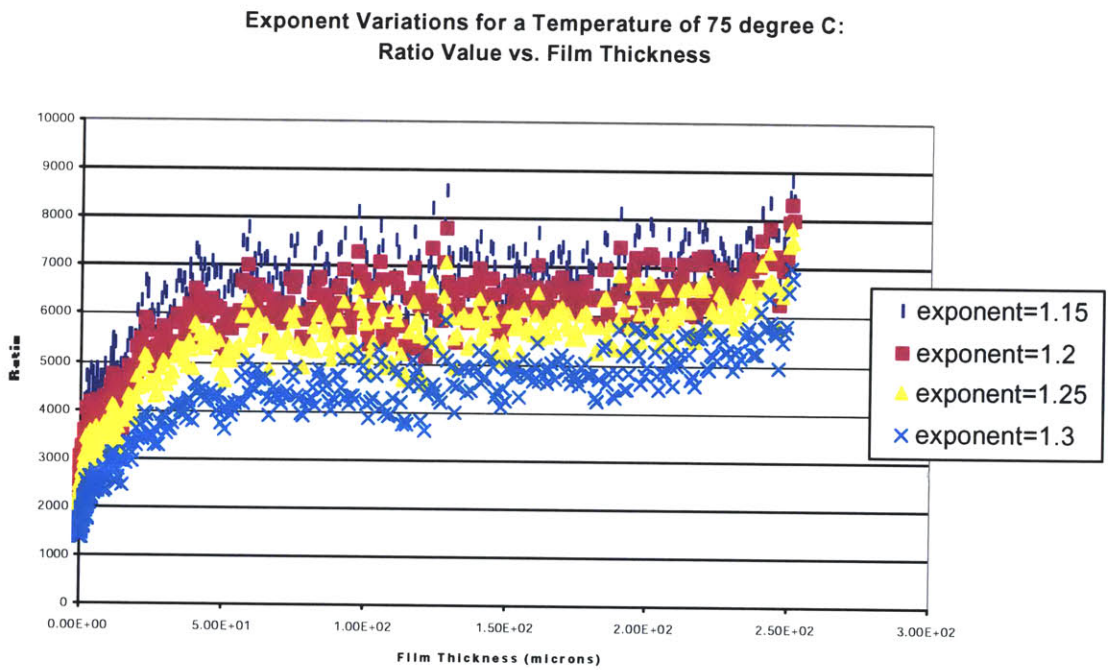

Figure 3.9: Comparison of the ratio values with variation due to different non-linear exponents.

In order to understand if this ambiguity would play a major role with choosing one exponent for the entire fixture, the film thickness measurements with each exponent were compared as in figure 3.9. For film thickness values less than approximately 20 microns, there would be a considerable amount of error if the improper exponent were to

be used. Another consequence of the lack of specific exponent clarity, was the lack of temperature recognition. The original technique for proper processing included the ability to recognize different non-linearity exponents at the various speeds to obtain the indirect measurement of temperature by matching the exponents to the calibrated images. This was assuming that there would be a distinction from temperature to temperature, which was not the case. A range could be pin pointed for the calibration images, but the range remained fairly constant over the temperature span (25 °C -150°C increments of 25 °C). Also, it proved to be next to impossible to differentiate from speed to speed any difference with changing exponent values. Once this was a recognized problem, an exponent was chosen that noticeably minimized the low frequency rings on the seal images, and then the corresponding calibration information that would be used was chosen by which one with the same exponent was also minimized. Though the deficiency in unique exponent recognition, the calibration proved to produce reliable information due to the lack of sensitivity to temperature fluctuations.

3.4.3 Experimental Setup-Dyes

Previous investigations tested out different types of dyes, concentrations, solubility in oil, bleaching effects, emission and absorption spectrums [14]. A further investigation was carried out by Dr. Carlos Hidrovo which mainly focused on combinations of five dyes. The ERLIF utilizes two dyes, one which reabsorbs (reabsorbing dye) the emission from the other dye (reabsorbed dye). The particular dyes that were chosen for these experiments were various concentrations of Pyrromethene 605 and Pyrromethene 650, with interference filter combinations of 580 and 610 respectively.

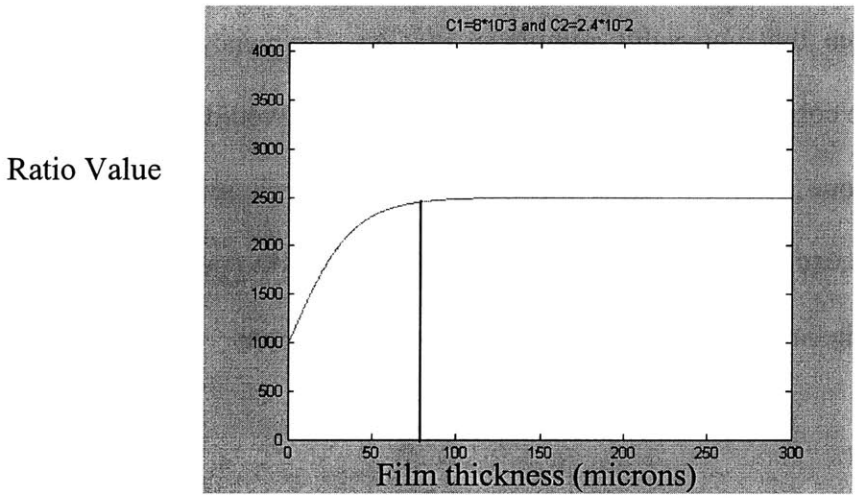

Figure 3.10 Profile of the ratio values as a function of film thickness based on the original dye concentrations. Vertical line allows for a rough estimate of what the cutoff film thickness values that can be calibrated based on the dye concentration.

The initial concentration of dyes used was C1= C (Pyrromethene 605) = $8*10^{-3}$ mol/L and C2=C (Pyrromethene 605) = $2.4*10^{-2}$ mol/L. Figure 3.10 shows that the expected range of film thickness that could be measured with this concentration would be approximately 0 microns up to 75-80 microns. From some of the initial seal tests with this system of dyes, the goal was to observe the activity of lubricating film thickness in a

thin film region (0-2 microns) and thicker film regions within the grooves themselves. In order to obtain more information within the grooves, variations of the concentrations of each of the above named dyes were tried. Figure 3.11 shows the respective profiles that would be expected with the changes.

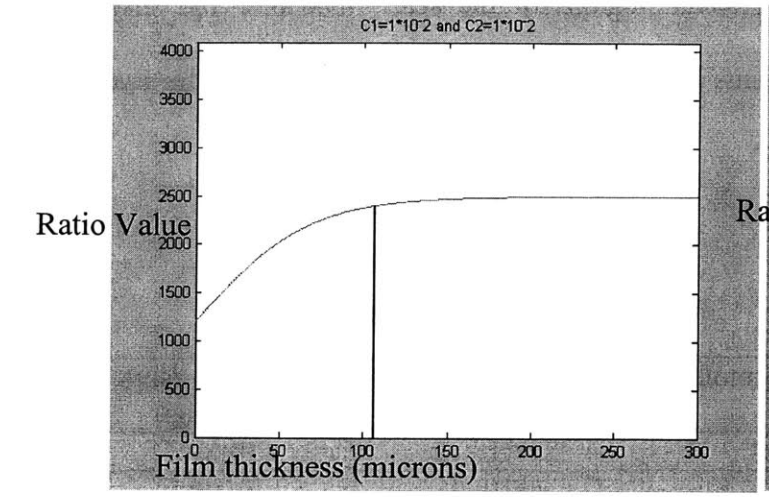

(a)

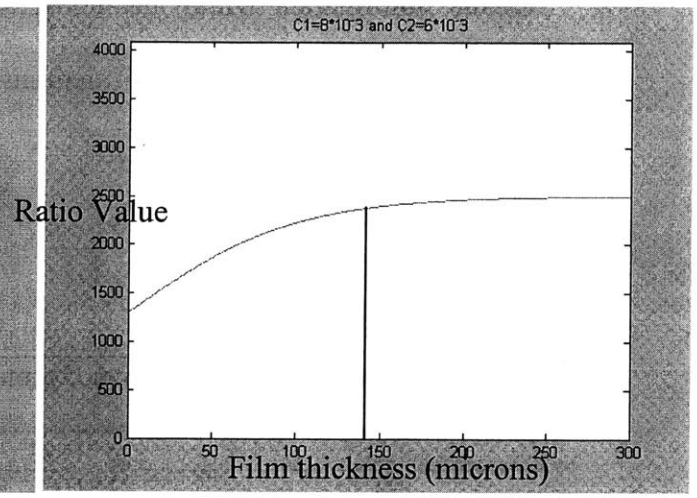

(b)

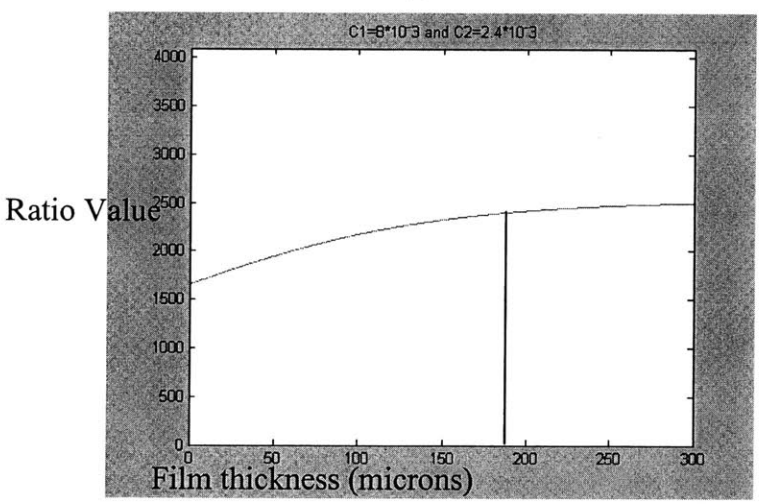

(c)

Figure 3.11 Profiles for (a) $C_1 = C_2 = 1*10^{-2}$ mol/L, (b) $C_1 = 8*10^{-3}$ mol/L & $C_2 = 6*10^{-3}$ mol/L, and (c) $C_1 = 8*10^{-3}$ mol/L & $C_2 = 2.4*10^{-2}$ mol/L.

Figure 3.11 shows how the profile gets stretched out with each changing of the concentration levels of the dyes. Out of these 3 different variations, option (b) was the one that was finally chosen. This option, in theory would provide information from approximately 0-200 microns. Another reason for the dye selection was the lack of reliable information within the non-grooved regions of the seal. The new dye also allowed for monitoring of the meniscus in some instances. A summary of the dye combinations is given in table 3.1.

Table 3.1: Dye Concentrations

Dye combination	C(pyr-605) (mol/L)	C(pyr-650) (mol/L)	Thickness range (microns)
1	8*10^-3	2.4*10^-2	0-80
2	1*10^-2	1*10^-2	0-100
3	8*10^-3	2.4*10^-3	0-145
4	8*10^-3	6*10^-3	0-190

3.4.4 Experimental Setup-Data Collection

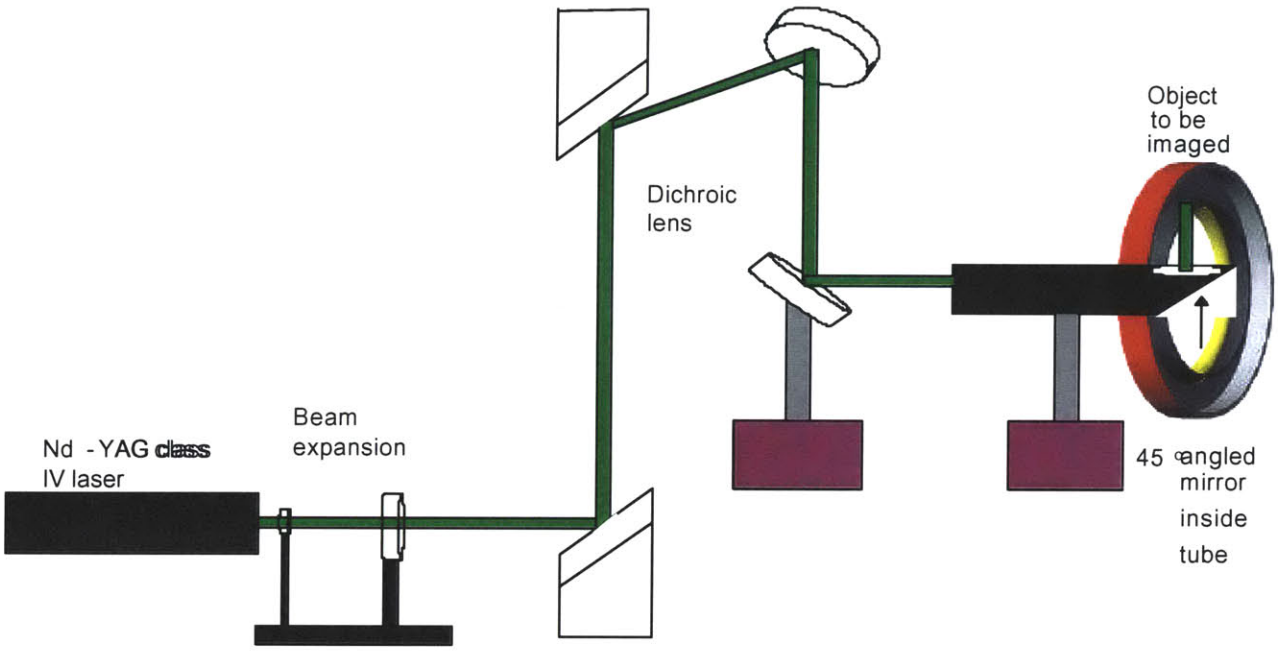

(a)

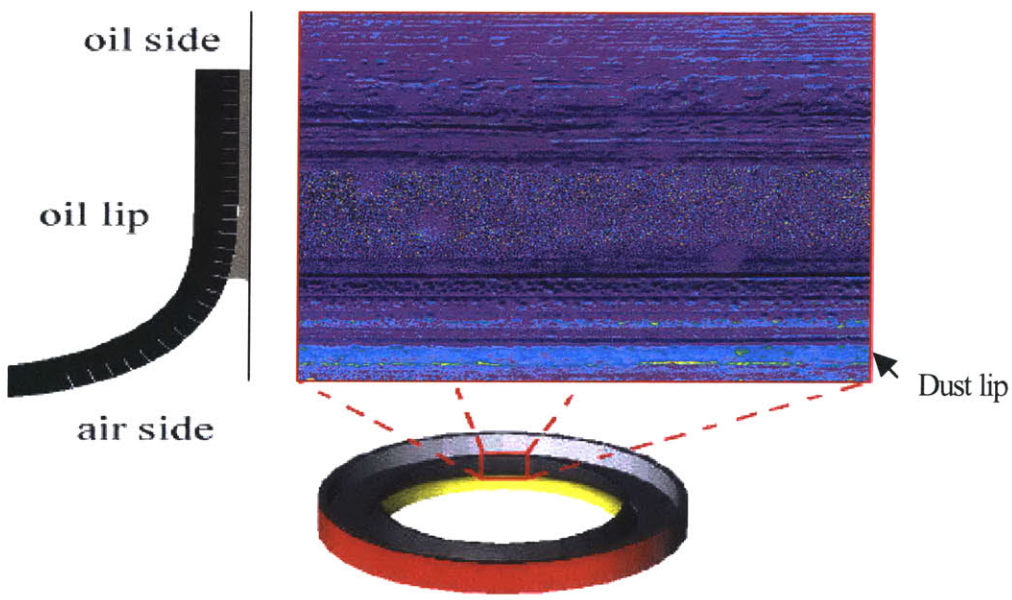

(b)

Figure 3.12: (a) is a schematic of how the optics were setup for capturing the image of the seal shown in (b).

4.1 Results and Discussion

There were a total of five different seals that were tested, all of which are listed in table 4.1, with a depiction of the angle theta in figure 4.1.

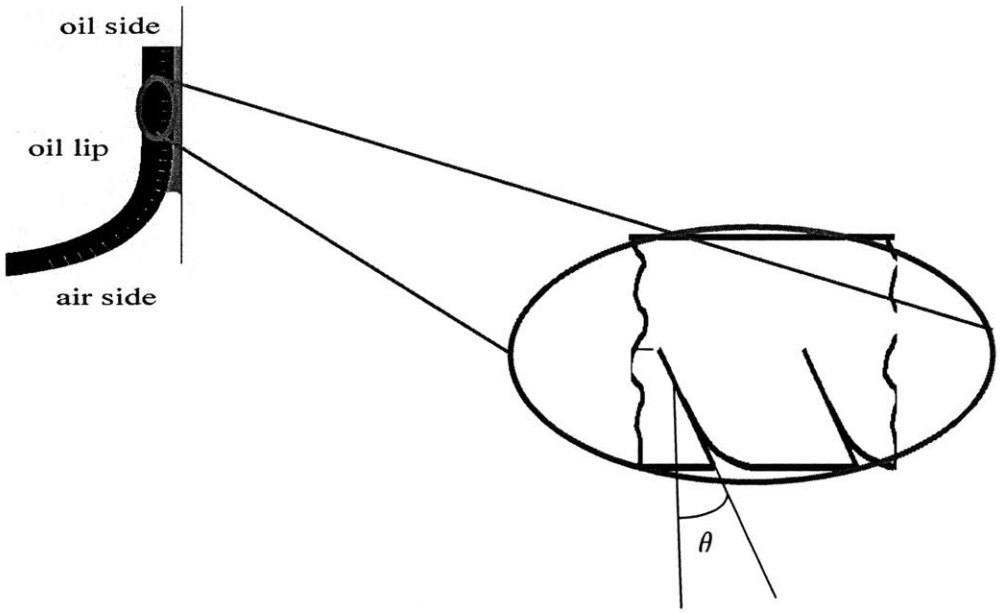

Figure 4.1: Depiction of the angle (θ) at which the seal type refers to in table 4.1.

Table 4.1: Seals tested

Seal Type (θ)	Dye Concentration from table 3.1
Production Seal (35°)	1
Plain Seal (90°)	1
0°, Full spiral (0°)	1
Production Seal (35°)	4
15°, Full spiral (15°)	4
Production Seal with holes(35°)	4

The production seal is the seal that Caterpillar uses presently, the others are variations on the angle, θ, at which the grooves are cut into the seal.

The experiments involved collecting data at different speeds, ramping up then back down in the specified increments. Each test also required a new calibration for the proper processing.

4.2.1 Results and Discussion-Production Seal-Dye 1

Figure 4.2 shows the calibration data and the corresponding best fit that was used for the calculation of thickness values.

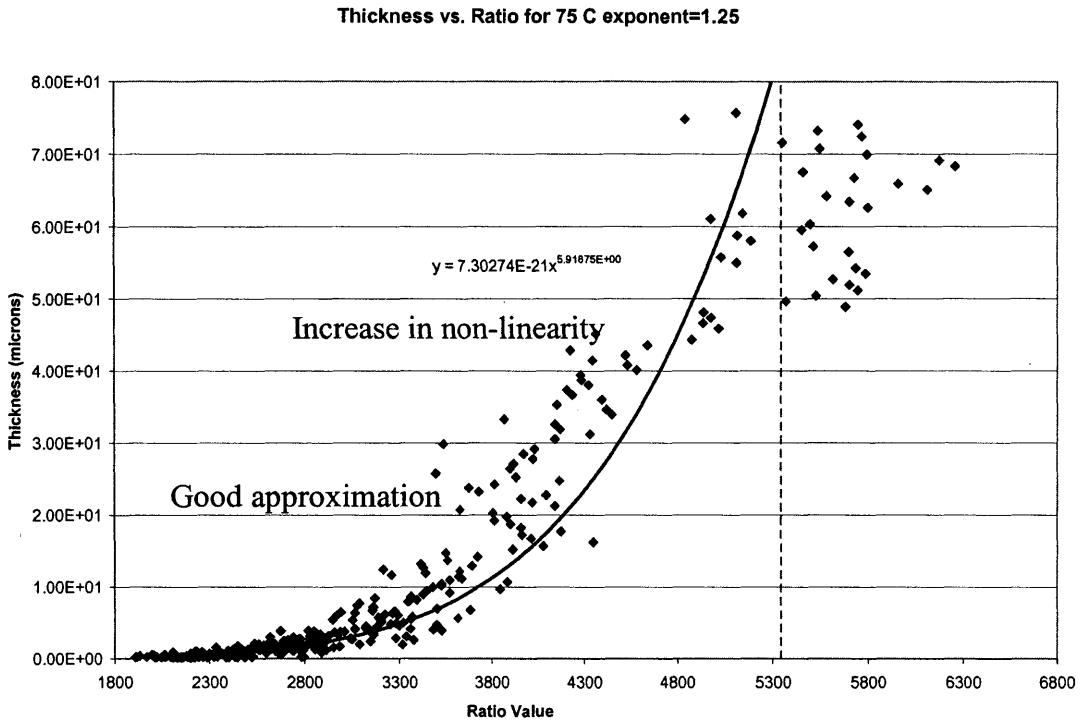

Figure 4.2: Calibration used for the production seal with dye 1. The red dotted line shows where the cutoff was located (approximately ratio value=5348).

The range of measurable thickness was 0.19-85 microns. There was a fairly close fit from 0.19-17 microns, however, beyond this point, the non-linearity increased.

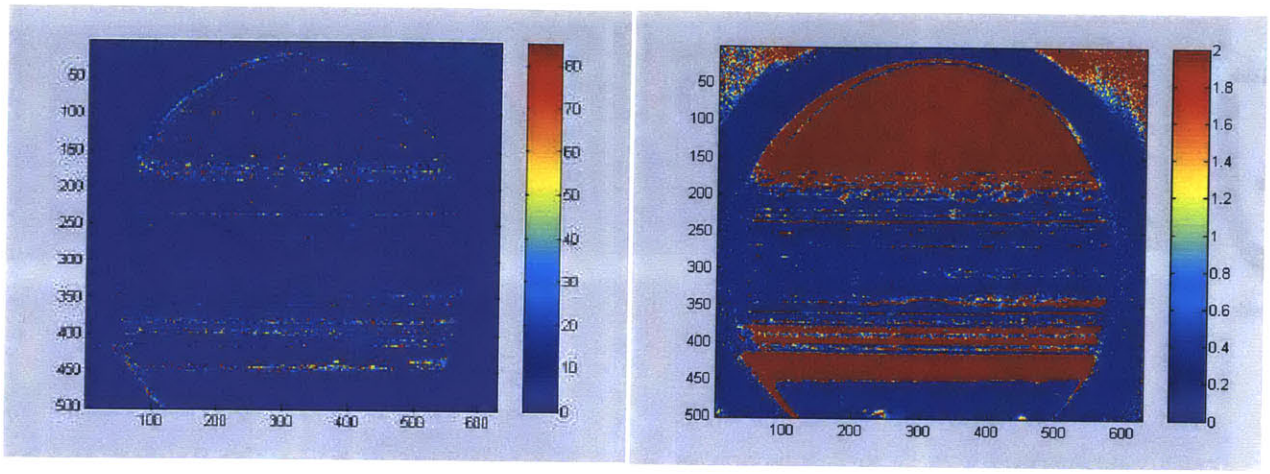

Figure 4.3: Thickness image of the seal at 300 rpm with a scale of 0-85 microns (left) and 0-2 microns (right).

It was difficult to see much detail in the images. A majority of the seal was binary, either above or below the calibrated range (blue regions in the left image in figure 4.3). To get more insight of the thickness variations, the scale was limited to 2 microns instead of 85 microns, which was what was used for the remaining images of the seal shown in figure 4.4.

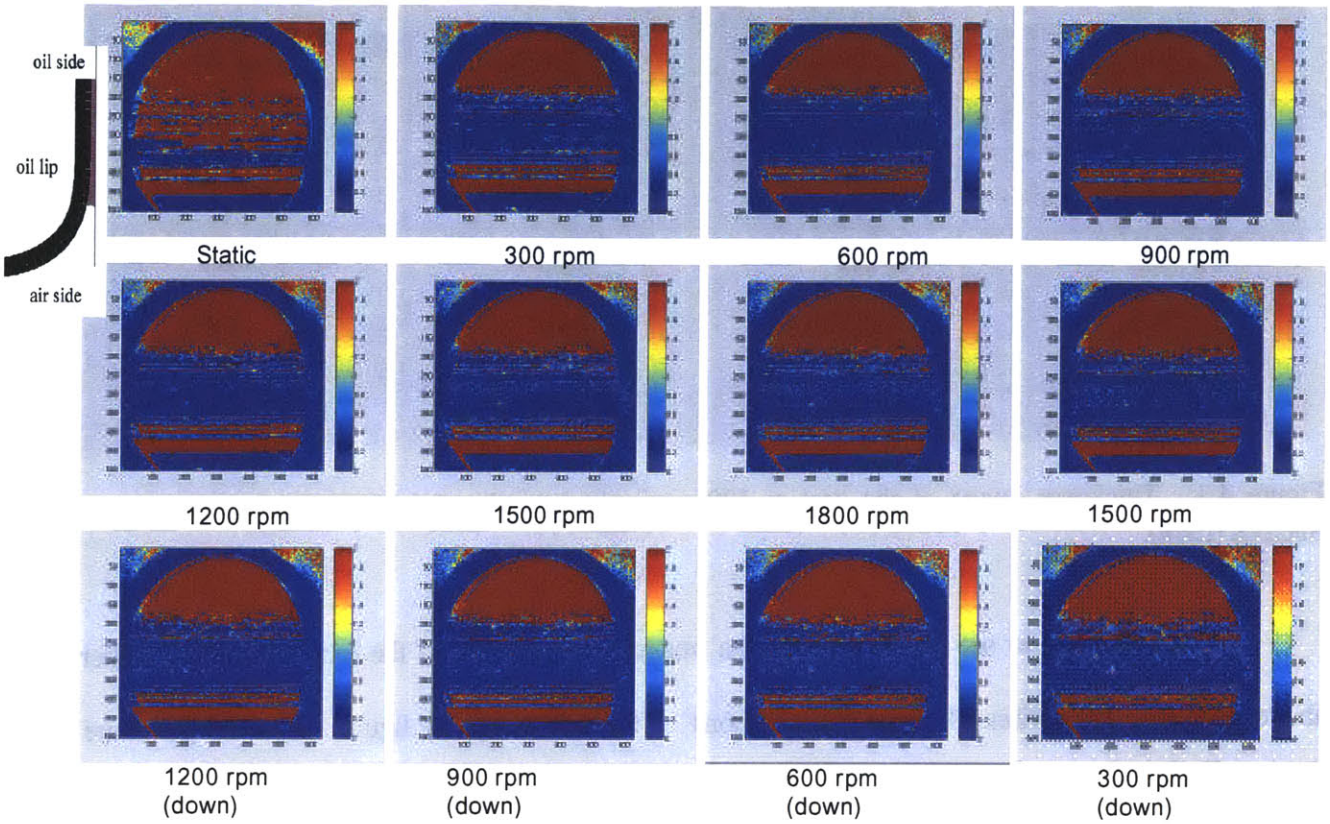

Figure 4.4: Progression of film thickness with shaft speed. The range is from 0-2 microns. Notice how the images appear to be extremely binary, i.e., values were not in the range that the calibration could provide.

From figure 4.4, the seal is still binary; saturated (mauve regions which represent anything above or equal to 2 microns) or the film thickness was so thin that it was not detectable by the calibration (blue regions, anything less than or equal to 0.17 microns). As expected, the film thickness of the seal in the static condition was much higher (mauve regions) when compared to the dynamic case. Also, once the shaft started rotating, the seal did not change significantly as the speed was ramped up and back down.

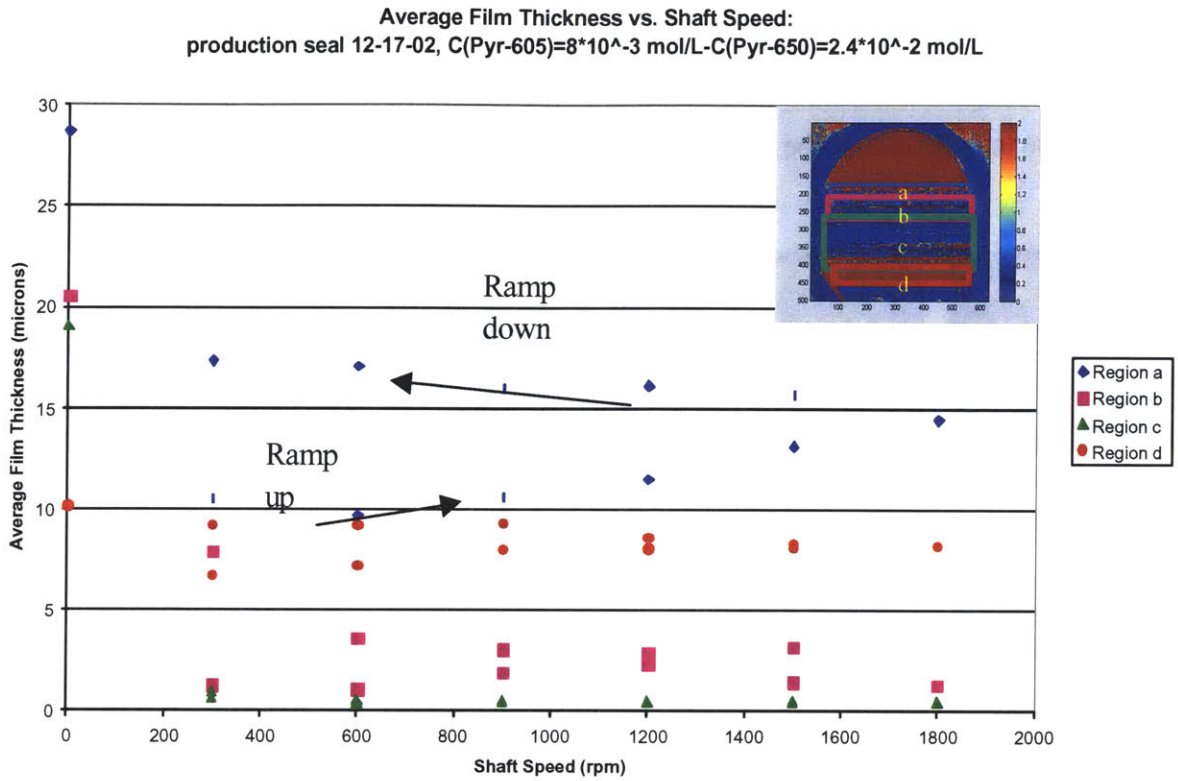

Figure 4.5: Production seal-dye 1-average film trend with shaft speed. There is not much difference in the ramping up or down in speed for regions b-d, but a shows the largest difference. Also, there is a noticeable jump from 0 to 300 rpm.

The values in figure 4.5 were calculated based on a translation of the ratio image of the seal into thickness measurements based on the calibration (values of film thickness at each pixel location from figure 4.2). The values represented are only those that fall within the ratio values of 1906 and 5348 (which correlate to 0.19 and 85 microns respectively), non-inclusive.

Regions a and b had the most change, regions c and d stayed relatively constant over the velocity changes. Region c contained the region where the seal came in most contact with the shaft. When the seal was stationary, the pressure difference coupled with surface tension, allowed for oil to seep out, and when the shaft started rotation, oil was pumped back towards the oil sump, which was observed through looking at the meniscus locations, figure 4.6.

Notice, region a film thickness values were smaller while ramping up compared to ramping down. This contradicts intuition since the highest amount of oil is present at 0 rpm, therefore the film thickness should be thicker.

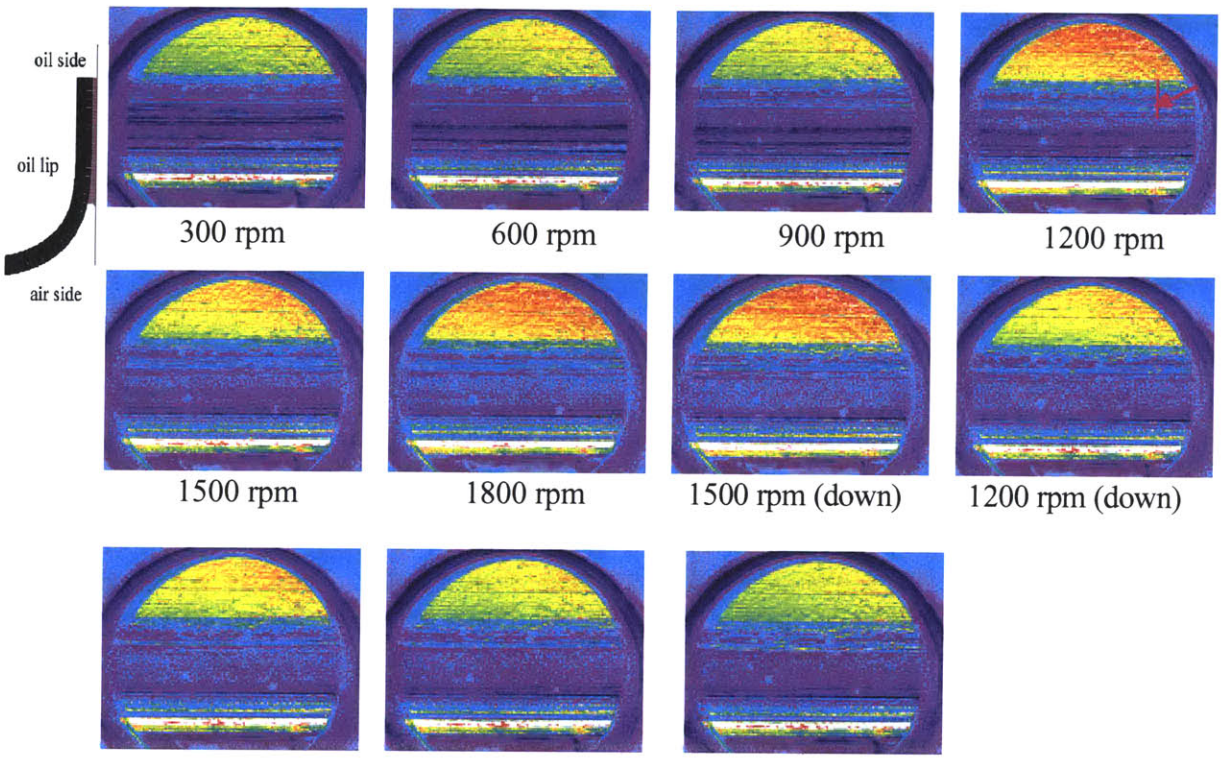

Figure 4.6: Tracking of the meniscus movement over the speed changes. The location was not obvious until around 900-1200 rpm, at which point, it did not move a noticeable distance.

Table 4.2: Meniscus location from the lip tip of the seal

Speed (rpm)	Distance (pixels)	Distance (mm)
300	n/a	n/a
600	n/a	n/a
900	86.0523	3.402353048
1200	88.0227	3.480259117
1500	85	3.360747
1800	88.0227	3.480259117
1500	94.0851	3.719955501
1200	89.1403	3.524447009
900	84.0952	3.324972837
600	80.2247	3.171940234
300	77.0584	3.046750431

Movement of the meniscus was not obvious as figure 4.6 and table 4.2 show. In fact, the location of the meniscus was not even detected until 900 rpm.

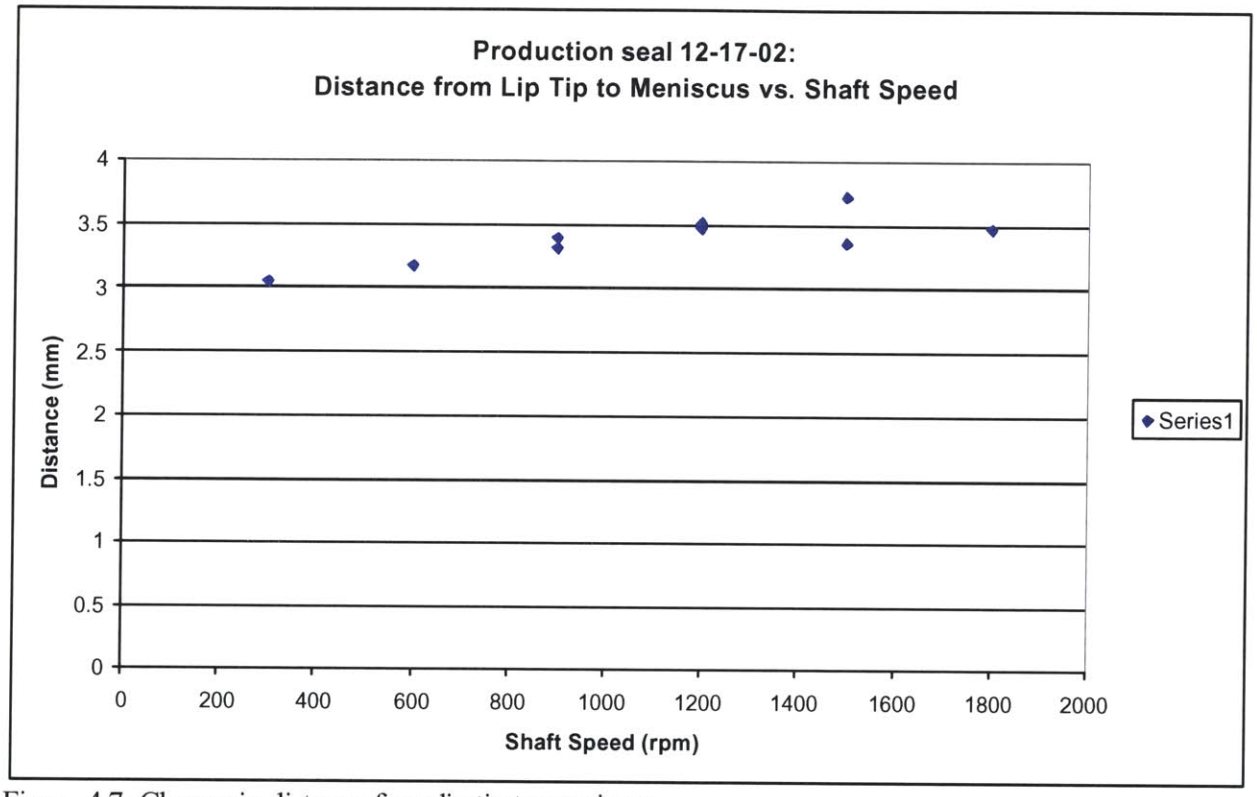

Figure 4.7: Change in distance from lip tip to meniscus.

The meniscus location should stay relatively constant if there is a balance between axial leakage and reverse pumping. If there were too much reverse pumping, the meniscus would get ingested toward the lip tip and overpower the effects of leakage, resulting in the meniscus not moving back out towards the dust lip. Conversely, if the reverse pumping were overpowered by leakage, the meniscus would tend to move more towards the dust lip. Figure 4.7 shows that the meniscus stayed around the same position.

To ensure that the film thickness values that were being calculated were a proper representation of what the calibration could properly measure, the MATLAB program used included only those values that were between the minimum and maximum, non-inclusive (F percentage plots described below). Additionally, it was also desirable to observe how many values were actually below (D) and above (E) these limits, which are presented as percentages (figure 4.8).

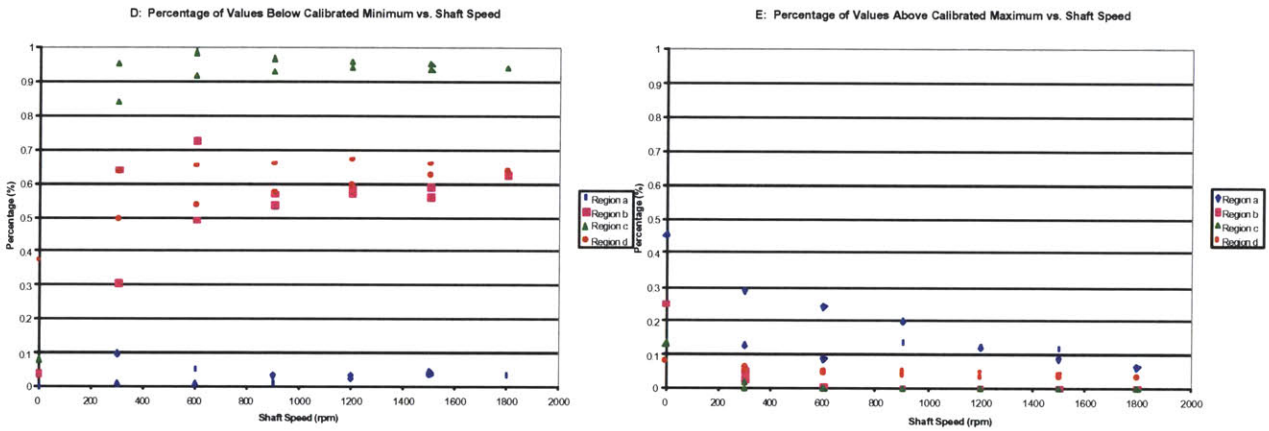

(D) (E)

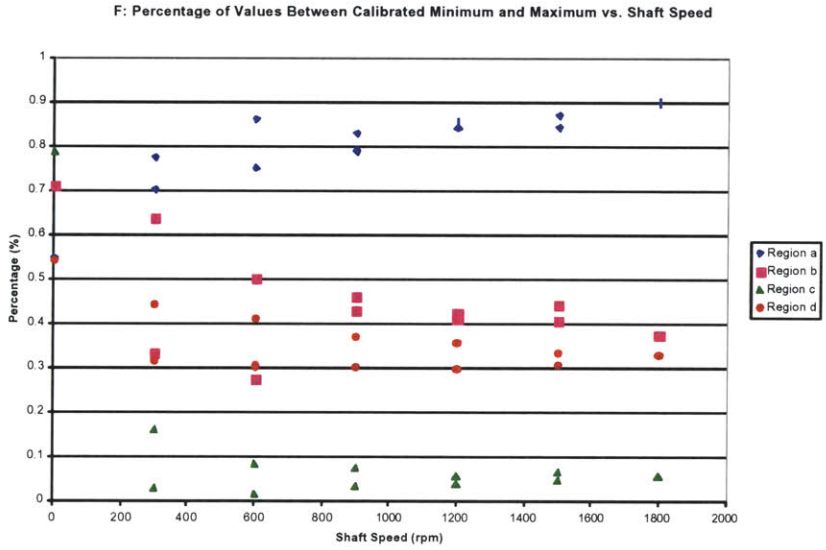

(F)

Figure 4.8: Percentage of thickness values that are (D) below, (E) above, and (F) within the calibrated range. Though there was a majority of values that fell within the calibrated range, region a had values that were above the maximum thickness value.

4.2.2 Results and Discussion-Plain Seal (90°)-Dye 1

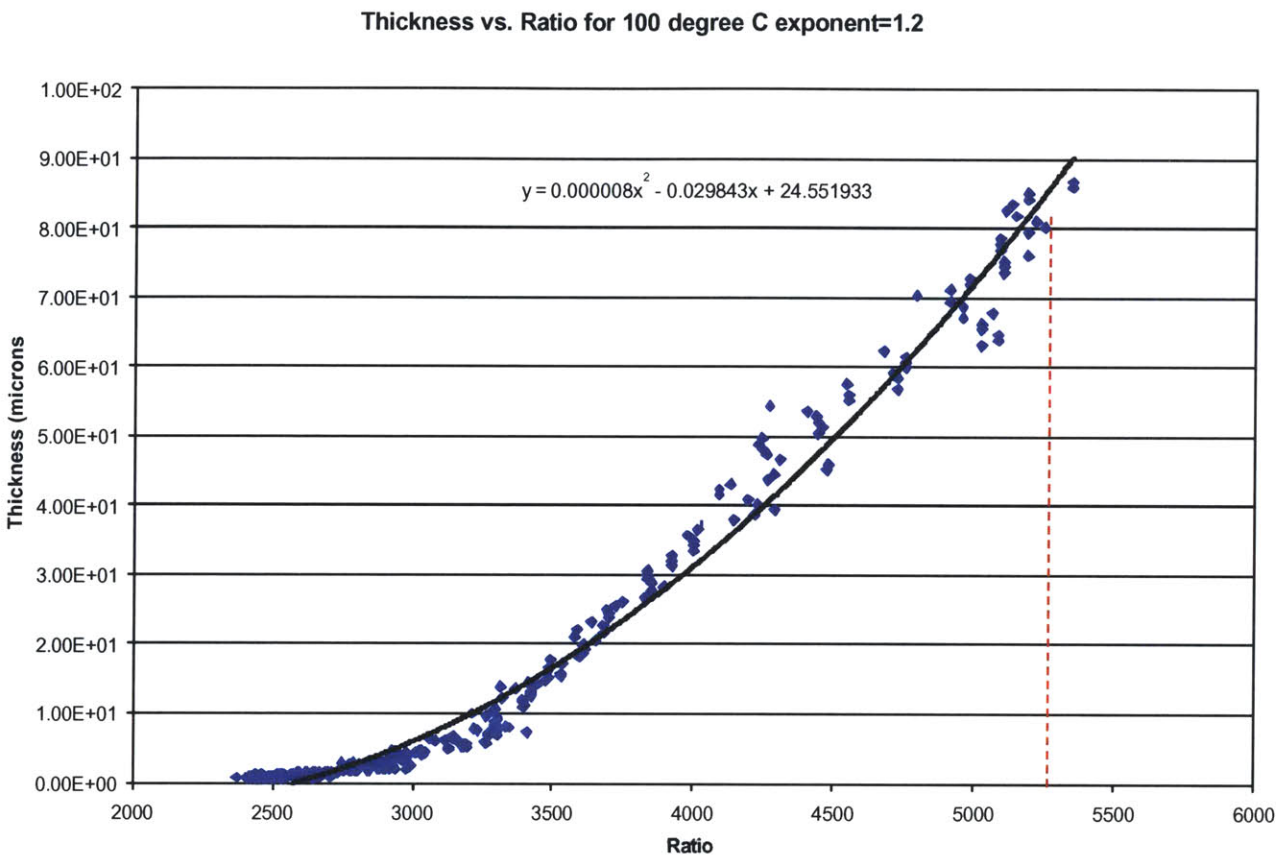

Figure 4.9: Plain seal-dye 1-calibration, red dotted line signifies the cutoff ratio value (~5346).

Range for the calibration was 2650 to 5346 (0.83-90.32 microns). The best fit correlated much better to the data than the previous test.

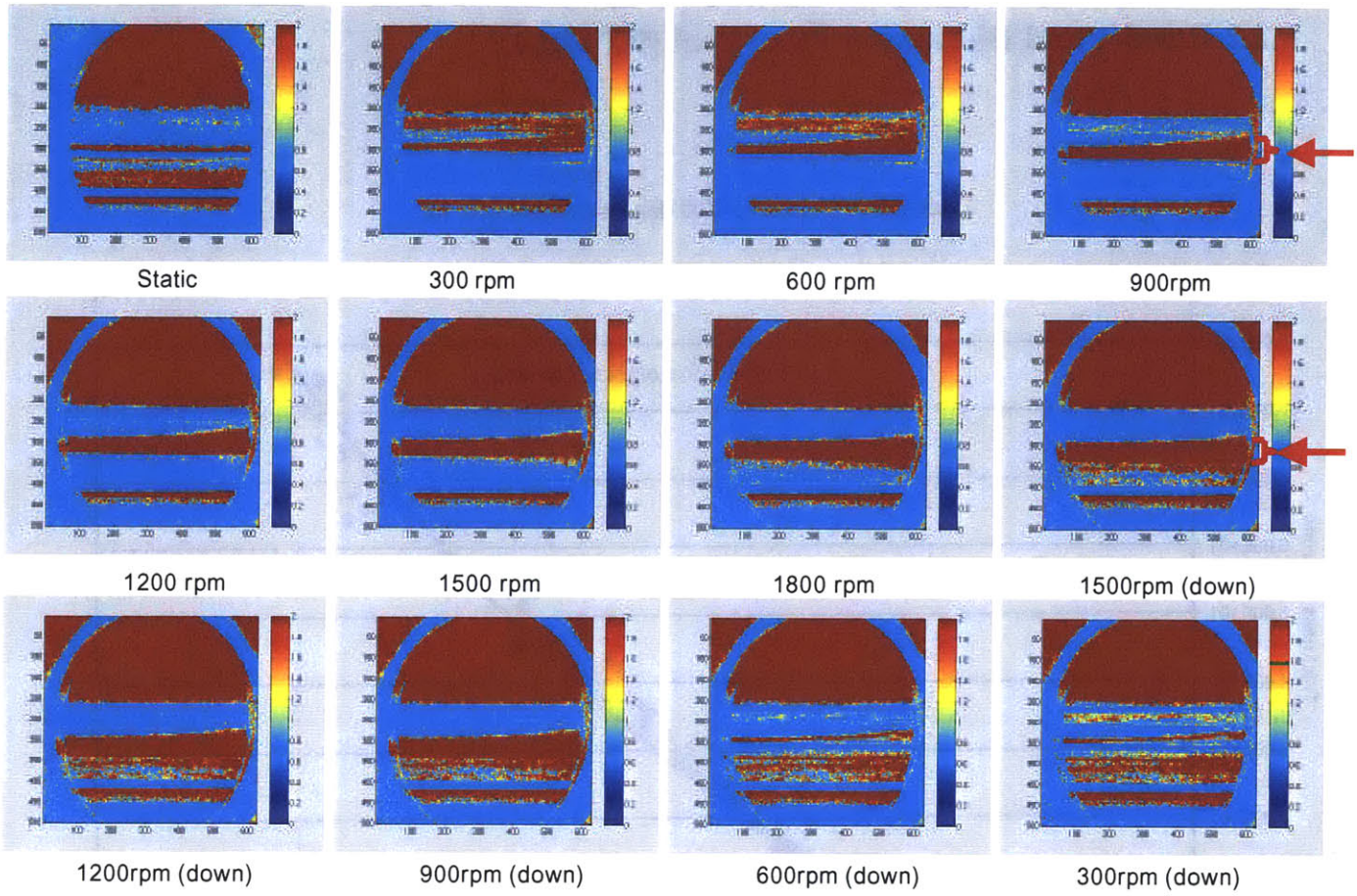

Figure 4.10: Thickness images for plain seal over the speed range. The arrows mark the general vicinity of the contact region.

The contact region was easier to locate with this seal (marked by the red arrows); however, the meniscus distance from the lip tip was not well defined. Though there still were thickness values above the maximum, there were more values that were within the range (light blue regions compared to the dark blue regions in figure 4.4).

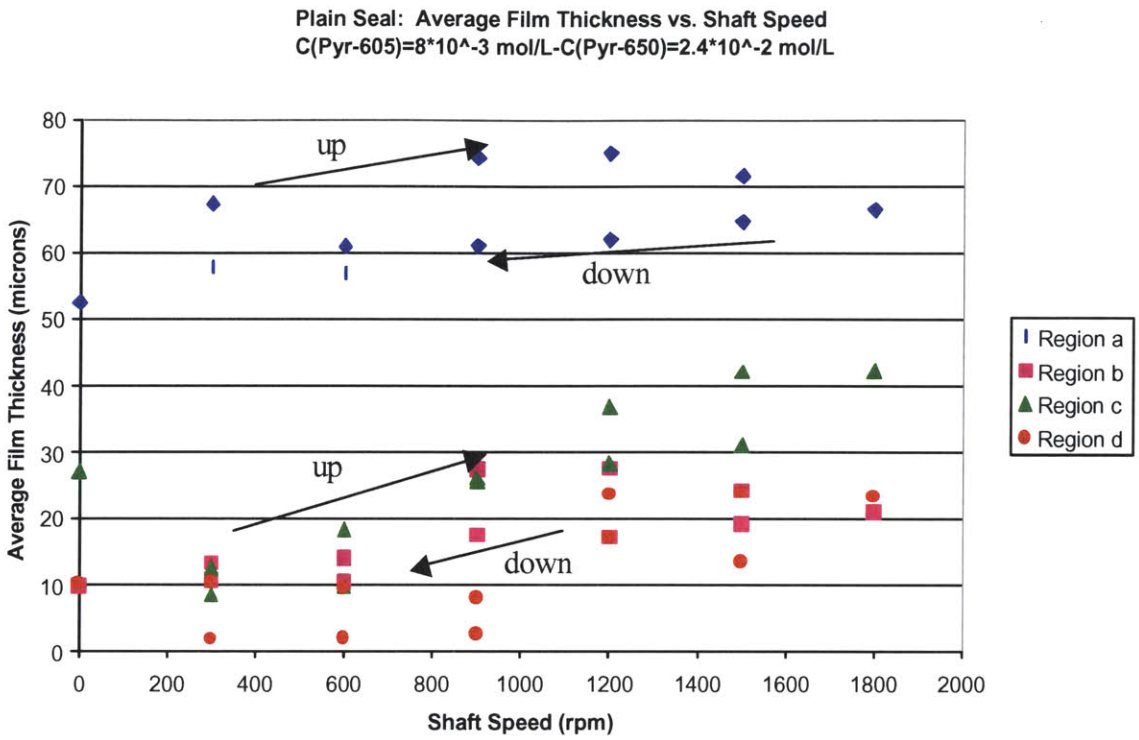

Figure 4.11: Plain seal-dye 1-average film thickness value progression with shaft speed. This seal showed higher average film thickness values with ramped up in speed than down. Also, the average film thickness appeared to be increasing with shaft speed instead of decreasing like was predicted with theory.

The film thickness for the plain seal was approximately double the values of the previous production seal test. The plain seal must rely on microgeometry for leakage control due to the lack of grooves, which was discussed in the introduction and relates back to the formation of microasperities. The results reiterate the benefits of the grooves. As the shaft speed increased, the film thickness increased instead of decreasing as in figure 4.5, showing the instability of the seal. Ironically, this particular seal did not leak.

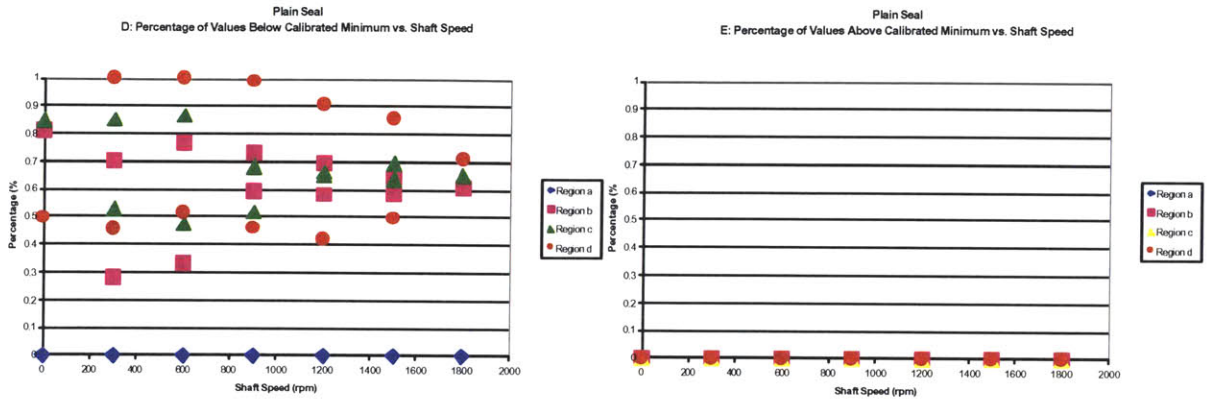

(D) (E)

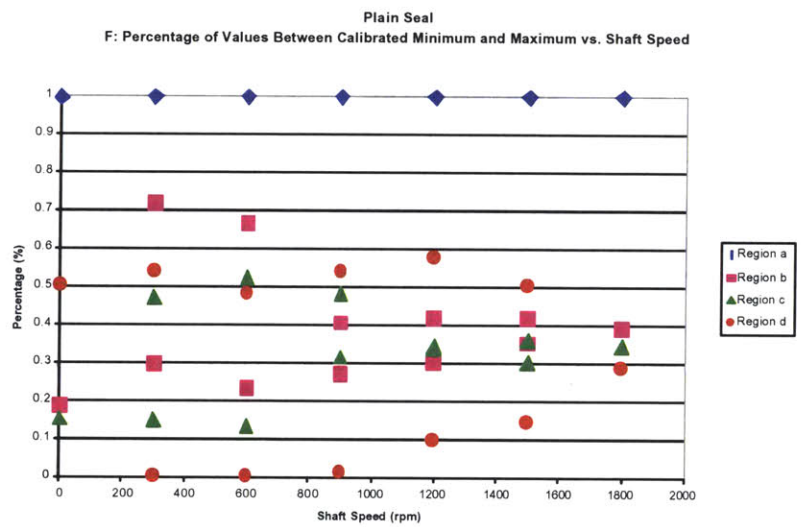

(F)

Figure 4.12: Percentage of thickness values that are (D) below, (E) above, and (F) within the calibrated range.

The plain seal thickness measurements were below or within the range of the calibration.

4.2.3 Results and Discussion-0 degree, Full Spiral-Dye 1

From the previous tests (figure 4.5 and 4.11), the film thickness trend for the ramping up in speed varied from the ramping down. Exploration of this phenomenon was accomplished by execution of two consecutive tests (run 1 and 2), without allowing the shaft to come to rest between the two separate data collections. This method was applied for this and subsequent seals.

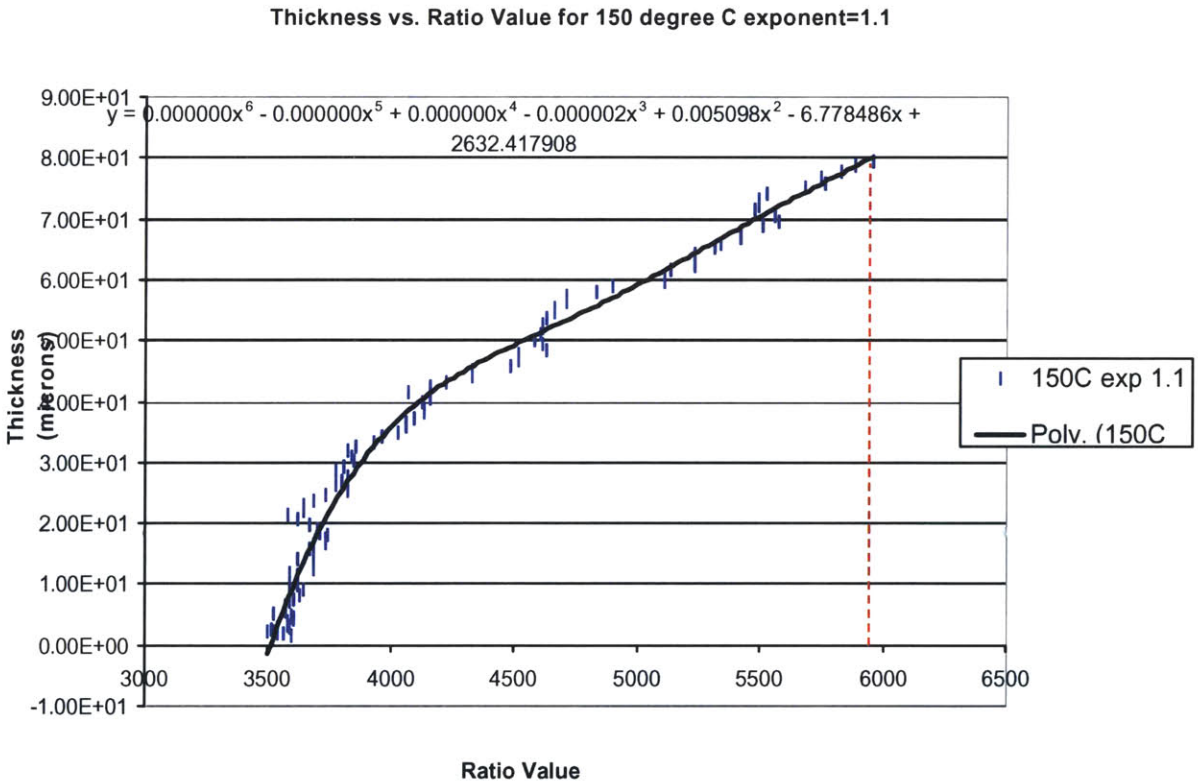

Figure 4.13: 0 degree seal-dye 1-calibration curve, with the red dotted line showing the maximum. The calibrated range for the 0 degree seal was 3520-5954 (0.97-80.19 microns).

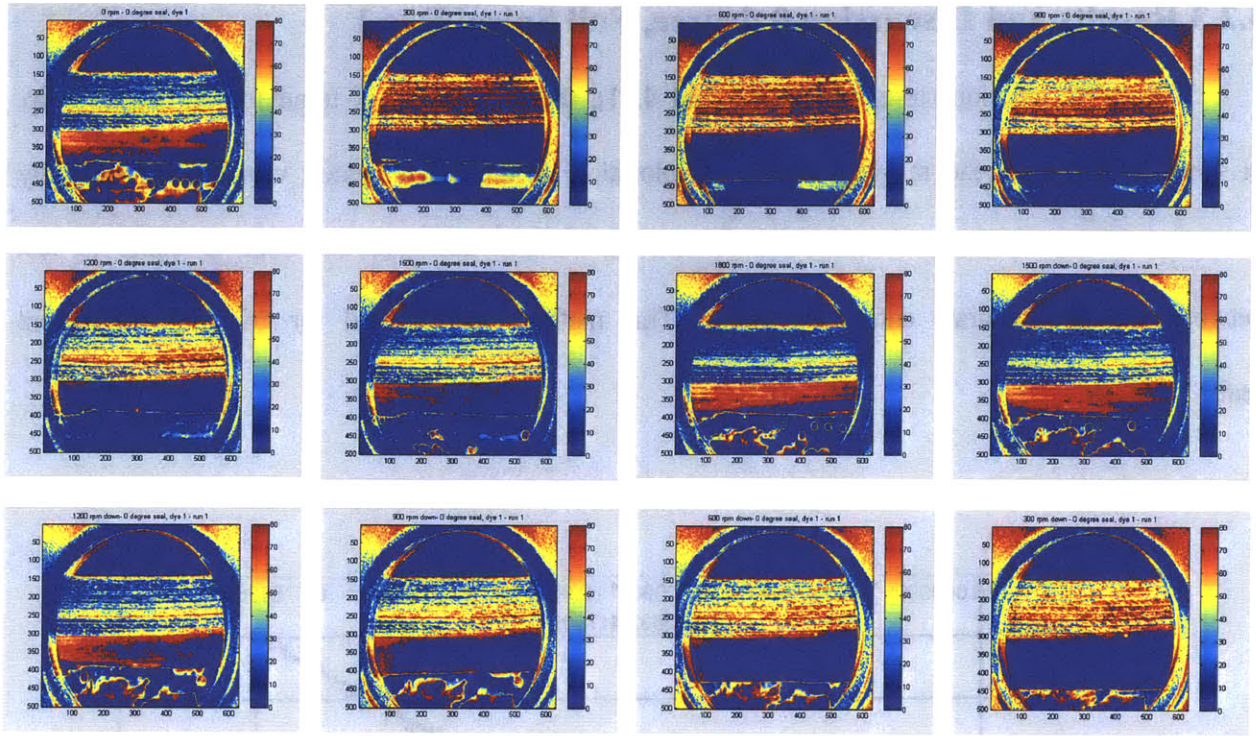

Figure 4.14a: Progression of film thickness with shaft speed images of 0 degree seal–run 1, first image being in the static condition.

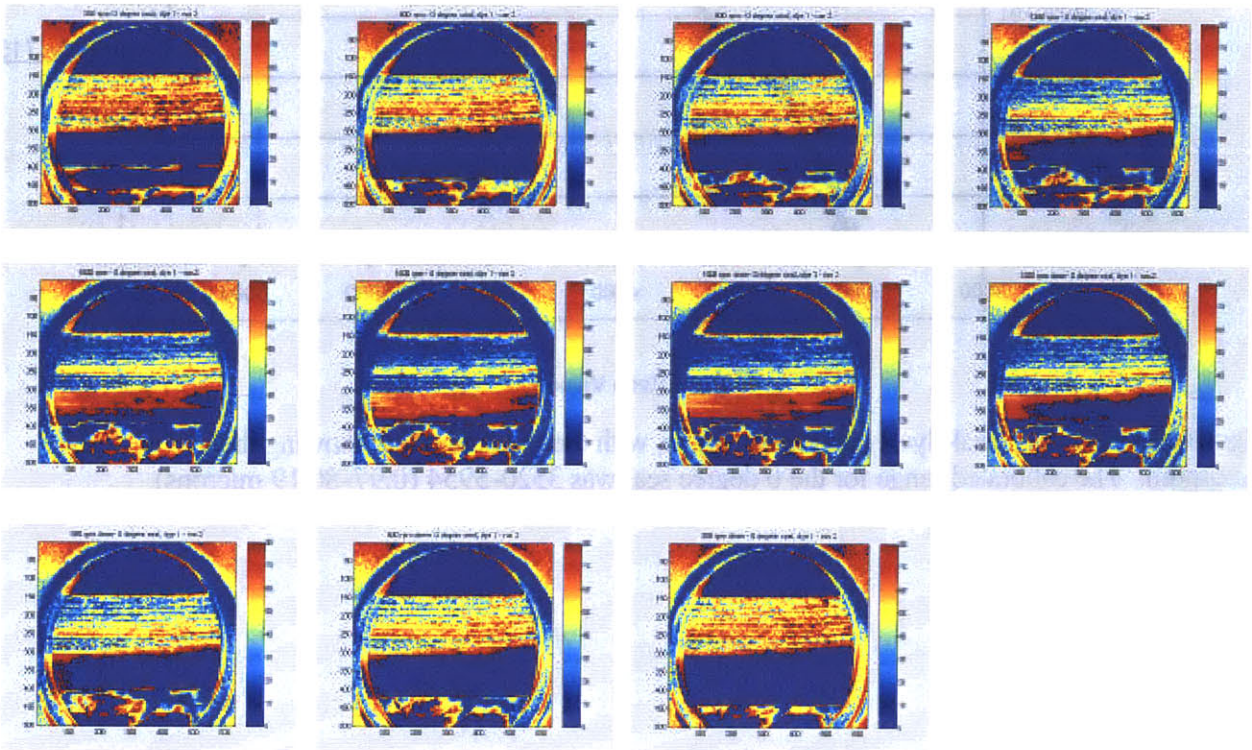

Figure 4.14b: Progression of film thickness with shaft speed images of 0 degree seal–run 2, the first image being at 300 rpm.

In both test runs, the region closest to the dust lip appeared to be flooded, which may have been due to the initial installation of the seal. The production and plain seals were both pre-assembled in the standard metal casings that were sent from Caterpillar. The seals with any other angle variation had to be manually assembled. Once assembled, this seal curled up when attempting to install it.

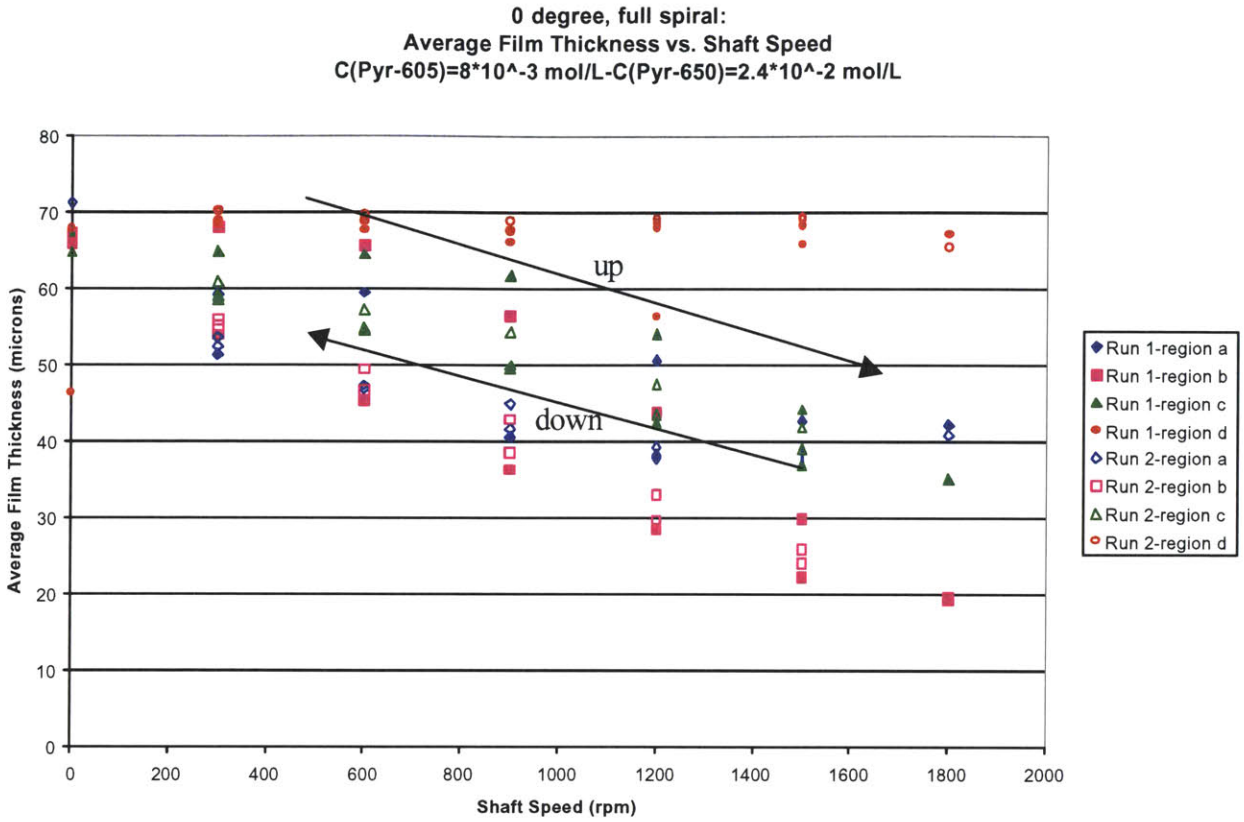

Figure 4.15: Progression of average film thickness for 0 degree seal-run 1 and 2. This seal at least depicted the predicted trend of decreasing film thickness with speed.

Region d had the highest values, presumably because of the seal deformation that was discussed. This trend of the film thickness decreasing with increased shaft speed was what was predicted. The film thickness was higher during the ramp up in shaft speed than the ramp down. The film thickness values for the second run followed more along the film thickness values for the initial ramp back down in speed, without as much of a difference between the ramp up and down.

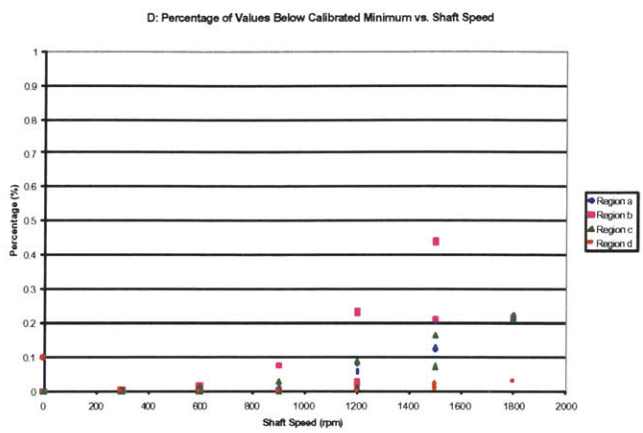

(D)

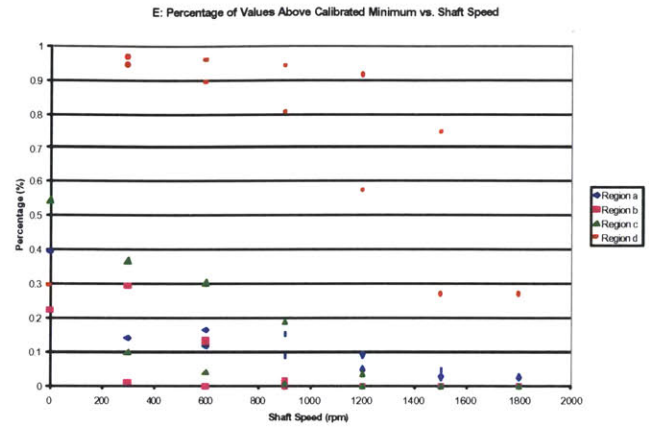

(E)

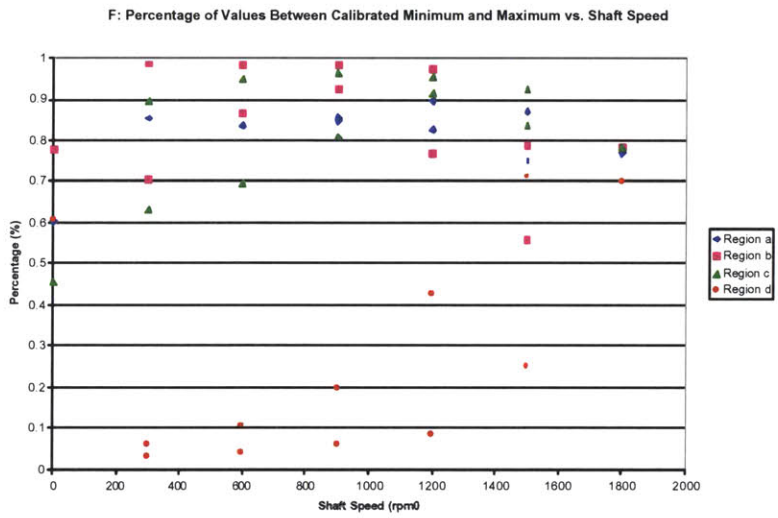

(F)

Figure 4.16: 0 degree-dye 1, percentage of thickness values that are (D) below, (E) above, and (F) within the calibrated range. Unlike the plain seal, a majority of the film thickness values exceeded the maximum calibrated value.

Again, a majority of the values were within the range or above it. Region c and d had much higher values, but again, that was most likely because of deformation.

Dye 1 was aimed at focusing on thin films (~1 micron) and as the above data has shown, the data was <1 micron. Even though there were values below the minimum, without designing a completely new method for calibration, the next logical and feasible step was manipulation of the dye concentration (discussed in the experimental setup).

4.2.4 Results and Discussion-Production Seal (35°)-Dye 4

For this and the subsequent seals, two variations on the initial speed test were implemented. The first was the ability to monitor the activity of the film thickness in the lower rpm range, since there existed a large transition in film thickness from the static (0 rpm) to 300rpm. The lower rpm range refers to 85-300 rpm, increments of 10 rpm, which was determined by the limitations of the test rig.

The second modification dealt with observing if the film thickness would deplete at a maximum rpm. Again, due to test rig limitations, the maximum speed was set to 2100 rpm.

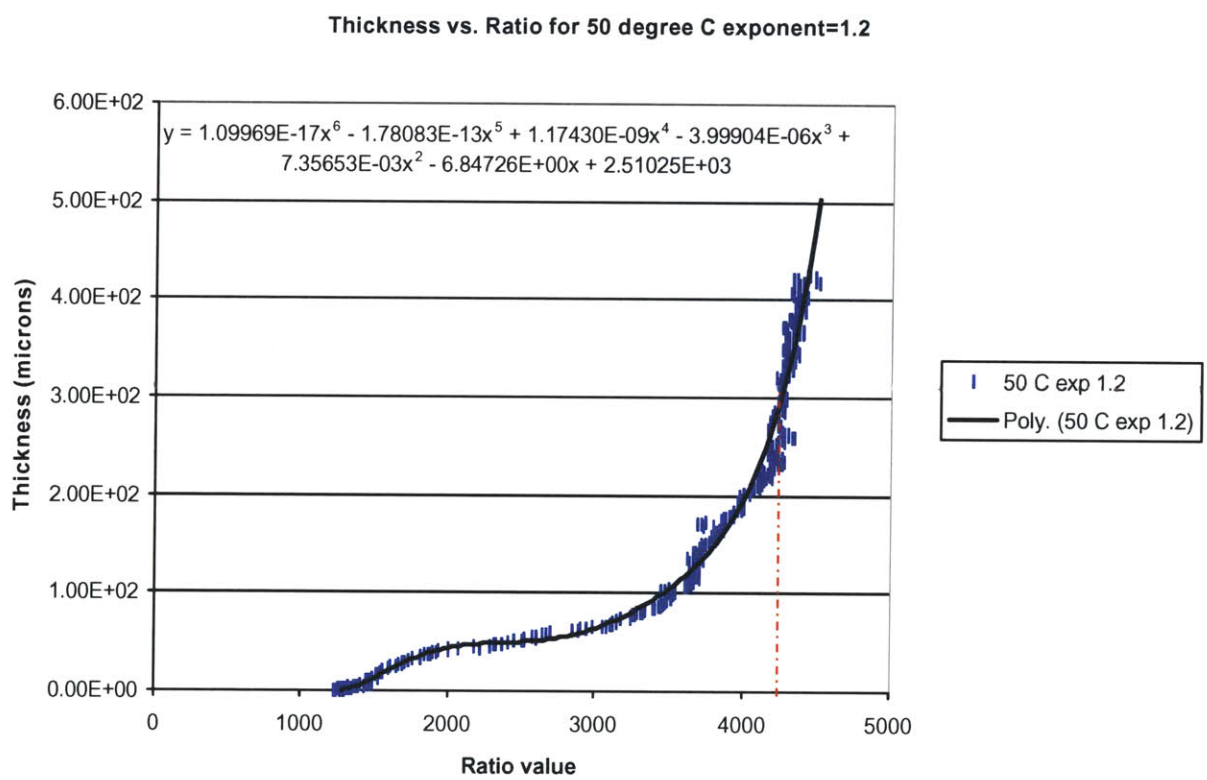

Figure 4.17: Production seal -dye 4 calibration, maximum at the red dotted line.
The dye concentration allowed for a range of 1280-4278 (0.82-311.08 microns).

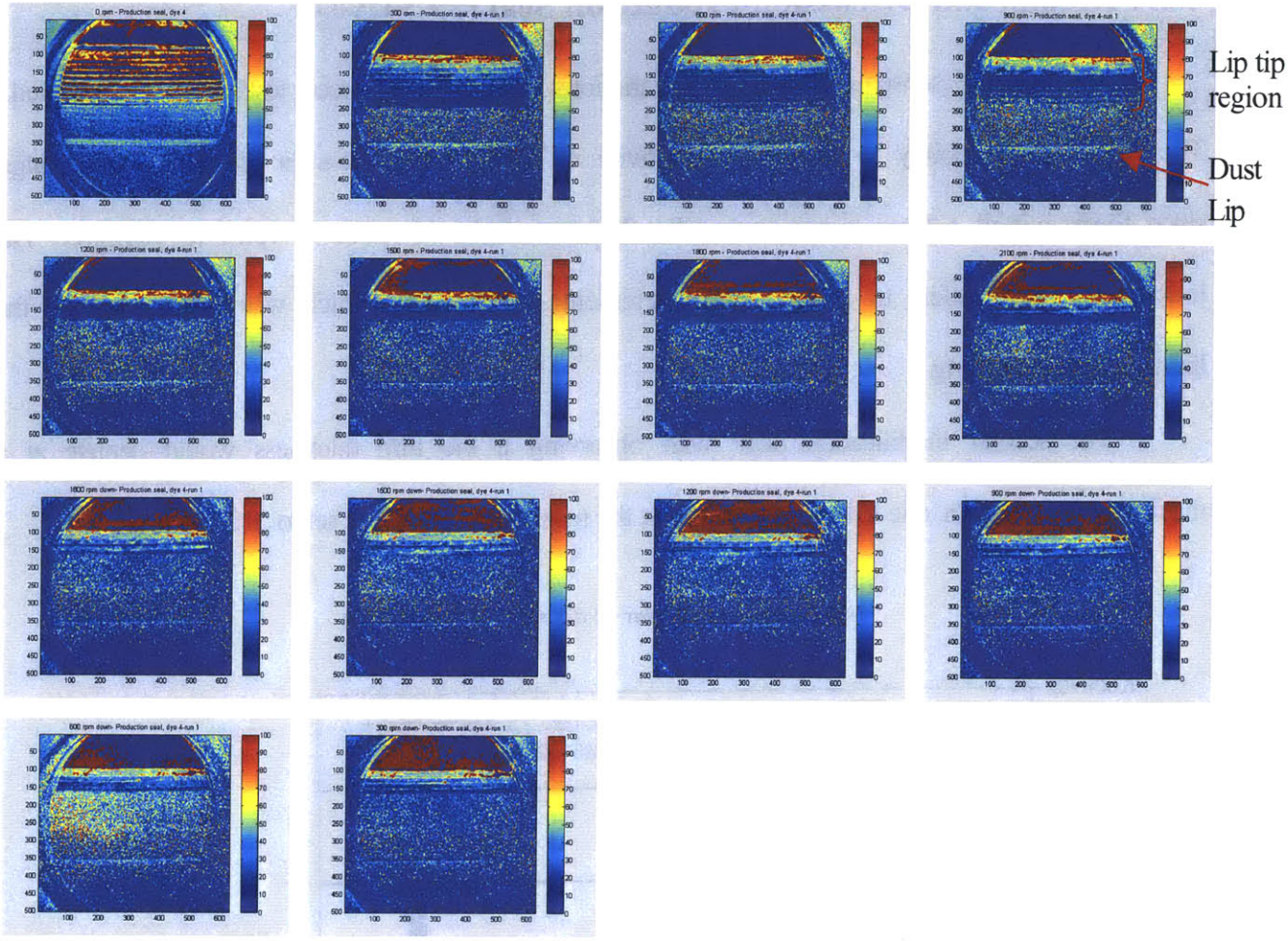

Figure 4.18a: Progression of film thickness with shaft speed images for the production seal-dye 4-run 1, first image starting in the static condition.

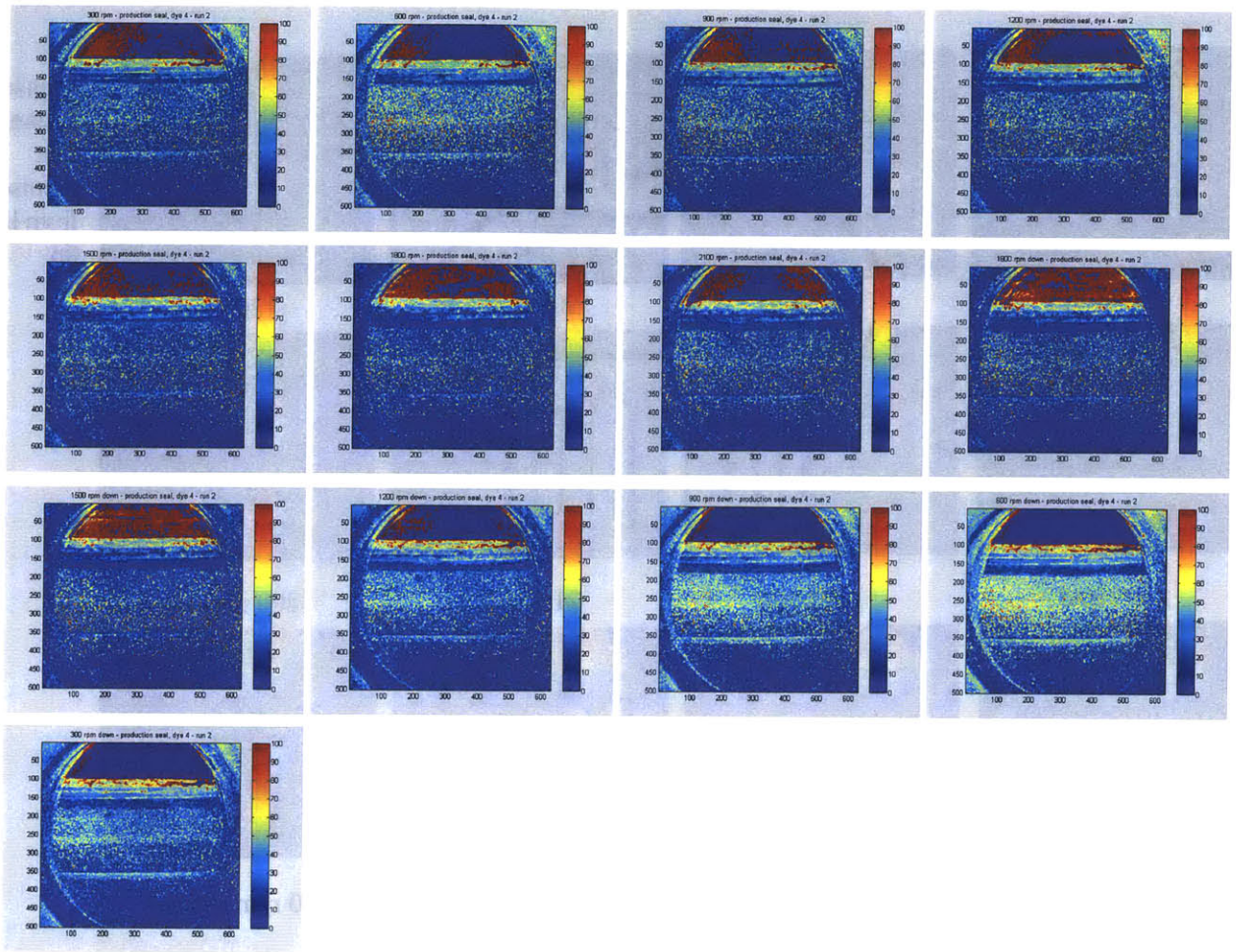

Figure 4.18b: Progression of film thickness with shaft speed images for the production seal-dye 4-run 2, first image starting at 300 rpm.

In figures 4.18 a and b, the lip tip region and the dust lip were clearly distinguishable. The first run shows a clear "ingestion" of the meniscus until approximately 1200-1500 rpm where the meniscus is stationary, even through the second run.

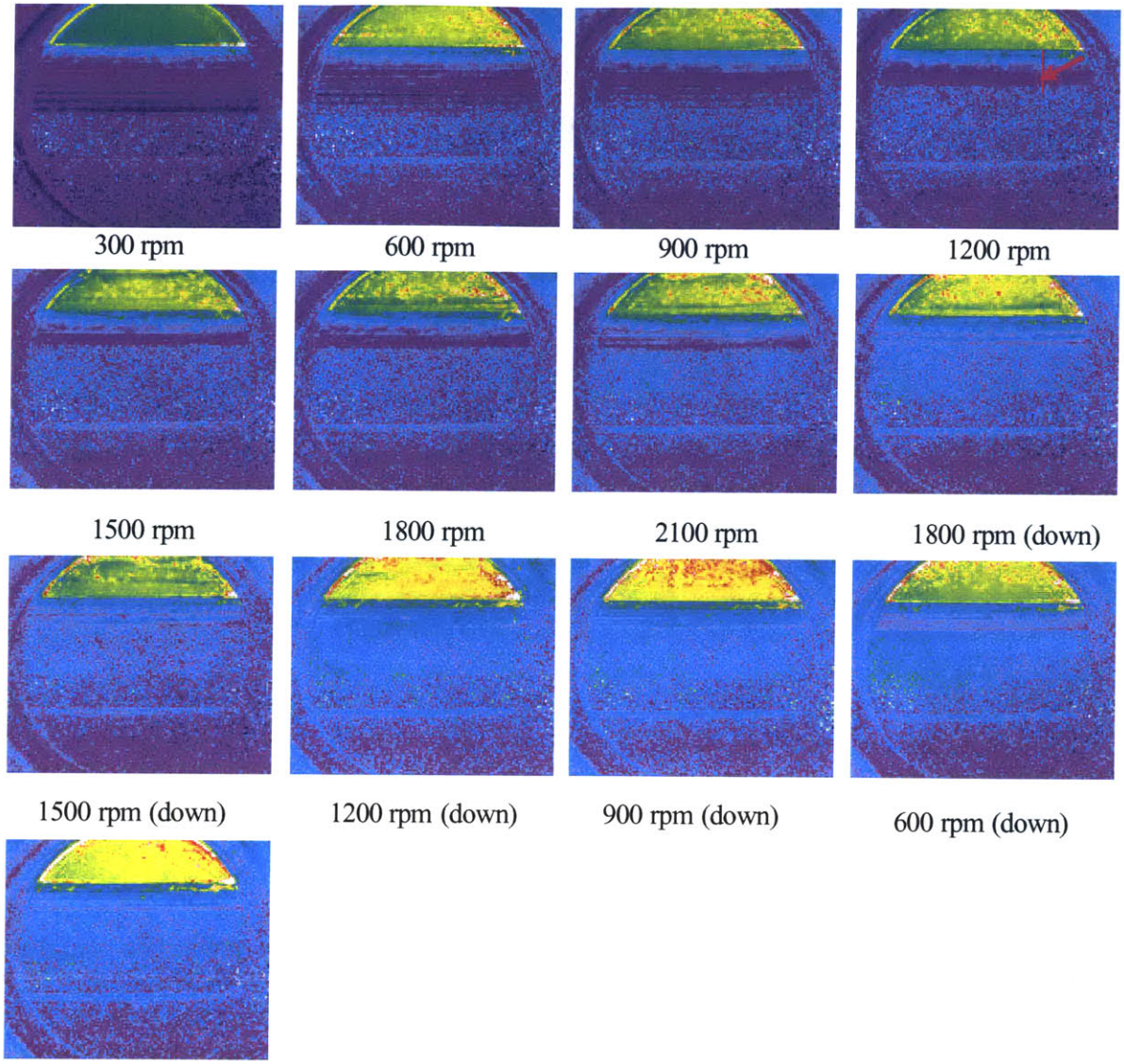

Figure 4.19: Change in meniscus location with shaft speed. Notice the meniscus initially was located closer to the air side of the seal until approximately 900-1200 rpm where the location shifts closer to the oil side, and remains for the remainder of the test. Actual measured distances provided in table 4.3 and figure 4.20.

Table 4.3: Meniscus location from the lip tip of the seal

Run 1			Run 2		
Speed (rpm)	Distance (pixels)	Distance (mm)	Speed (rpm)	Distance (pixels)	Distance (mm)
300	145.086	5.743301853	300	63.07	2.496657485
600	155.029	6.13690048	600	67.0671	2.654884687
900	135	5.3440425	900	61.0737	2.417632951
1200	81.0555	3.208622495	1200	63.1981	2.501728388
1500	77.0584	3.050395293	1500	75.06	2.97128763
1800	81.0555	3.208622495	1800	65.192	2.580657916
2100	77.1622	3.054504268	2100	79	3.1272545
1800	65.0692	2.575796817	1800	75.06	2.97128763
1500	59	2.3355445	1500	79.3095	3.139506212
1200	59.0762	2.338560915	1200	79	3.1272545
900	65.0692	2.575796817	900	81.0555	3.208622495
600	63.0714	2.496712905	600	81.0555	3.208622495
300	57.2189	2.265038766	300	77	3.0480835

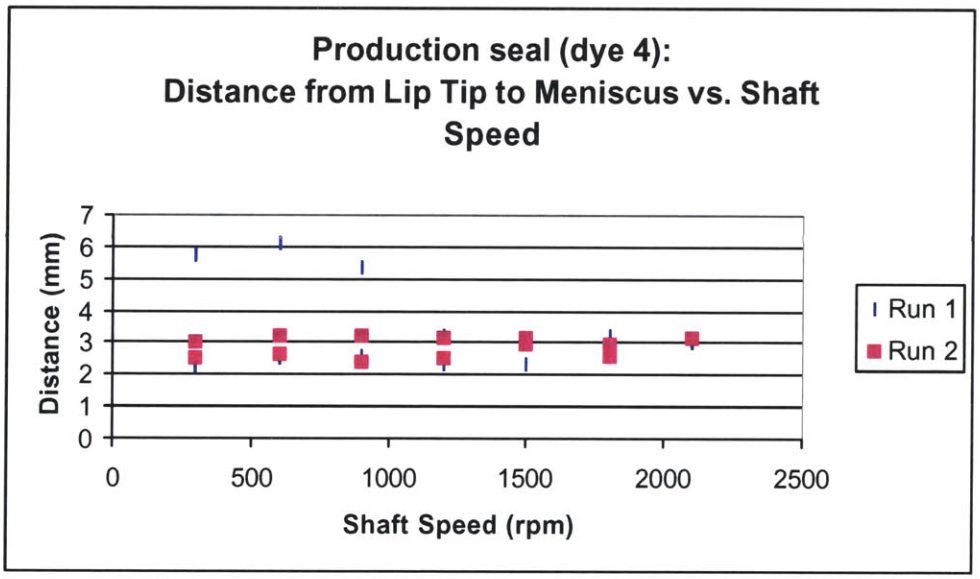

Figure 4.20: Change in distance from lip tip to meniscus with speed.

Observe how the meniscus distance is further from the lip tip until about 900 rpm, where it then stabilizes closer to the lip tip. This could be a signifier of starved lubrication.

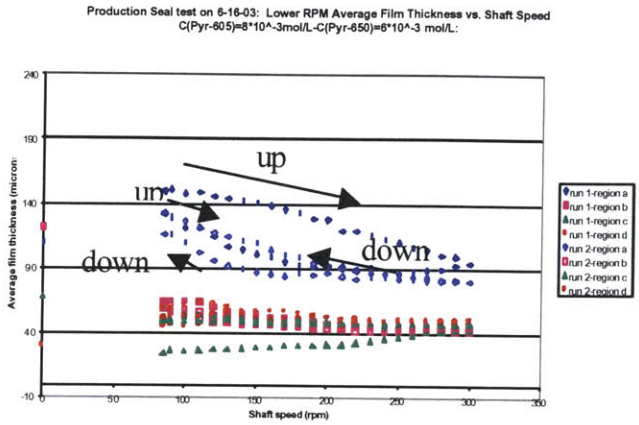

(i)

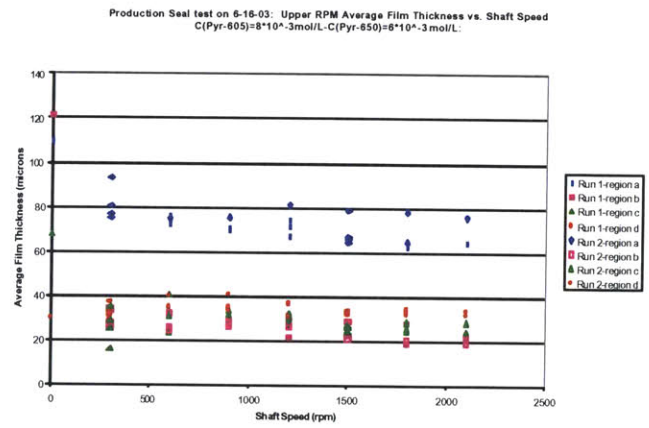

(ii)

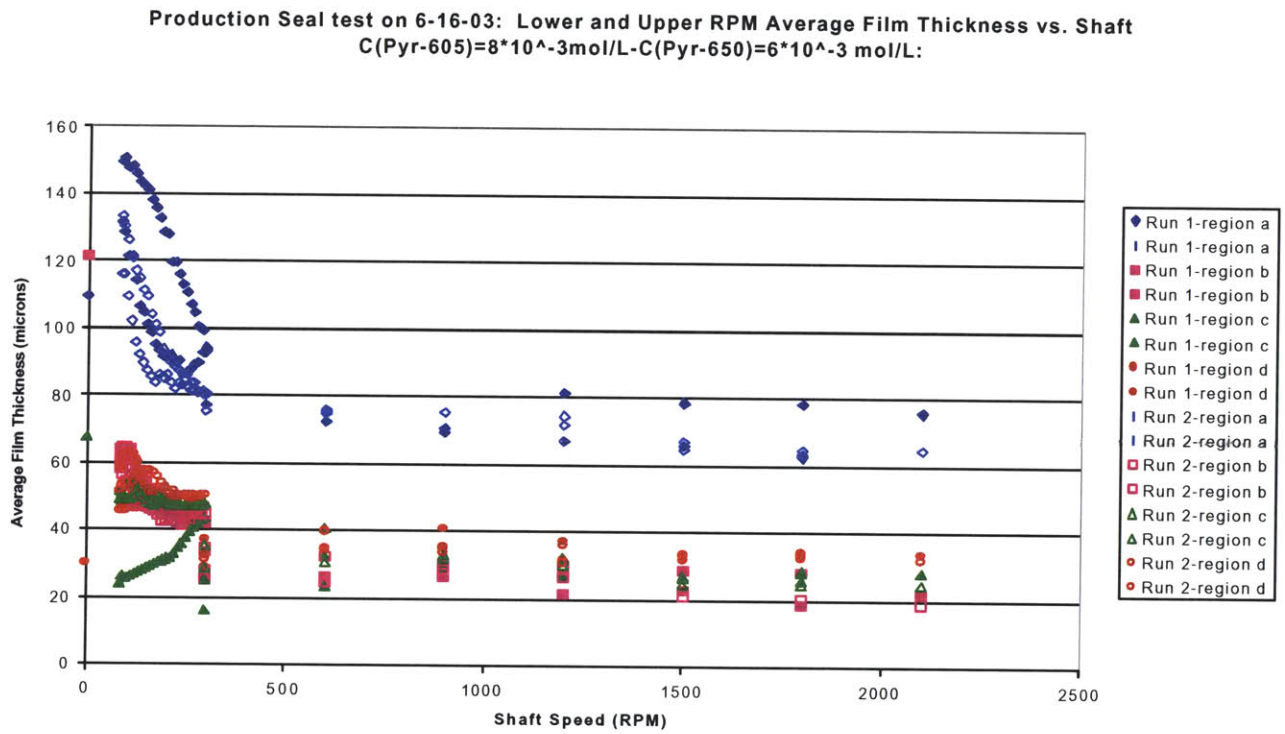

(iii)

Figure 4.21: Production seal-dye 4 average film thickness progressions for (i) lower rpm range, (ii) upper rpm range, and (iii) entire range. (i) showed the largest change over the range of speeds.

Region a, for the lower rpm range, was initially higher due to the thicker oil in the static condition. The film thickness followed the same path when the speed was decreased in the first run. The thickness became relatively constant from approximately 200-300 rpm.

The upper range film thickness values stayed relatively constant beyond 300 rpm. There was the largest change within the lower rpm range.

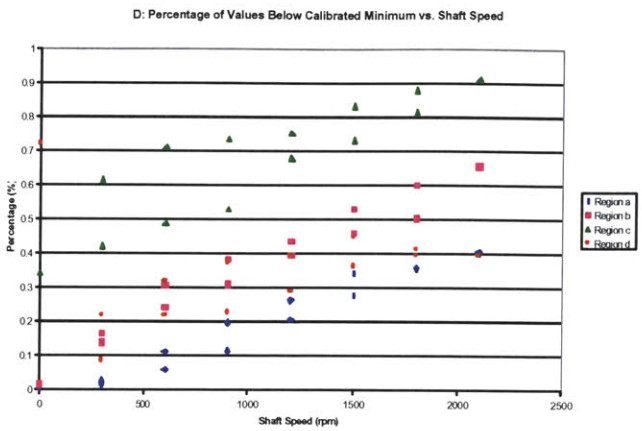

(D)

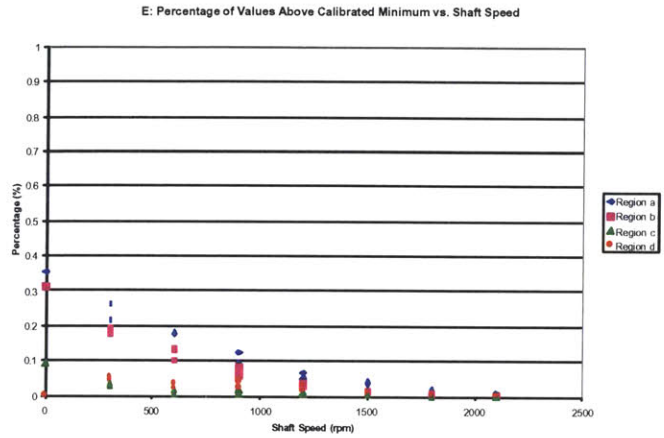

(E)

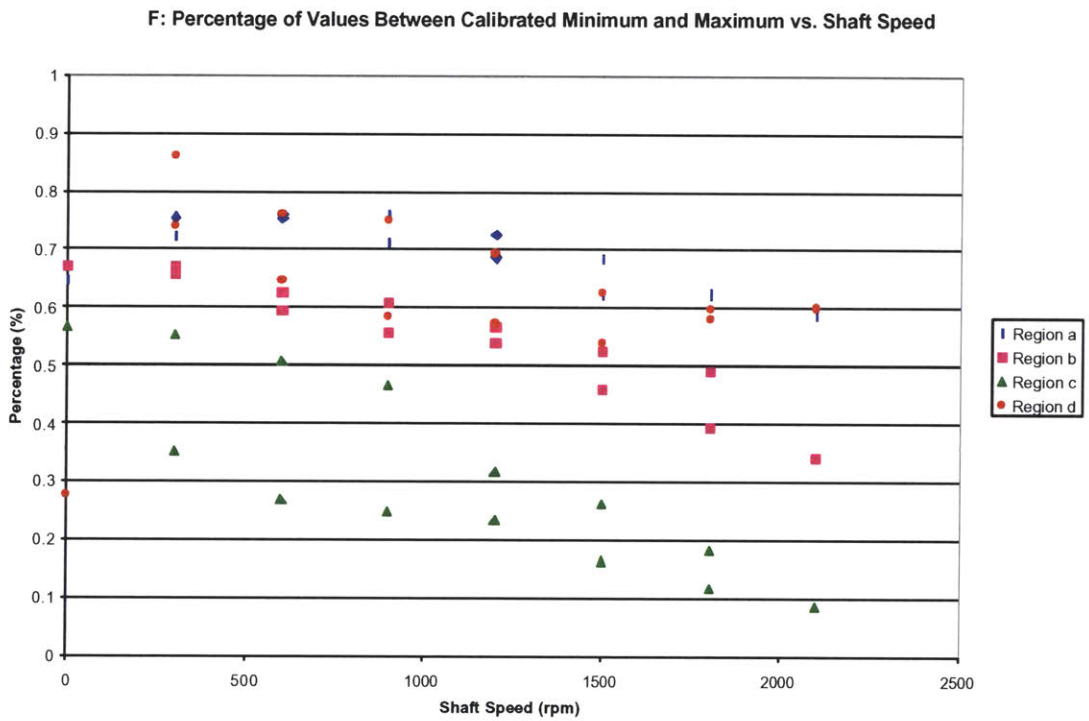

(F)

Figure 4.22: Production seal-dye 4, percentage of thickness values that are (D) below, (E) above, and (F) within the calibrated range. The change in the dye concentrations increased the percentage of values below the minimum, which was acceptable since the only means to calibrate the thinner films would be to create a completely new method for calibrating.

Since the dye concentration was changed to capture the thicker films, the percentage of values less than the minimum increased. The calibration range still provided reliable values (F percentage for region a and b are 50% or more).

4.2.5 Results and Discussion-15 Degree Seal-Dye 4

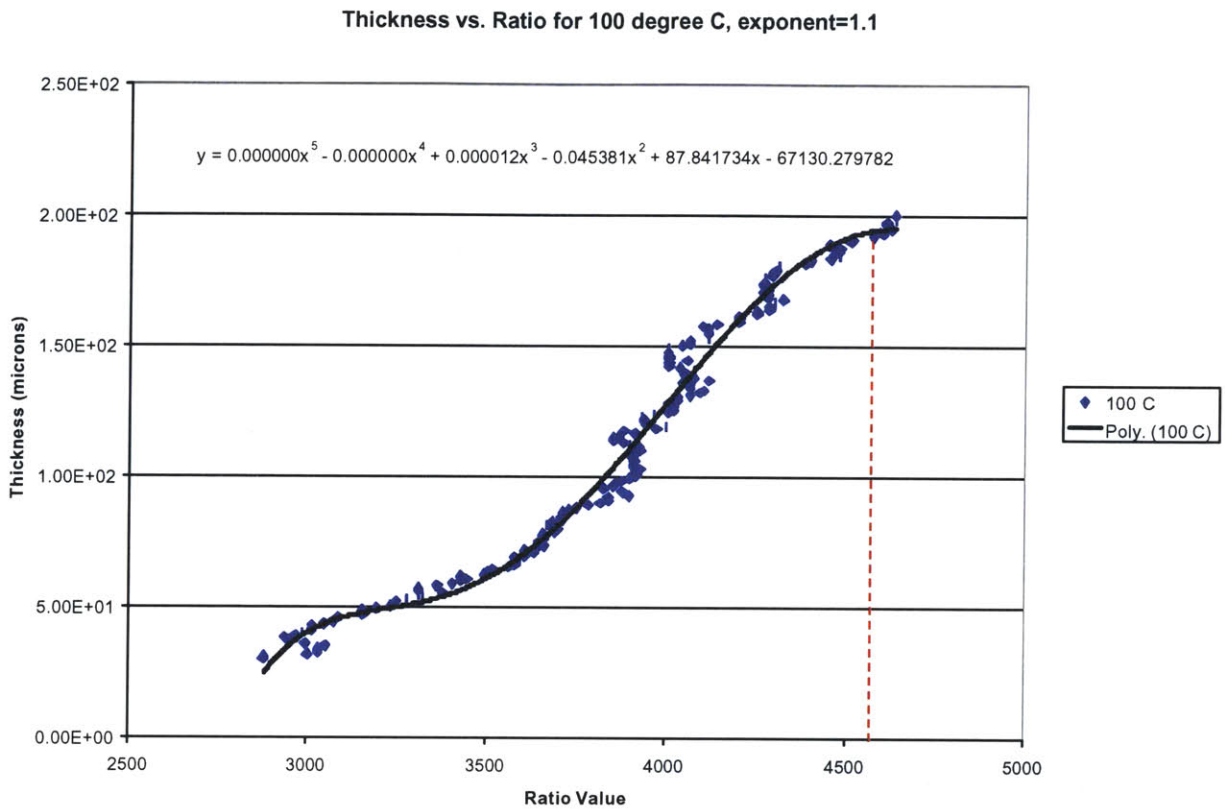

Figure 4.23: Calibration curve for 15 degree seal-dye 4, maximum at the red dotted line. The calibrated range was 2878-4636 (24.87-195.15 microns).

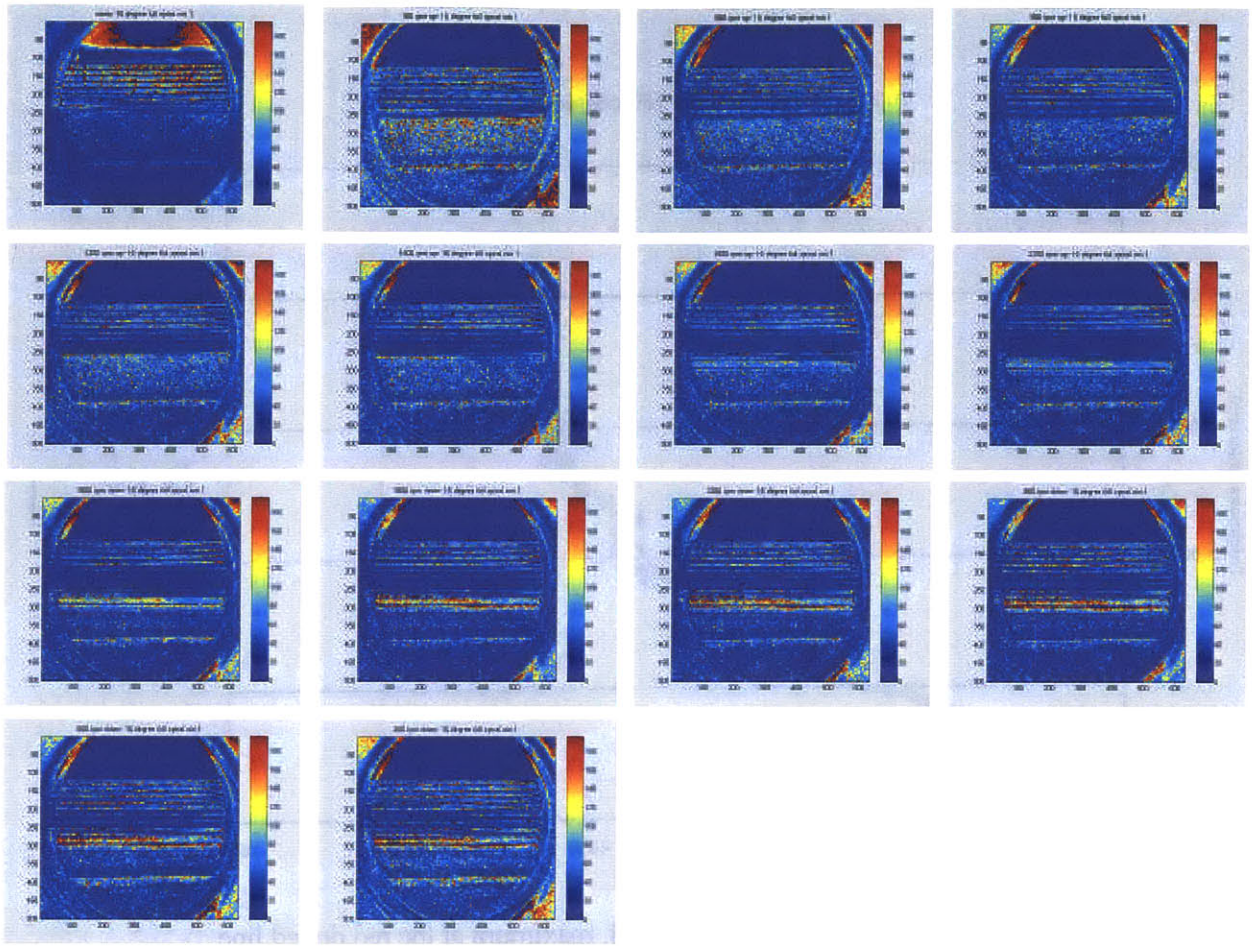

Figure 4.24a: Progression of film thickness with shaft speed for the 15 degree seal-dye 4-run 1, first image in the static condition.

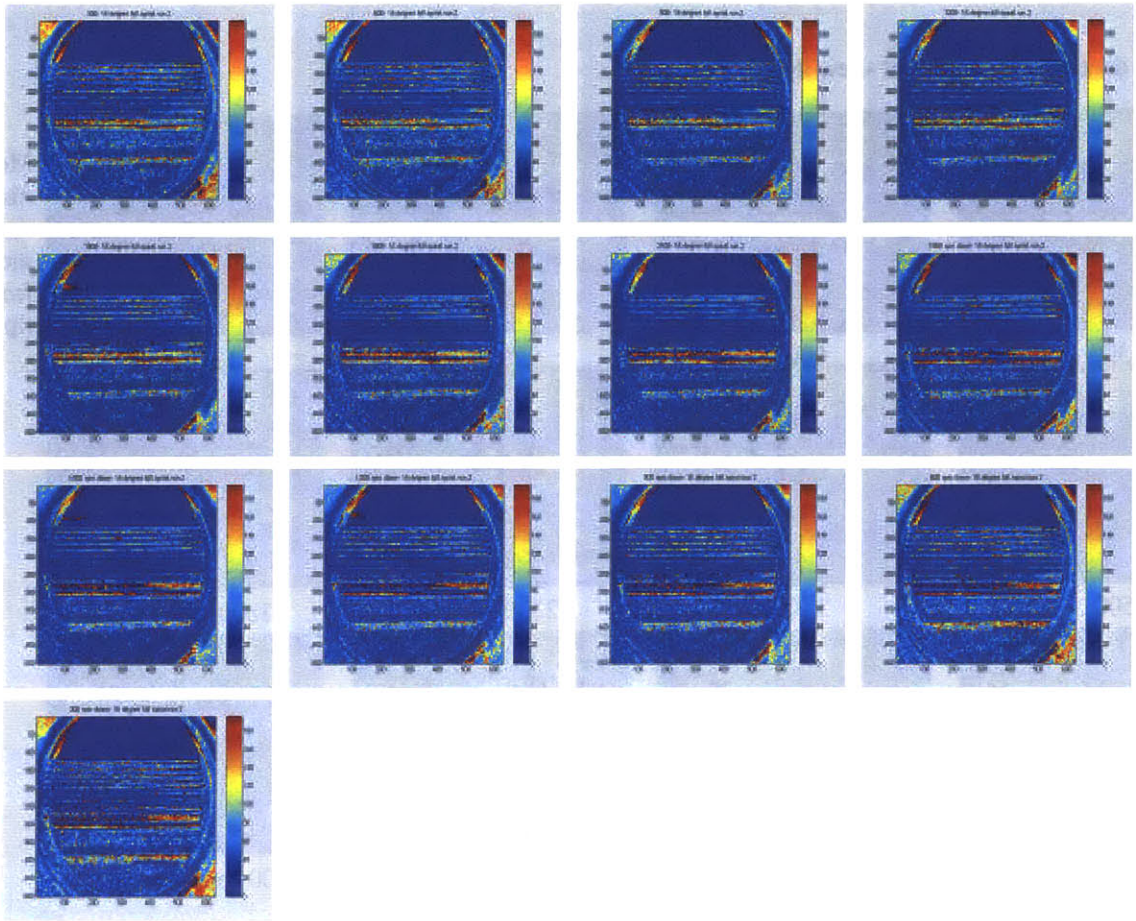

Figure 4.24b: Progression of film thickness with shaft speed for the 15 degree seal-dye 4-run 2, first image in the static condition.

15 degree, full spiral seal -new dye

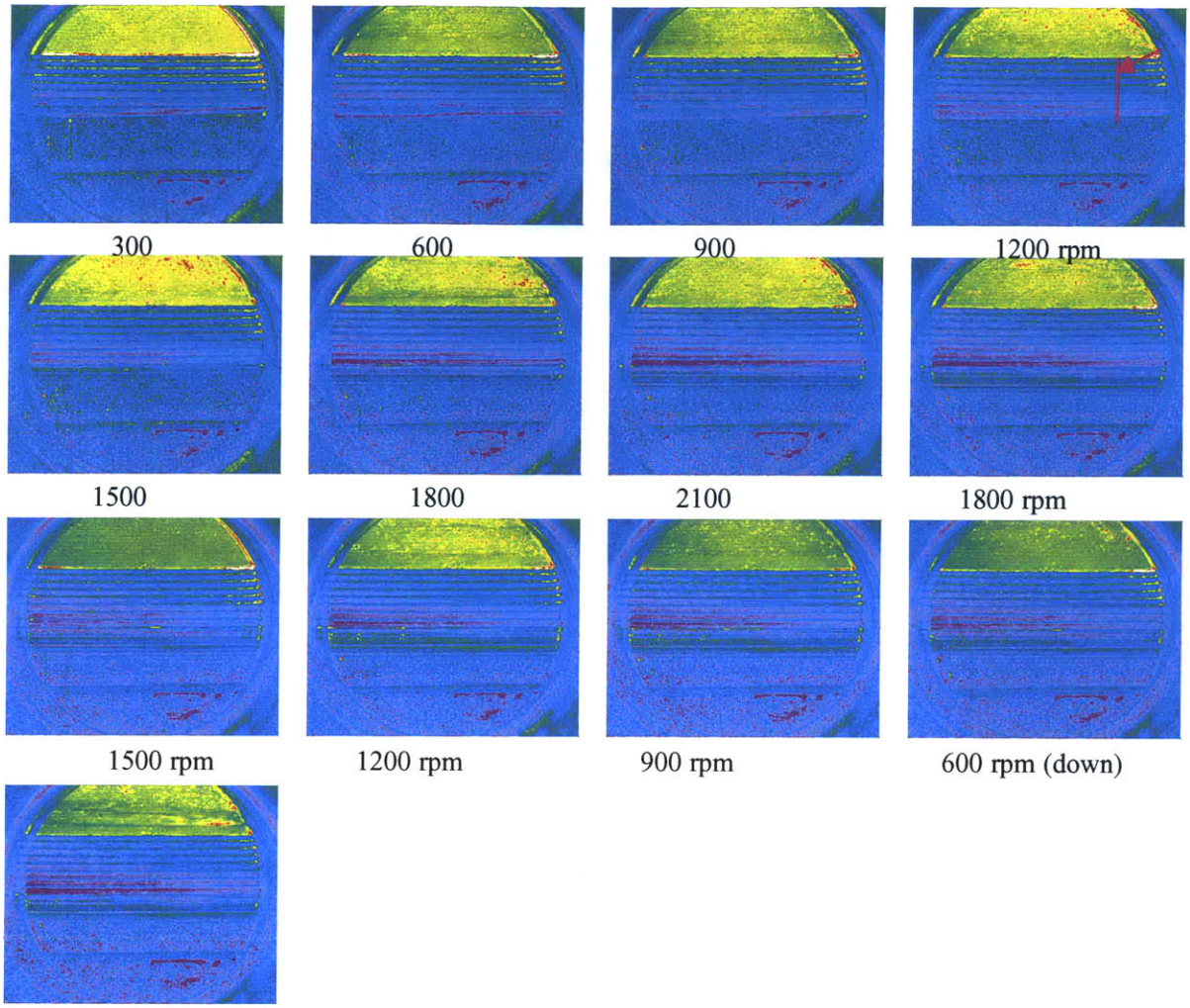

Measured distance that meniscus is from lip tip.

Figure 4.25: Change in meniscus location with shaft speed. The meniscus location remained relatively constant over the observed speeds. This would imply possible better lubrication since the meniscus is visible which means no leakage and not as close to the lip tip as with some of the previous seals. Specific measurements are given in table 4.4 and the progression comparison is shown in figure 4.26.

Table 4.4: Change in distance from lip tip to meniscus with speed.

Run 1			Run 2		
Speed (rpm)	Distance (pix)	Distance (mm)	Speed (rpm)	Distance (pix)	Distance (mm)
300	140.014	5.508724817	300	189	7.4360349
600	140.014	5.508724817	600	189.024	7.436979158
900	140.014	5.508724817	900	187	7.3573467
1200	140.014	5.508724817	1200	189.011	7.436467685
1500	140.014	5.508724817	1500	187.024	7.358290958
1800	178	7.0032498	1800	187	7.3573467
2100	178	7.0032498	2100	187	7.3573467
1800	189.024	7.436979158	1800	187	7.3573467
1500	189.024	7.436979158	1500	187	7.3573467
1200	189.024	7.436979158	1200	187	7.3573467
900	189.024	7.436979158	900	187	7.3573467
600	189.024	7.436979158	600	187	7.3573467
300	189.024	7.436979158	300	187	7.3573467

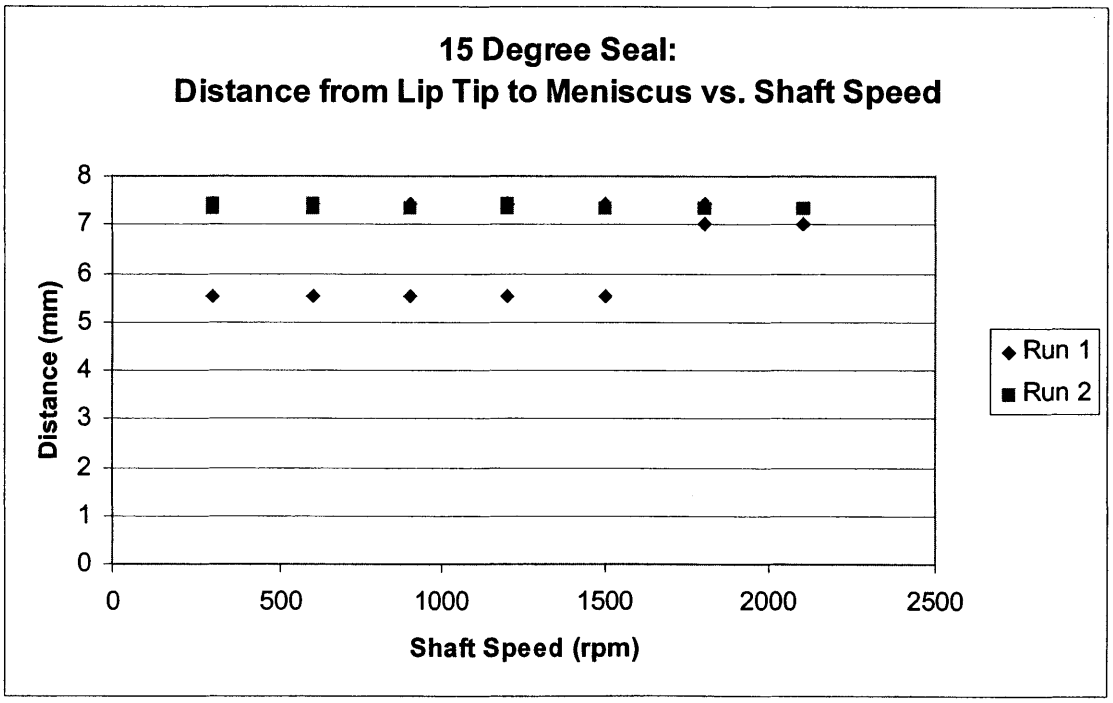

Figure 4.26: Change in meniscus distance from lip tip with speed.

The meniscus moves out toward the dust lip, and then proceeds to remain stationary at around 1500-1800 rpm. Notice that though the meniscus becomes stationary, it stabilizes at a further distance from the lip tip compared to the previous production seal.

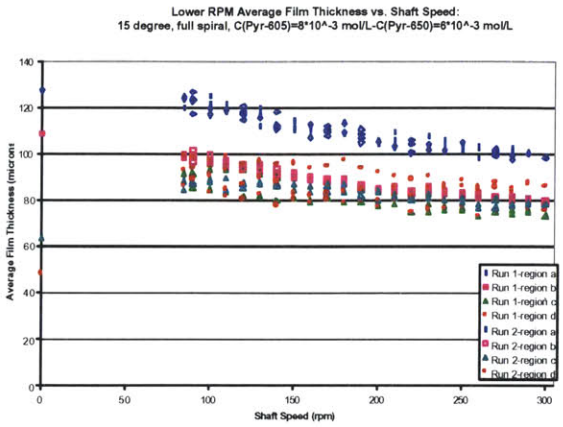

(i)

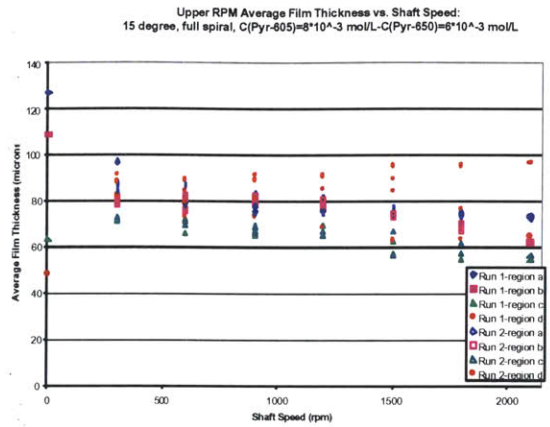

(ii)

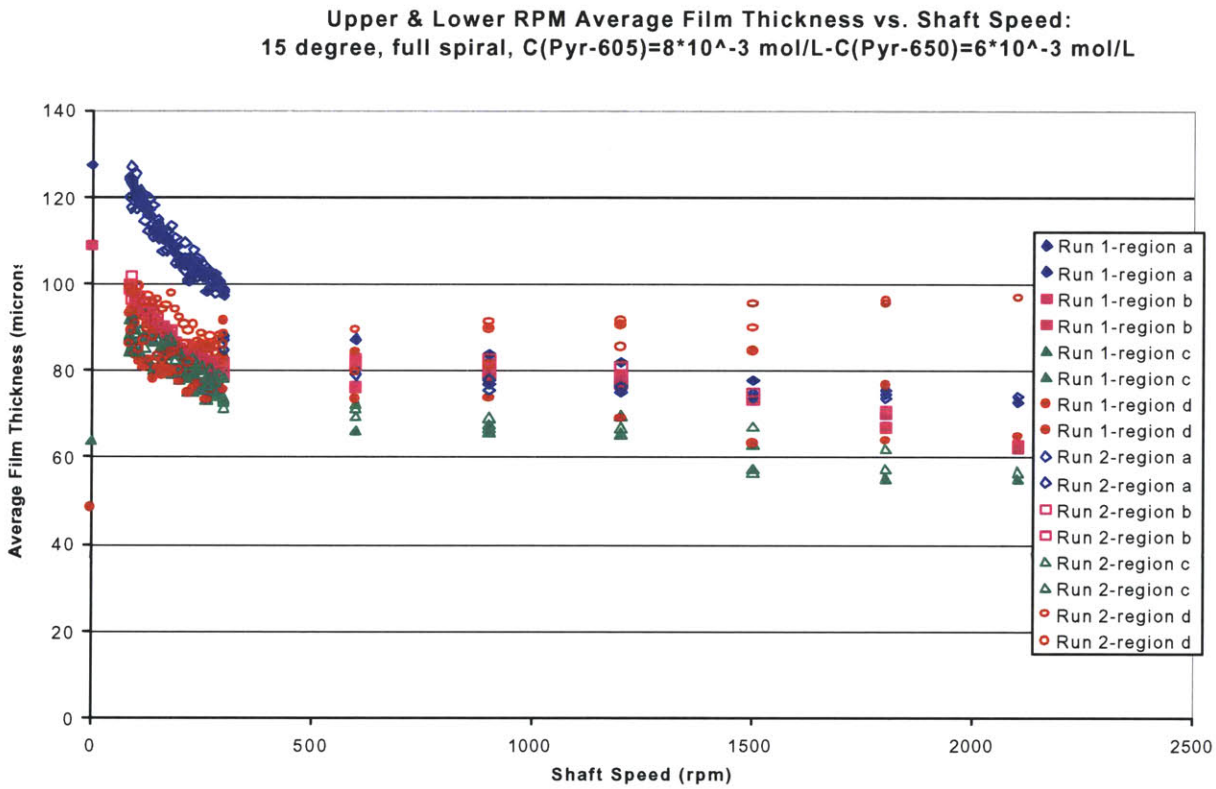

(iii)

Figure 4.27: 15 degree-dye 4 average film thickness progressions for (i) lower rpm range, (ii) upper rpm range, and (iii) entire range. The data over the entire range showed great results, the average film thickness values decreased with shaft speed as predicted, and the difference between ramping up and down decreased.

The 15 degree seal produced great results. Both the upper and lower rpm ranges had a consistent trend, both following a repeatable path for speed increase and decrease.

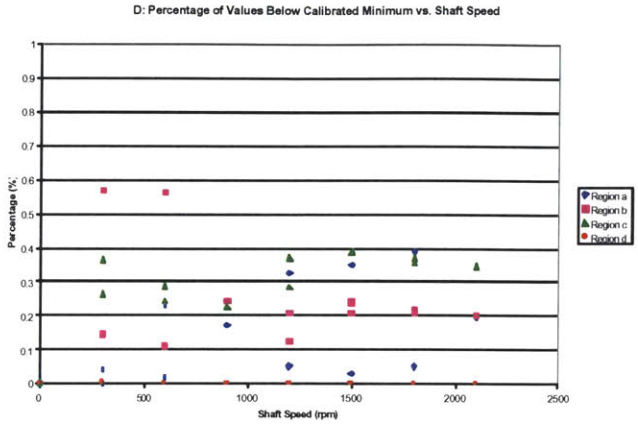

(D)

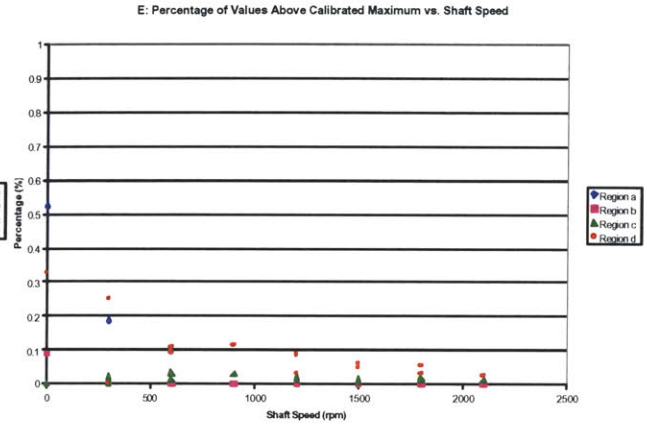

(E)

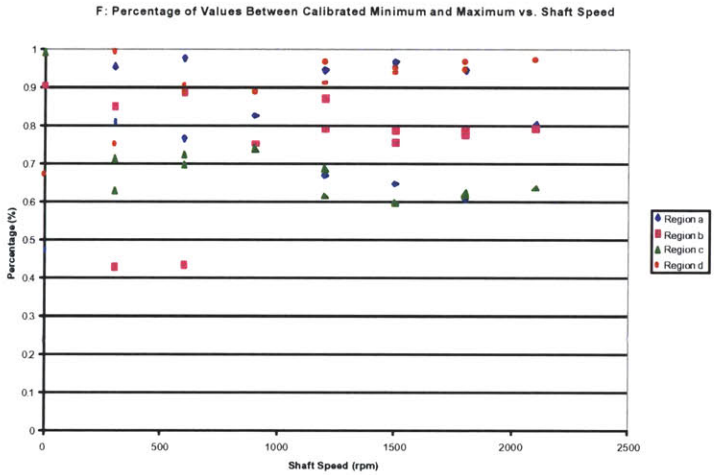

(F)

Figure 4.28: 15 degree-dye 4-percentage of thickness values that are (D) below, (E) above, and (F) within the calibrated range. This seal had more values within the range with still some values below the minimum.

4.2.6 Results and Discussion-Production Seal with Holes-Dye 4

As mentioned in the introduction, the ideal situation includes a thick lubrication layer, while simultaneously preventing leakage. Holes were drilled into the region closest to the lip tip to observe how the film thickness was affected.

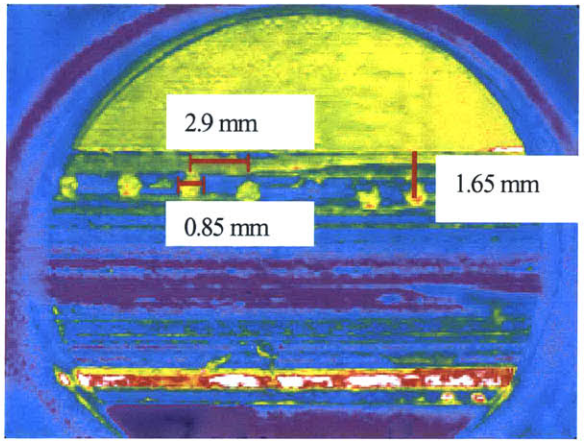

Figure 4.29: Schematic of where through holes were drilled into the seal.

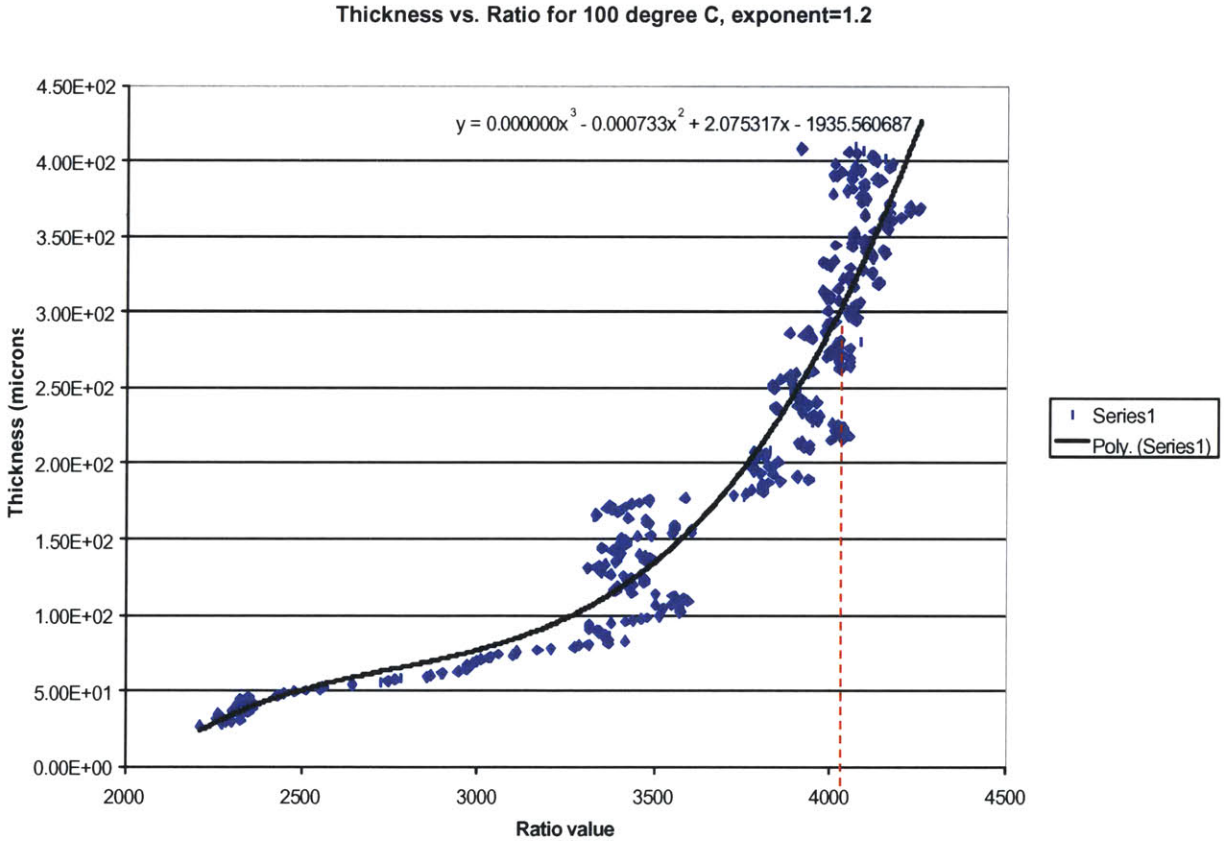

Figure 4.30: Calibration range 2212-4050 (23.48-313.04 microns), maximum at red dotted line.

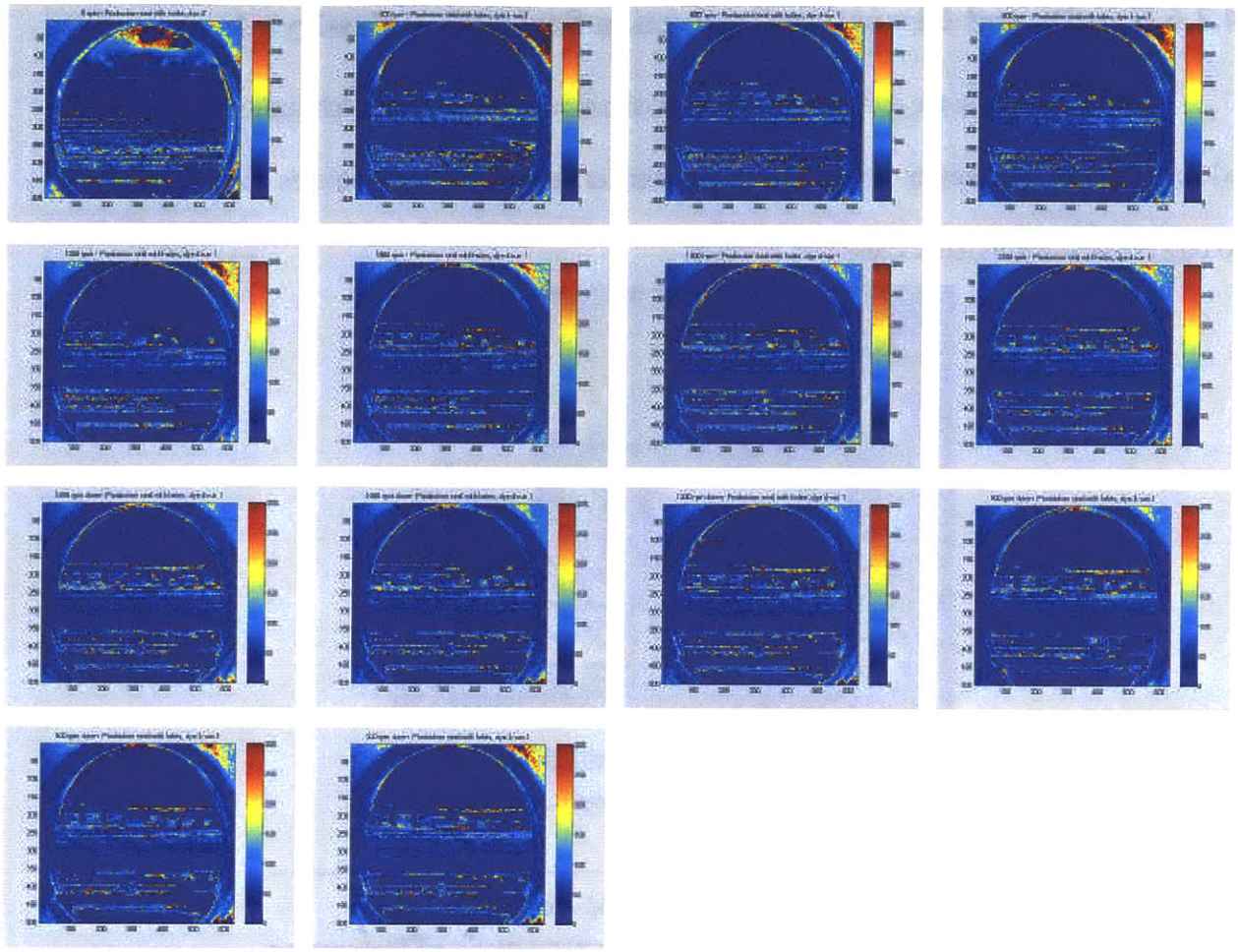

Figure 4.31a: Progression of film thickness with shaft speed for production seal with holes-dye 4, run 1, progression of film thickness with shaft speed.

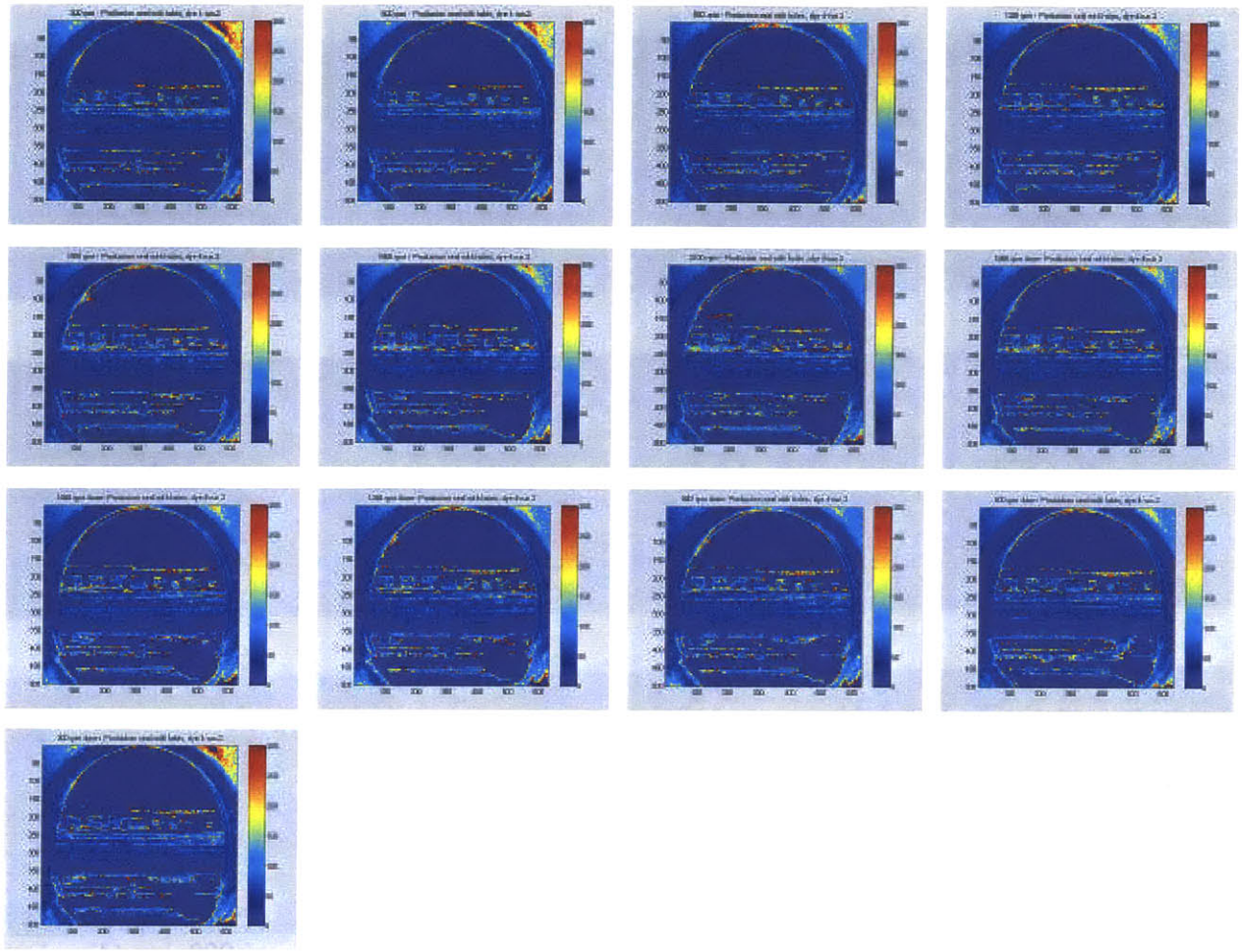

Figure 4.31b: Progression of film thickness with shaft speed for production seal with holes-dye 4, run 2, progression of film thickness with shaft speed.

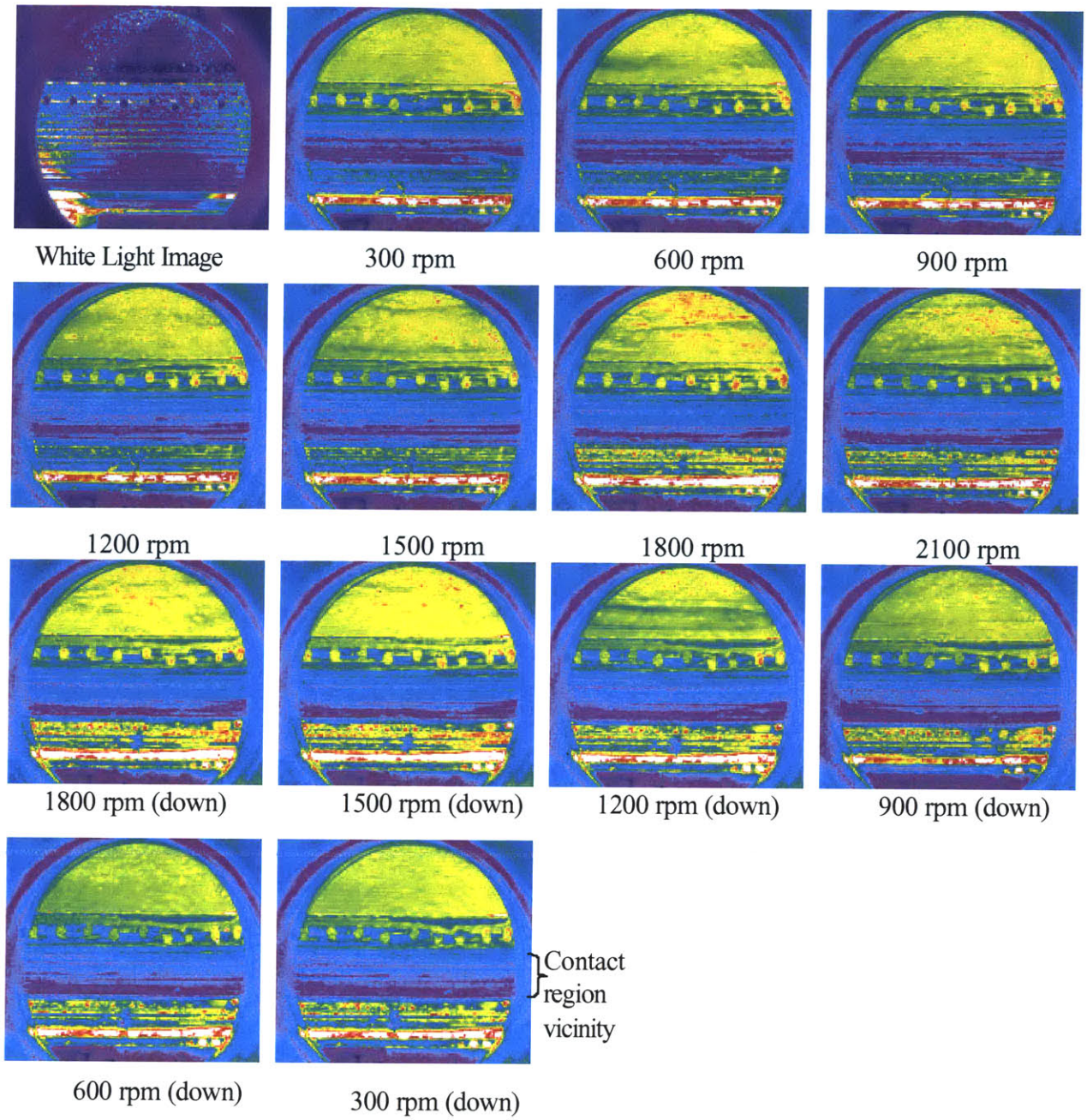

Figure 4.32: Progression of ratio images of seal over the velocity range. This seal did not show a prominence when attempting to locate the meniscus locations.

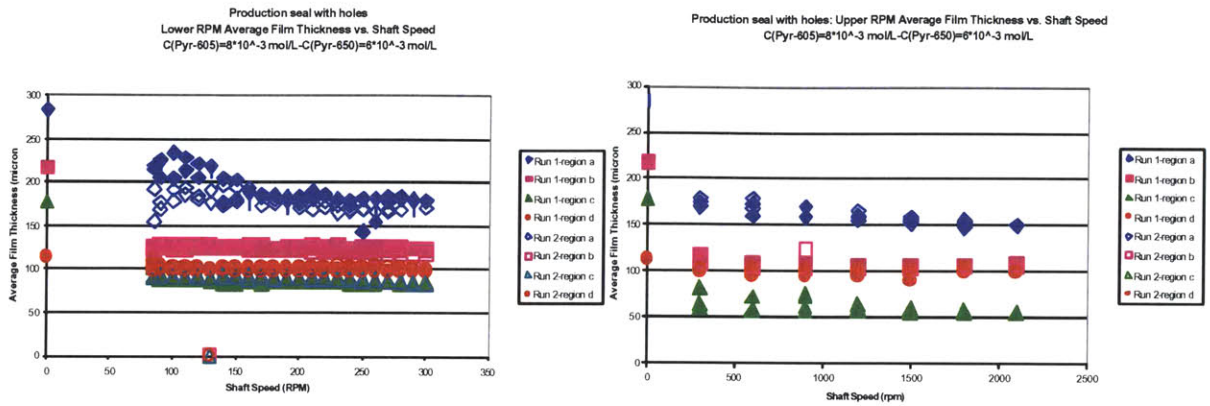

(i) (ii)

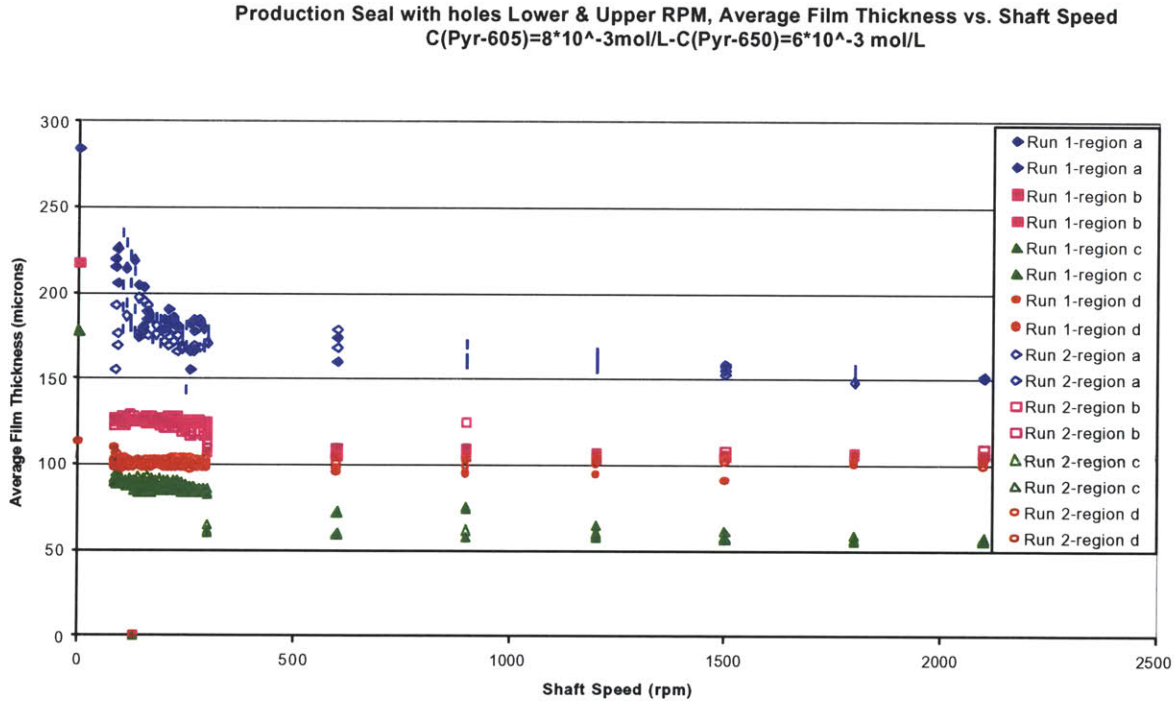

(iii)

Figure 4.33: Production seal with holes-dye 4, average film thickness as a function of speed for (i) lower rpm range, (ii) upper rpm range, and (iii) entire range. Again, great results for this particular seal. Notice the nearly doubling in average film thickness values compared to the standard production seal.

The addition of the holes nearly doubled the film thickness, yet still provided enough reverse pumping to prevent leakage. There was an initial small amount of leaked oil, possibly due to an excess of pressure within the oil sump.

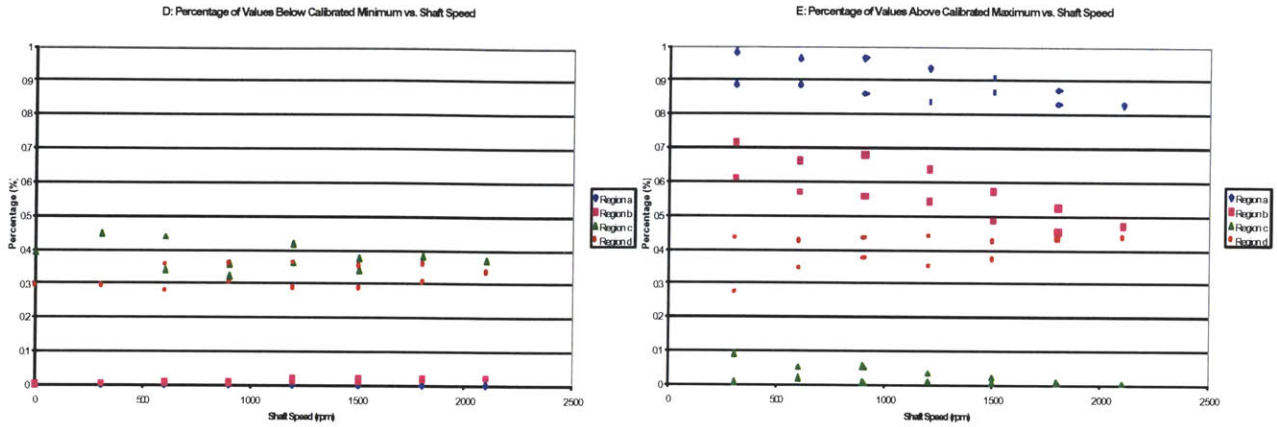

(D) (E)

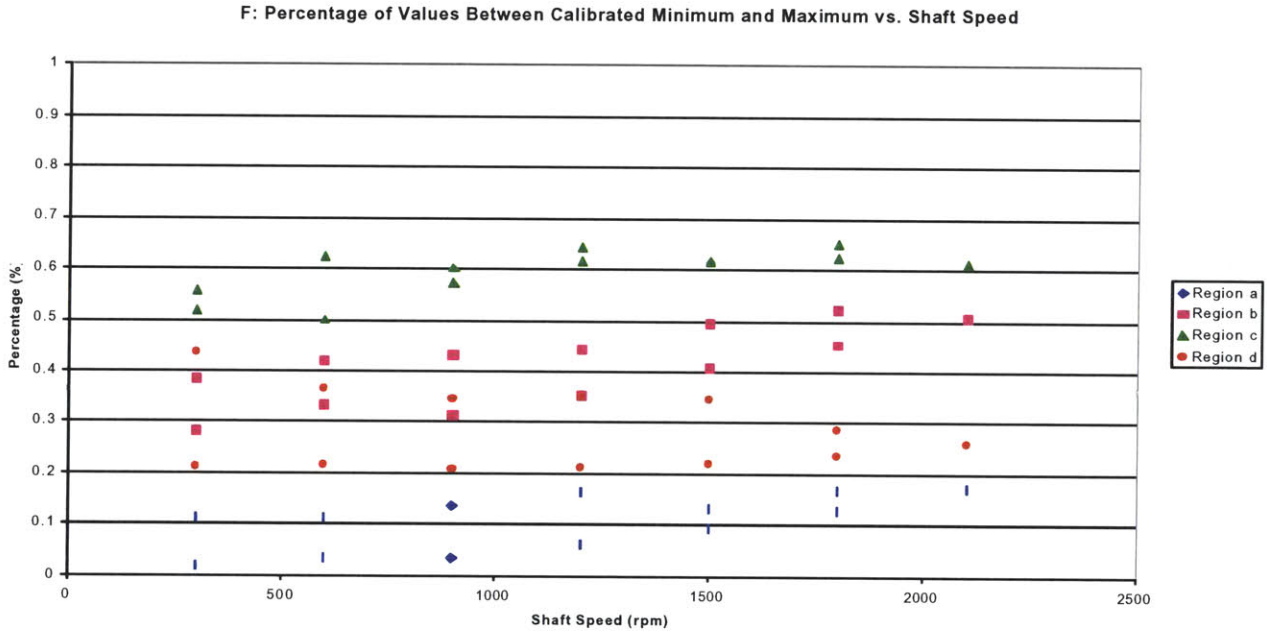

(F)

Figure 4.34: Production seal with holes-dye 4 percentage of thickness values that are (D) below, (E) above, and (F) within the calibrated range. Here, more values were above the maximum because the holes allowed for an increase in film thickness.

Due to the increase in film thickness with the presence of the holes, there were a considerable percentage of values that were above the calibrated range.

5.1 Summary

Based on the results and analysis, the region of the seal closest to the lip tip (region a), provided the most insight to the changes in film thickness, and thus insight into reverse pumping as the rotational velocity was changed.

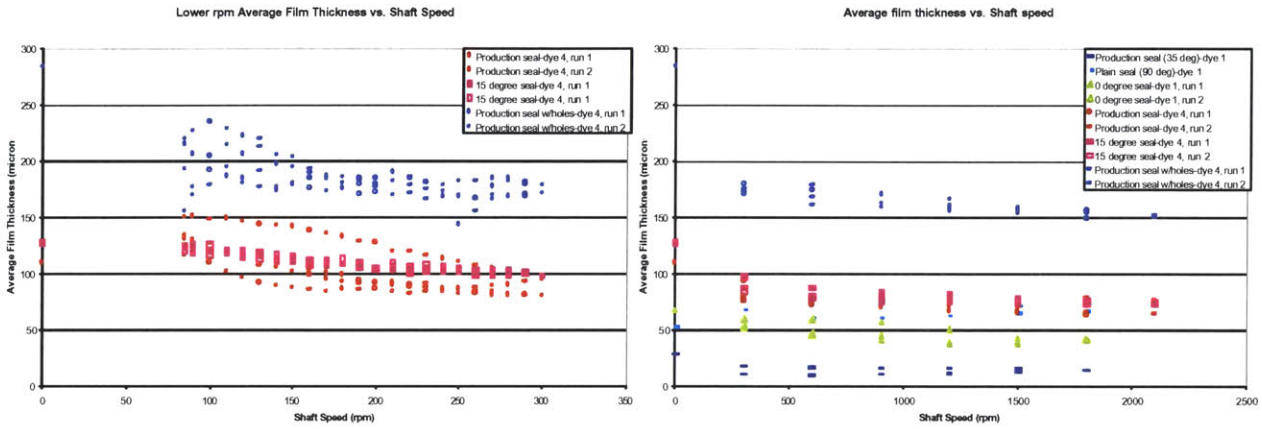

Figure 5.1: A comparison of average film thickness values in region a for the different seals tested. Clearly, the production seal with the holes provided the most amount of a lubricating film (nearly double that of the production seal).

Figure 5.1 summarizes the average film thickness values for each of the tested seals. The seals tested with dye 1 may not be as comparable to the ones with dye 4 since the cutoff values were an order of magnitude different.

Dye 1

The plain seal had the higher film thickness values presumably because there were no grooves, however, there was no oil that leaked out of the seal, which would mean there must be reverse pumping that occurs but on the microscopic level. The 0 degree seal had thickness levels between the 90 degree (plain seal) and 35 degree (production seal).

Dye 4

Again, the production seal had the smallest of the film thickness values, while the production seal with holes that were added near the lip tip, had the largest values.

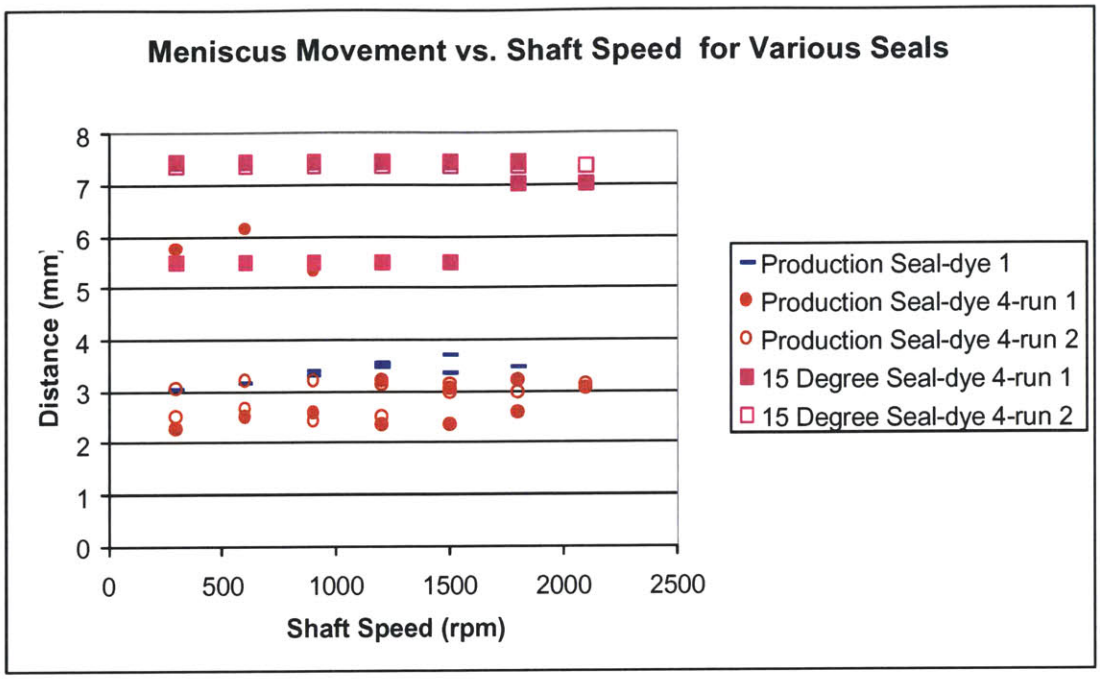

Figure 5.2: Comparison of the distance the meniscus lies from the lip tip for the seals tested (including only the seals where the meniscus was observable).

The 15 degree seal had the largest distance from the lip tip without leakage. Also, out of the 0°, 35°, 90°, this seal had the thickest average film thickness (from figure 5.1). The film thickness coupled with the meniscus location, signifies a good lubricating situation because the oil was not only thicker than the other seals, but also provided lubrication farther from the lip tip. The reason for the missing data in figure 5.2 for the other seals was because the meniscus location was not distinguishable.

5.2 Conclusions

The ideal lubricating situation would be as thick of a film layer between the shaft and seal for proper lubrication, heat dissipation and ultimately, a more successful operating seal without catastrophic failure (i.e. leakage). When observing the changes in film thickness values over the shaft speed ranges of 300-2100 rpm, there was not as significant of a change when compared to the lower rpm range (85-300 rpm). For instance, the range in film thickness in the lower rpm span for the production seal was 90-150 microns (region a) compared to 64-77 microns over the upper rpm span. When investigating further into the lower rpm range, the film thickness would change the most drastically between 85-200 rpm. Thus, during the initial speed increase of a seal, there is a decrease of oil film. However, the lubricating film is not recoverable, as was seen with the repeated runs (i.e., the film thickness while ramping down the shaft speed was not as high as when the speed was ramping up). This is also due to the fact that in the static condition, there is the maximum lubricating film. Thus, the largest effect of reverse pumping occurs between 0 and 200 rpm.

The fact that the trend of film thickness followed the same path whether the speed was being ramped up or down (excluding the initial ramping up from 0 rpm), proves that the effect of reverse pumping counterbalances the effects of pressure differences that would force the seal to leak. Even in the extreme case where the film thickness was doubled (production seal with holes), the film thickness followed the same repeatable trend, again proving the reverse pumping effects.

The seals that produced the most successful lubrication were the 15 degree seal and the production seal with holes, both with the use of dye 4. The repeatability of the results for each,

exemplified that the forces that would drive oil to leak out, is almost equal to the reverse pumping (i.e., the film thickness had approximately the same values whether the speed was being ramped up or down).

5.3 Future Work

A better method for calibrating the film thickness values would allow for more reliable results for both the thin films (<<1 micron) and the thick film (>150 microns). The interference fringes that are observed when clamping the two plates together prove the inconsistencies that the calibration induces when looking at thin film regions. Aspects such as surface roughness and the fringes cannot be neglected for these values because they are the same order of magnitude. Utilization of an interferometric microscope was explored, but the capabilities were not available at the time to accommodate the present calibration fixture.

There still remain other variations of the Caterpillar production seal such as reversal of groove spirals around the contact region, and addition of a relief cut between the lip tip and the roll up of the seal. Also, further exploration into the production seal with holes would provide interesting observations. Hole placement with respect to the lip tip, frequency, size, and most importantly, elapsed time to failure compared to the production seal without holes are worth exploring.

Appendix A

Estimation for $\frac{\partial p}{\partial x}$:

From

$$P_{\text{lip tip}} = P_{\text{oil}} = \frac{k_{teflon} z}{A} \approx \frac{k_{teflon} h}{2\pi R \Delta x} \tag{2.8}$$

$$k_{teflon} = \frac{IE}{R^3}$$

$$E = 0.46 \times 10^9 \frac{N}{m^2}$$

$$R = 0.0334m$$

$$I = 2\pi R^3 (\text{thickness})$$

thickness =0 .001066m

Though it may be a close approximation by using the spring force, we are introducing some error. Since the pressure differential in the x direction is not necessarily constant, we are defining the area as the circumferential length over a distance of Δx, when in reality, the surface area may be smaller, therefore increasing the value of P_{oil}.

There may also be contributions to the pressure differential due to surface tension.

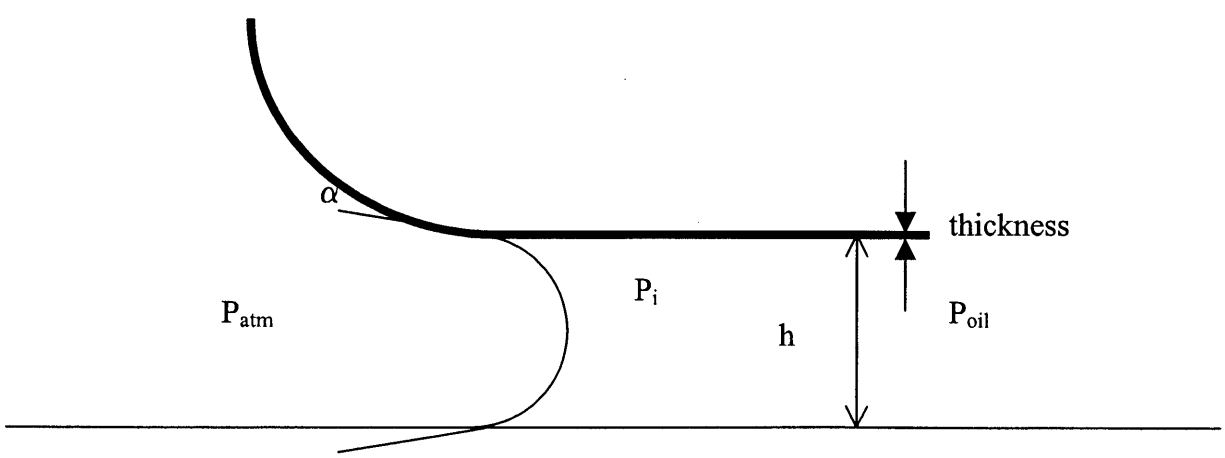

$$(\frac{\partial p}{\partial x})_{SurfaceTension} = \gamma(\frac{2\cos\alpha}{h})$$

$$\gamma = 0.0315\frac{N}{m};\ \alpha = 30^0\ [14]$$

Comparing the orders of magnitude of the two pressures:

$$P_{oil} \approx (3.16778\text{E}+11)\text{h} >> P_{SurfaceTension} \approx 0.009717841\text{h}$$

Therefore, the effects of surface tension can be neglected from the pressure estimation.

Appendix B

$$-\frac{h^3}{12\mu}\frac{\partial P}{\partial x}+\frac{R\omega h}{2}=0$$

$$\frac{\partial P}{\partial x}=\frac{\frac{k_{teflon}h}{2\pi R\Delta x}-P_{atm}}{\Delta x}$$

$$\mu=\rho\{10^{10^{[-3.1562\log_{10}\left\{\frac{v\rho_{oil}}{k_{oil}}(R\omega)^2+T(\omega=0)\right\}+8.9679]}}-0.8\}$$

$$-\frac{h^3}{12\rho\{10^{10^{[-3.1562\log_{10}\left\{\frac{v\rho_{oil}}{k_{oil}}(R\omega)^2+T(\omega=0)\right\}+8.9679]}}-0.8\}}\frac{\frac{k_{teflon}h}{2\pi R\Delta x}-P_{atm}}{\Delta x}+\frac{R\omega h}{2}=0$$

$$\frac{h_1^{\,3}h_2^{\,3}+\frac{b_1}{b}(1-\frac{b_1}{b})\sin^2\beta(h_1^{\,3}-h_2^{\,3})^2}{(1-\frac{b_1}{b})h_1^{\,3}+\frac{b_1}{b}h_2^{\,3}}\left\{\frac{P_{atm}-\frac{k_{teflon}h}{2\pi R\Delta x}}{12\mu\Delta x}\right\}+\frac{R\omega}{2}\left\{\frac{(h_1-h_2)\frac{b_1}{b}(1-\frac{b_1}{b})\sin\beta\cos\beta(h_1^{\,3}-h_2^{\,3})}{(1-\frac{b_1}{b})h_1^{\,3}+\frac{b_1}{b}h_2^{\,3}}\right\}=0$$

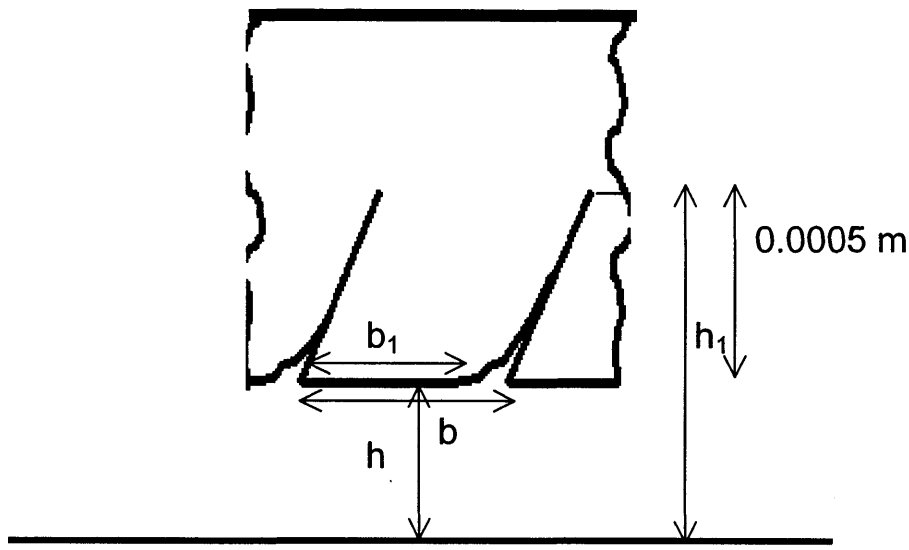

$b = 0.0007m$ $h_1 = h+0.0005$

$b_1 = 0.00056m$ $h_2 = h$

Even though the depth of the groove is about 0.5 mm, not all of the groove is being used. Since there is an angle, some of the groove is compressed the farther away from the lubrication layer it gets. 0.1 mm was an assumed value.

Also, it is assumed that β=1.6 degrees.

Matlab code to calculate the values of h:

```
h1=x+0.0005;
h2=x+.001;
b1=0.00014;
b=0.0007;
%a=(((h1)^3*(h2)^3)+(b1/b)*(1-(b1/b))*((sin(45))^2)*((h1)^3-(h2)^3)^2)/((1-
(b1/b))*((h1)^3)+(b1/b)*((h2)^3));
%b=((h1-h2)*(b1/b)*(1-(b1/b))*sin(45)*cos(45)*((h1)^3-(h2)^3))/((1-
(b1/b))*((h1)^3)+(b1/b)*((h2)^3));

r=.0334;
omega=219.9113;
%31.4159
%62.8318
%94.2477
%125.6636
%157.0795
%188.4954
%219.9113


P=1.01*10^5;
mu=0.053171217;

%0.143492491
%0.122639896
%0.101956167
%0.084977679
%0.071690781
%0.061365464
%0.053171217

x1=.00675;
k=3083332.355;
%function y = f(x)
%f=inline('((x+0.0005-(x+0.001))*(0.2)*(1-0.2)*sin(45)*cos(45)*((x+0.0005)^3-
(x+0.001)^3))/((1-
0.2)*((x+0.0005)^3)+(0.2)*((x+0.001)^3))*0.0334*31.4159*0.5+1.01*10^5*(((x+0.0005)^3*(x
+0.001)^3)+(0.2)*(1-0.2)*((sin(45))^2)*((x+0.0005)^3-(x+0.001)^3)^2)/((1-
0.2)*((x+.0005)^3)+(.2)*((x+.001)^3))/(12*0.143492491*.00675)-
(((x+0.0005)^3*(x+0.001)^3)+(0.2)*(1-0.2)*((sin(45))^2)*((x+0.0005)^3-(x+0.001)^3)^2)/((1-
(0.2))*((x+0.0005)^3)+(0.2)*((x+0.001)^3))*3083332.355*x/(12*0.143492491*2*3.14159*0.03
34*0.00675^2)');
f=inline('((((x+0.0005)^3*(x)^3+(.2)*(1-(.2))*(sin            (1.6))^2*((x+0.0005)^3-(x)^3)^2)/((1-
(.2))*(x+0.0005)^3+(.2)*(x)^3))*((1.01*10^5/(12*0.143492491*(.00675)))-
```

```
(3083332.355*x/(12*0.143492491*2*3.14159*0.0334*(.00675)^2))))+(0.0334*31.4159/2)*(((x
+0.0005-x)*(.2)*(1-(.2))*sin(1.6)*cos(1.6)*((x+0.0005)^3-(x)^3))/((1-
(.2))*(x+0.0005)^3+(.2)*(x)^3))');
z=fzero(f,.0002)
f=inline('((((x+0.0005)^3*(x)^3+(.2)*(1-(.2))*(sin          (1.6))^2*((x+0.0005)^3-(x)^3)^2)/((1-
(.2))*(x+0.0005)^3+(.2)*(x)^3))*((1.01*10^5/(12*0.122639896*(.00675)))-
(3083332.355*x/(12*0.122639896*2*3.14159*0.0334*(.00675)^2))))+(0.0334*62.8318/2)*(((x
+0.0005-x)*(.2)*(1-(.2))*sin(1.6)*cos(1.6)*((x+0.0005)^3-(x)^3))/((1-
(.2))*(x+0.0005)^3+(.2)*(x)^3))');
z=fzero(f,.0002)
f=inline('((((x+0.0005)^3*(x)^3+(.2)*(1-(.2))*(sin          (1.6))^2*((x+0.0005)^3-(x)^3)^2)/((1-
(.2))*(x+0.0005)^3+(.2)*(x)^3))*((1.01*10^5/(12*0.101956167*(.00675)))-
(3083332.355*x/(12*0.101956167*2*3.14159*0.0334*(.00675)^2))))+(0.0334*94.2477/2)*(((x
+0.0005-x)*(.2)*(1-(.2))*sin(1.6)*cos(1.6)*((x+0.0005)^3-(x)^3))/((1-
(.2))*(x+0.0005)^3+(.2)*(x)^3))');
z=fzero(f,.0002)
f=inline('((((x+0.0005)^3*(x)^3+(.2)*(1-(.2))*(sin          (1.6))^2*((x+0.0005)^3-(x)^3)^2)/((1-
(.2))*(x+0.0005)^3+(.2)*(x)^3))*((1.01*10^5/(12*0.084977679*(.00675)))-
(3083332.355*x/(12*0.084977679*2*3.14159*0.0334*(.00675)^2))))+(0.0334*125.6636/2)*(((
x+0.0005-x)*(.2)*(1-(.2))*sin(1.6)*cos(1.6)*((x+0.0005)^3-(x)^3))/((1-
(.2))*(x+0.0005)^3+(.2)*(x)^3))');
z=fzero(f,.0002)
f=inline('((((x+0.0005)^3*(x)^3+(.2)*(1-(.2))*(sin          (1.6))^2*((x+0.0005)^3-(x)^3)^2)/((1-
(.2))*(x+0.0005)^3+(.2)*(x)^3))*((1.01*10^5/(12*0.071690781*(.00675)))-
(3083332.355*x/(12*0.071690781*2*3.14159*0.0334*(.00675)^2))))+(0.0334*157.0795/2)*(((
x+0.0005-x)*(.2)*(1-(.2))*sin(1.6)*cos(1.6)*((x+0.0005)^3-(x)^3))/((1-
(.2))*(x+0.0005)^3+(.2)*(x)^3))');
z=fzero(f,.0002)
f=inline('((((x+0.0005)^3*(x)^3+(.2)*(1-(.2))*(sin          (1.6))^2*((x+0.0005)^3-(x)^3)^2)/((1-
(.2))*(x+0.0005)^3+(.2)*(x)^3))*((1.01*10^5/(12*0.061365464*(.00675)))-
(3083332.355*x/(12*0.061365464*2*3.14159*0.0334*(.00675)^2))))+(0.0334*188.4954/2)*(((
x+0.0005-x)*(.2)*(1-(.2))*sin(1.6)*cos(1.6)*((x+0.0005)^3-(x)^3))/((1-
(.2))*(x+0.0005)^3+(.2)*(x)^3))');
z=fzero(f,.0002)
f=inline('((((x+0.0005)^3*(x)^3+(.2)*(1-(.2))*(sin          (1.6))^2*((x+0.0005)^3-(x)^3)^2)/((1-
(.2))*(x+0.0005)^3+(.2)*(x)^3))*((1.01*10^5/(12*0.053171217*(.00675)))-
(3083332.355*x/(12*0.053171217*2*3.14159*0.0334*(.00675)^2))))+(0.0334*219.9113/2)*(((
x+0.0005-x)*(.2)*(1-(.2))*sin(1.6)*cos(1.6)*((x+0.0005)^3-(x)^3))/((1-
(.2))*(x+0.0005)^3+(.2)*(x)^3))');
z=fzero(f,.0002)
```

Works Cited

[1] Constantinescu, V. N. and Galetuse, S. (1992). "On Extending the Narrow Spiral-Groove Theory to Configurations of Interest in Seals." Journal of Tribology 114.

[2] Constantinescu, V. N. and Castelli, V. (1969). "On the Local Compressibility Effect in Spiral-Groove Bearings." Journal of Lubrication Technology.

[3] Gabelli, A. and Poll, G. (1992). "Formation of Lubricant Film in Rotary Sealing Contacts: Part I-Lubricant Film Modeling." Transactions of the ASME 114.

[4] Gabelli, A. "Micro-elastohydrodynamic lubricant film formation in rotary lip seal contacts." In Proceedings of the 15th Leeds-Lyon Symposium on *Tribology*, Leeds, 1988, pp. 57-68 (Elsevier, Amsterdam).

[5] Hidrovo, C.H., Hart, D. P., 2001. "2D Thickness and Temperature Mapping of Fluids by Means of a Two Dye Laser Induced Fluorescence Ratiometric Scheme", Proceedings of the 3rd Pacific Symposium on Flow Visualization and Image Processing, March 18-21, 2001, Maui, Hawaii.

[6] Hidrovo, C.H., Hart, D. P., 2001, "Emisson Reabsorption Laser Induced Fluorescence (ERLIF) Film Thickness Measurement." Volume 12, Number 4, pp. 467-477.

[7] Hirano, F. and Ishiwata, H. "The Lubricating Condition of a Lip Seal." Proc. Instn. Mech. Engrs, 1965-6, 180(3B), 187-196.

[8] Jagger, E. T. and Walker, P. S. (1966-67). "Further Studies of the Lubrication of Synthetic Rubber Rotary Shaft Seals." Proc. Instn. Mechanical Engrs 181.

[9] Jagger, E. T. "Rotary Shaft Seals-Some Effect of Shaft Surface Finish." In the International Conference on Fluid Sealing.

[10] Jagger, E. T. (1957). "Study of the Lubrication of Synthetic Rubber Rotary Shaft Seals." Proc. of Conf. Lubric. Wear 409.

[11] Kammöller, M. (1986). "Aur Abdichtwirkung von Radial-Wellendichtringen." Thesis, University of Stuttgart (in German).

[12] Möller, H. K. (1987). "Concepts of Sealing Mechanism of Rubber Lip Type Rotary Shaft Seals." Proc. 11th International Conference on Fluid Sealing, Cannes.

[13] Müller, Heinz K., (1933). Fluid Sealing Technology. New York : M. Dekker, 1998.

[14] Saeki, S., Hart, D. P., 2001, "Investigation on YAG(532) Laser Dyes for Oil Film Thickness and Temperature Measurement." Proceedings of the 3rd Pacific Symposium on Flow Visualization and Image Processing, March 18-21, 2001, Maui, Hawaii.

[15] Salant, R. F. "Numerical Analysis of the Flow Fiel Within Lip Seals Containing Microundulations." Journal of Tribology, 1992, 114.

[16] Shaw, Milton C. and Macks, E. F. Analysis and Lubrication of Bearings, New York: McGraw-Hill Book Company, Inc., 1949.

[17] Stakenborg, M. J. L., 1988, "On the Sealing Mechanism of Radial Lip Seals." TribologyInternational, volume 21, pp. 335-340.

5186
59